



**HAL**  
open science

# Density profile reconstruction methods for extraordinary mode reflectometry

Rennan Bianchetti Morales

► **To cite this version:**

Rennan Bianchetti Morales. Density profile reconstruction methods for extraordinary mode reflectometry. Plasma Physics [physics.plasm-ph]. Université de Lorraine, 2018. English. NNT : 2018LORR0031 . tel-01836220

**HAL Id: tel-01836220**

**<https://theses.hal.science/tel-01836220>**

Submitted on 12 Jul 2018

**HAL** is a multi-disciplinary open access archive for the deposit and dissemination of scientific research documents, whether they are published or not. The documents may come from teaching and research institutions in France or abroad, or from public or private research centers.

L'archive ouverte pluridisciplinaire **HAL**, est destinée au dépôt et à la diffusion de documents scientifiques de niveau recherche, publiés ou non, émanant des établissements d'enseignement et de recherche français ou étrangers, des laboratoires publics ou privés.



## AVERTISSEMENT

Ce document est le fruit d'un long travail approuvé par le jury de soutenance et mis à disposition de l'ensemble de la communauté universitaire élargie.

Il est soumis à la propriété intellectuelle de l'auteur. Ceci implique une obligation de citation et de référencement lors de l'utilisation de ce document.

D'autre part, toute contrefaçon, plagiat, reproduction illicite encourt une poursuite pénale.

Contact : [ddoc-theses-contact@univ-lorraine.fr](mailto:ddoc-theses-contact@univ-lorraine.fr)

## LIENS

Code de la Propriété Intellectuelle. articles L 122. 4

Code de la Propriété Intellectuelle. articles L 335.2- L 335.10

[http://www.cfcopies.com/V2/leg/leg\\_droi.php](http://www.cfcopies.com/V2/leg/leg_droi.php)

<http://www.culture.gouv.fr/culture/infos-pratiques/droits/protection.htm>

# Density profile reconstruction methods for extraordinary mode reflectometry



UNIVERSITÉ  
DE LORRAINE

COLLEGIUM  
TECHNOLOGIE



**Rennan Bianchetti Morales**

Members of the jury:

Prof. Stéphane Heuraux	Thesis Director
Dr. Roland Sabot	Thesis Co-Director
Dr. Sébastien Hacquin	Examiner
Dr. Carine Giroud	Examiner
Prof. Zwinglio de Oliveira Guimarães Filho	Referee
Dr. Carlos Silva - Senior Scientist	Referee

Institut Jean Lamour  
Université de Lorraine

This dissertation is submitted for the degree of  
*Doctor of Philosophy*

École doctorale EMMA

25<sup>th</sup> May 2018



# Table of contents

<b>Acknowledgement</b>	<b>1</b>
<b>Abstract</b>	<b>3</b>
<b>Résumé</b>	<b>5</b>
<b>Résumé étendu</b>	<b>7</b>
<b>1 Introduction</b>	<b>15</b>
1.1 Nuclear fusion: a promising source of energy . . . . .	15
1.1.1 Confinement techniques . . . . .	17
1.1.2 Optimization of the energy output . . . . .	22
1.2 Main physics used in this thesis . . . . .	24
1.2.1 Waves in plasmas . . . . .	25
1.2.2 Wave scattering . . . . .	29
1.3 Non-perturbative density diagnostics . . . . .	32
1.3.1 Basic principles of reflectometry . . . . .	33
1.3.2 I/Q demodulation . . . . .	36
1.4 Objectives and outline of this thesis . . . . .	39
<b>2 Numerical tools to simulate the reflectometer signals</b>	<b>41</b>
2.1 Simulations using the WKB approximation . . . . .	41
2.2 1D full-wave wave equation solver . . . . .	42
2.2.1 Code's numerical dispersion . . . . .	45
2.3 Phase and time-of-flight extraction . . . . .	46
<b>3 X-mode inversion methods</b>	<b>49</b>
3.1 Introduction . . . . .	49
3.2 Overview of Bottollier-Curtet's method . . . . .	50

3.3	New approaches on the reconstruction method . . . . .	53
3.3.1	Parabolic integration shapes . . . . .	53
3.3.2	Square root integration shapes . . . . .	55
3.3.3	$x^\alpha$ integration shapes . . . . .	55
3.4	Comparison of accuracy from all methods . . . . .	56
3.5	Stability of the inversion method . . . . .	60
3.6	Noise analysis . . . . .	61
3.7	Approaching the optimal W(R) profile from iterative reconstructions . . . . .	64
3.8	Obtaining the ideal refractive index shape from the plasma properties . . . . .	67
3.9	Reconstructions with less probing frequencies . . . . .	73
3.10	Conclusions . . . . .	74
<b>4</b>	<b>Blind areas in frequency swept reflectometry</b>	<b>77</b>
4.1	Proof of concept in WKB framework . . . . .	79
4.2	Introduction to time dependent full-wave effects in the simulated signals . . . . .	81
4.3	The amplitude drop related to the tunneling and frequency mixing effects . . . . .	84
4.4	Resonances . . . . .	88
4.5	Reflections and Bragg backscattering from square perturbations . . . . .	90
4.6	Influence of the perturbation shape on the time-of-flight signal . . . . .	92
4.6.1	Effect from the perturbation skewness. . . . .	93
4.6.2	Effect from the perturbation kurtosis. . . . .	94
4.7	A method to estimate the perturbation size with fixed conditions . . . . .	98
4.8	Multiple perturbations . . . . .	100
4.9	A generalization of the reconstruction schemes . . . . .	103
4.9.1	Review of the impact of full-wave effects on the reconstruction method . . . . .	103
4.9.2	Database of time-of-flight signals from sine shaped valleys . . . . .	106
4.9.3	Example of reconstruction using the database on a synthetic case . . . . .	108
4.9.4	Analysis of reconstruction accuracy . . . . .	108
4.10	Conclusions and future prospects . . . . .	116
<b>5</b>	<b>Issues and new improvements on the determination of the first cut-off position</b>	<b>119</b>
5.1	Benchmarks of the initialization error . . . . .	120
5.1.1	Shifts from errors in the starting density value . . . . .	120
5.1.2	Shifts from neglecting shallow plasma . . . . .	123

---

5.1.3	Shifts from errors in the magnetic field . . . . .	125
5.1.4	Conclusions from benchmarking the initialization errors . . . . .	125
5.2	Full-wave signals in the vicinity of the first cut-off . . . . .	126
5.3	Perturbations in the vicinity of the first cut-off . . . . .	129
5.4	Partial conclusions . . . . .	135
5.4.1	Future prospects . . . . .	136
<b>6</b>	<b>Conclusions and prospects</b>	<b>139</b>
6.1	General conclusions . . . . .	139
6.2	Future prospects . . . . .	142
	<b>References</b>	<b>143</b>
	<b>Appendix A Experimental application of optimized <math>W(f)</math></b>	<b>149</b>
	<b>Appendix B Experimental demonstration of blind area reconstruction</b>	<b>153</b>
	<b>Appendix C Experimental errors in the initialization technique</b>	<b>159</b>



# Acknowledgements

First and foremost, I would like to thank my supervisors Stéphane Heuraux and Roland Sabot for taking me as a their student and providing me many interesting ideas to research about. Sébastien Hacquin also attended nearly all our meetings and followed my work closely, always providing all possible help. I am very grateful to have had these researchers of three different specialities that complement each other quite well. They provided me with the latest technical knowledge and always very good orientation. I also felt very pleased to deal with them in a personal level. Even though they are very senior and highly qualified researchers, they were always extremely easily approachable, uplifting and friendly. This made for a very pleasant and motivating working environment.

During my PhD I spent most of the time in IJL (Institut Jean Lamour), although it was initially planned to evenly distribute the time with the CEA research center, but unfortunately was not possible due to the administrative complications encountered. Nevertheless, I thank my supervisors for the extensive and incessant effort on this bureaucratic action. I am thankful to Stéphane Heuraux to have guided me during this unplanned extended time in IJL.

I would like to thank the members of the jury for taking interest on my research topic and participating on my PhD defense.

I want to thank Frédéric Clairet and Christine Bottereau for the interest in my research and the discussions we had while in CEA. In addition, I thank Frédéric Clairet for the help on the pursuit of data from the JET and Tore Supra databases.

I also want to thank my colleagues Hugo Arnichand and Gregoire Hornung for the initial exchanges when I have just started my PhD, and Georgiy Zadvitskiy and Yan Sun for the frequent discussions on various topics related to our PhD projects.

Last but not least, I would like to thank my wife and my family for all the support I always had in my academic career.

The work I present here was only possible due to the funding provided by the Brazilian National Council for Scientific and Technological Development (CNPq) under the program Science without Borders, for which I am also very grateful.



# Abstract

The main objective of this PhD is to improve the data analysis techniques from X-mode frequency swept reflectometry for determination of the electronic density profile of fusion plasmas. The applications are numerous, including the improvement of turbulence studies, validation of numerical simulations, and real-time monitoring of the plasma shape and position. The results obtained will benefit the research in the current and next generation of fusion experiments, like ITER and DEMO.

The first topic investigated was the optimization of the density profile reconstruction algorithm. Not only a more accurate density profile is achieved, specially in the edge region, but the results obtained also allow to reduce the number of frequency steps used to perform the profile reconstruction without causing a deterioration of the profile accuracy. Reducing the number of frequency steps speeds up the reconstruction algorithm, enabling access to faster profile changes in real-time applications.

The next step was to investigate perturbations in the density profile that causes the cut-off profile to have a blind zone, where the probing waves are not reflected. Firstly, it was demonstrated how these perturbations degrade the reconstructed density profile when the standard reconstruction scheme is applied. Next, 1D time-dependant full-wave simulations were employed to investigate the various full-wave effects that affect the perturbation signature in the reflectometer signal. After observing all full-wave effects in place, a band was set where the perturbation signatures can be analysed in the WKB validity domain. With this in mind, the WKB approximation was used to generate a database of signals originated from isolated perturbations. From the database, the observed signal can be inverted into determining the perturbation size. The next step was to demonstrate and discuss all the factors that influence the precision of the reconstruction of a blind area. The final precision of the perturbation reconstruction is not strongly bound to the accuracy of the database, but rather, to how well the initial assumptions hold and the noise level in the experimental signal.

The last topic investigated was the initialization of the density profile reconstruction. The first step was to enumerate all possible error sources in the initialization technique

and compute a benchmark of the error transferred to the reconstructed profiles. The greatest error source emanate from a false assumption, that the cut-off frequency  $f_R$  equals the cyclotron frequency  $f_{ce}$  for the first probing frequency. Various simulations were performed with a minimum critical starting density and added perturbations in the vicinity of the initialization position. The observations on these simulations laid a good basis onto which to perform further research on two distinct branches. The first, on the reconstruction of perturbations in the plasma edge, fully detached from the main density profile. The second, on the determination of the initialization point of the main profile reconstruction in the presence of these perturbations. For the first topic, a database similar to the one developed to reconstruct the blind areas can be computed, this time including the signatures of these fully detached perturbations. On the second topic, the first discrepancy already observed that needs accounting for is the divergence between the full-wave and the WKB signals around the initialization point. Since the profile reconstruction algorithm uses the estimation of the WKB phase, these discrepancies must be corrected to improve the initialization accuracy. This is true even without any perturbation. In order to get results more consistent with the real experimental signals, so that the correct adaptations can be developed, these simulation will be extended in the future to 3D time-dependant full-wave simulations.

# Résumé

L'objectif principal de cette thèse est d'améliorer les techniques d'analyse de données obtenues avec un réflectomètre pour la reconstruction du profil de densité des plasmas de fusion. Les applications sont nombreuses, notamment l'amélioration des études de turbulence, la validation des simulations numériques et la surveillance en temps réel de la forme et de la position du plasma dans les réacteurs de fusion nucléaire. Les résultats obtenus bénéficieront à la recherche actuelle et à la prochaine génération d'expériences de fusion, comme ITER et DEMO.

Le première partie porte sur l'optimisation de l'algorithme de reconstruction du profil de densité. En plus d'avoir obtenu un profil de densité plus précis, spécialement dans la bordure du plasma, la quantité de données à traiter sans entraîner une détérioration de la précision du profil mesuré a été réduite. Cette réduction de la quantité de données à traiter permet d'accéder en temps réel à des changements de profils de densité, ce qui est pertinent pour les futurs réacteurs en fonctionnement continu.

Le développement suivant traite des perturbations du profil de densité conduisant à des profils creux considérés comme non-inversibles. Tout d'abord, il a été démontré comment ces perturbations dégradent le profil de densité reconstruit lorsque le schéma de reconstruction standard est appliqué. Ensuite, des simulations "full-wave" dépendant du temps en 1D ont été utilisées pour étudier les divers effets qui affectent la signature de perturbation dans le signal de réflectomètre. Ensuite, une base de données de signaux provenant de perturbations isolées a été élaborée. Cette base a été utilisée pour inverser de la signature de perturbation à la taille de perturbation. Ensuite il a été démontré et discuté quels sont les facteurs qui influencent la précision de la reconstruction de ces profils creux. La précision finale de la reconstruction de perturbation n'est pas fortement liée à la précision de la base de données, mais plutôt au bon respect des hypothèses initiales et au niveau de bruit dans le signal expérimental.

La dernière étude s'intéresse à l'initialisation de la reconstruction du profil de densité. La première partie est une énumération de toutes les sources d'erreur possibles dans la technique d'initialisation et à déterminer comment ces erreurs d'initialisation sont

transférées au profil reconstruit. La plus grande source d'erreur provient de l'hypothèse fautive où la densité est supposée négligeable pour la première fréquence de coupure. Ensuite, diverses simulations ont été effectuées avec des perturbations supplémentaires au voisinage de la position d'initialisation. L'analyse de ces simulations a fourni une bonne base de réflexion sur laquelle s'ancre deux axes de recherche plus approfondis. Le premier porte sur la reconstruction des perturbations dans le bord du plasma, complètement détaché du profil de densité principal. Le second se focalise sur la détermination du point d'initialisation de la reconstruction du profil principal en présence de ces perturbations. Pour le premier thème, une base de données similaire à celle développée pour reconstruire les zones aveugles peut être construite où sont incluses les signatures de ces perturbations complètement détachées. Pour le deuxième point, la première divergence déjà constatée sur la prise en compte des besoins est la divergence entre les signaux "full-wave" et de WKB autour du point d'initialisation. Puisque l'algorithme de reconstruction de profil utilise l'estimation de la phase WKB, ces écarts doivent être corrigés pour améliorer la précision de l'initialisation. Cet effet s'avère vrai même sans aucune perturbation de densité. Afin d'obtenir des résultats plus cohérents avec les vrais signaux expérimentaux, de sorte que les adaptations correctes puissent être développées, ces simulations seront étendues dans le futur à des simulations 3D full-wave dépendant du temps.

# Résumé étendu

L'objectif principal de cette thèse est d'améliorer les techniques d'analyse de données fournies par la réflectométrie par balayage de fréquence en mode X pour la détermination de tout le profil de densité électronique des plasmas de fusion. Les applications sont nombreuses, notamment l'amélioration des études de turbulence, la validation des simulations numériques et la surveillance en temps réel de la forme et de la position du plasma. Les résultats obtenus à l'aide des nouvelles méthodes développées dans cette thèse profiteront à la recherche actuelle sur les plasma de fusion et la prochaine génération d'expériences de fusion, comme ITER et DEMO.

Le premier sujet étudié était l'optimisation de l'algorithme de reconstruction du profil de densité, traité dans le Chap. 3.

La première méthode de reconstruction publiée par Bottollier-Curtet et Ichtschenko en 1987 est la méthode standard de reconstruction des profils de densité pour la réflectométrie dit "mode X" depuis lors, avec seulement des révisions mineures. Bien qu'il soit théoriquement possible d'augmenter la précision du profil reconstruit simplement en augmentant le nombre de fréquences prises en compte pour l'algorithme de reconstruction, la résolution pratique des fréquences est limitée non seulement par la résolution de l'équipement, le temps de calcul mais surtout par la présence de nombreuses sources de bruit. L'addition artificielle de plus de points de fréquence par interpolation du signal n'est pas non plus viable parce qu'elle peut ajouter des erreurs artificielles à partir de n'importe quelle fausse représentation du signal réel. Cet effet est observé plus loin dans l'étude de la reconstruction des zones aveugles. De plus, les applications de surveillance en temps réel bénéficient d'algorithmes de reconstruction plus rapides, qui ont une relation directe avec le nombre de fréquences utilisées durant la reconstruction. Par conséquent, la seule alternative pour améliorer la précision de la reconstruction est d'améliorer l'évaluation de la position de chaque pas en fréquence. Seules des données synthétiques ont été utilisées pour cette recherche. La justification de ce choix vient du fait que c'est le seul moyen de connaître le profil de densité réelle permettant ainsi de vérifier la précision de la nouvelle méthode de reconstruction développée dans cette thèse.

La procédure suivie consistait à s'appuyer sur des fonctions chaque fois plus complexes que de simples fonctions linéaires pour décrire la forme de l'indice de réfraction à chaque étape d'intégration, comme cela a été fait dans Sec. 3.3. La stabilité et la précision obtenues lors de l'utilisation des fonctions de puissance fractionnaire parabolique et fixe ou adaptative sont comparées à la méthode précédente dans Sec. 3.4 et après avoir été testées contre les événements parasites et le bruit de phase dans Secs. 3.5 et 3.6. Les conclusions de ces études ont permis d'optimiser les meilleures formes d'intégration par rapport aux paramètres du plasma, dans Sec. 3.8. Il a été démontré que l'utilisation des fonctions de puissance fractionnaire optimisée radialement a amélioré la précision et la stabilité du profil reconstruit parce que ces fonctions approximent bien la véritable forme de l'indice de réfraction. Bien que l'utilisation d'un profil de racine carrée ait donné de bons résultats dans le plasma de coeur, ce n'est pas la forme la mieux adaptée dans le plasma de bord. Dans cette région, la puissance des fonctions de puissance fractionnaire peut être très proche de zéro pour les premières fréquences réfléchies. L'adaptation de la puissance de ces fonctions en fonction du profil plasma a montré une amélioration de la précision du profil plasma de bord pouvant aller jusqu'à deux ordres de grandeur. L'amélioration exacte dépend aussi de la précision de l'initialisation et du profil à reconstruire.

La comparaison entre toutes les méthodes étudiées a également montré que la reconstruction est plus stable lorsqu'on n'utilise aucune information sur les positions précédemment calculées pour déterminer la position suivante, ou même, forçant une variation plus lente sur l'une quelconque des conditions de reconstruction. Il a été démontré que toutes ces procédures retardent la capacité d'amortissement des erreurs de la méthode de reconstruction lors de l'introduction d'événements parasites et de bruit de phase. De plus, l'analyse sur la stabilité de reconstruction a déduit un meilleur amortissement des erreurs pour des valeurs plus élevées de  $WN_{n-1}$  (le facteur de poids d'intégration multiplié par l'indice de réfraction à la dernière position connue), ce qui est typique des conditions de bord.

Lors de la reconstruction d'une forme de profil de densité bien connue contenant une transition claire du piédestal, les formes d'intégration optimisées pourraient être facilement proposées. Les goulets d'étranglement de cette mise en oeuvre sont : une transition évidente vers le piédestal ; et la précision du facteur d'intégration supposé dans la première étape de reconstruction. La méthode élaborée dans la Sec. 3.8 supprime ces questions. Il peut être utilisé pour déterminer le profil complet des facteurs d'intégration pour n'importe quelle forme de profil. L'optimisation des facteurs d'intégration permet également d'utiliser un nombre réduit de fréquences de sondage pour reconstruire le profil

sans perte de précision, comme le démontrent deux exemples traités dans cette thèse. Cette fonction permet de suivre en temps réel l'évolution plus rapide du profil de densité.

La procédure développée pour optimiser les formes d'intégration est applicable à n'importe quelle forme de profil de densité. Chap. 3 se termine par une démonstration en Sec. 3.9 de toutes les améliorations décrites lors de l'application du schéma de reconstruction dans sa version optimisée et ceci dans un cas très exigeant : un profil de coupure linéaire à faible gradient, avec la contrainte supplémentaire d'utiliser moins de fréquences de palpation. Non seulement un profil de densité plus précis a été obtenu en appliquant les formes d'intégration optimisées, en particulier dans la région des bords, mais il a également démontré la réduction du nombre d'étapes de fréquence utilisées pour effectuer la reconstruction du profil sans causer une détérioration de la précision du profil. La réduction du nombre de pas de fréquence accélère l'algorithme de reconstruction, ce qui permet d'accéder plus rapidement aux changements de profil dans les applications en temps réel.

Le deuxième sujet étudié était la description des perturbations de densité qui font que le profil de coupure a une zone aveugle, où les ondes de sondage ne sont pas réfléchies. La reconstruction des zones aveugles en réflectométrie à balayage de fréquence n'a jamais été abordée auparavant.

Lors d'une décharge lors d'expériences de fusion, de nombreux phénomènes peuvent introduire des perturbations dans le profil de densité. Les fluctuations de turbulence à petite échelle génèrent un changement global dans le signal de phase acquis et le processus d'inversion des propriétés de fluctuation est étudié par une fonction de transfert. Pour les perturbations isolées, la signature sur le signal du réflectomètre est liée à la taille de la perturbation. Le spectre du signal de phase peut être utilisé pour décrire la forme de perturbation dans certains cas à petite échelle (dans l'ordre de la longueur d'onde de sondage). Dans cette situation, le champ électrique de sondage est encore proche du profil non perturbé. Ici, d'autre part, les perturbations plus importantes, hors du domaine de validité de l'approximation Born, sont étudiées, en se concentrant sur les perturbations introduisant une vallée dans le profil de densité qui est suffisamment grande pour que les micro-ondes de sondage n'aient pas de réflexion à l'intérieur de la vallée et que le champ électrique de sondage ne soit plus proche du cas non perturbé. Cette situation peut se produire lors d'injections massives de gaz et de pellets, de l'activité MHD et dans les profils creux qui émergent lors de l'initiation des systèmes de chauffage. Si la méthode de reconstruction n'incorpore pas des outils d'identification et de reconstruction pour ces régions masquées, de grandes divergences peuvent apparaître dans le profil reconstruit comme démontré dans le Chap. 4. Il est clair que la reconstruction standard ne décrit

pas bien la perturbation. De plus, si les oscillations introduites sont lisses, la perturbation peut être entièrement négligée, ou pire encore, un glissement peut être introduit dans le profil reconstruit après la perturbation.

Même si les micro-ondes de sondage n'ont pas de réflexion à l'intérieur de la zone aveugle, il y a des informations à exploiter à partir des fréquences plus élevées qui se propagent à travers la perturbation. Les paramètres nécessaires pour décrire une perturbation sont : la largeur de la perturbation, la profondeur de la perturbation et la forme de la perturbation. Pour simplifier, les premières perturbations étudiées ont une forme et une largeur bien connues et sont insérées dans une région avec un profil de coupure linéaire. De cette façon, le profil de densité peut être reconstitué à l'aide d'un signal non perturbé, qui peut provenir d'un balayage précédent ou d'une interpolation du signal de temps de vol, la signature de perturbation étant supprimée. Ensuite, la signature de la perturbation est évaluée pour déterminer ses propriétés. La première approche pour déterminer la profondeur de la perturbation consistait à mettre à l'échelle certaines signatures de perturbation dans le signal de temps de vol en fonction de la profondeur de la perturbation (pour une largeur et une forme présumées). Comme preuve de concept, cette procédure a d'abord été démontrée dans le cadre de l'approximation WKB dans Sec. 4.1. Par la suite, le signal du réflectomètre a été simulé à l'aide d'un solveur d'équation d'ondes 1D pour tenir compte des effets de pleine onde tels que l'effet tunnel, le piégeage des ondes, l'interférence et la diffusion. Bien que les principales caractéristiques physiques des régions masquées soient bien décrites par les simulations 1D présentes dans cette contribution, des simulations 3D sont nécessaires pour vérifier tous les aspects géométriques supplémentaires. Après tout, la surface et la forme du faisceau de sondage, ainsi que la forme des perturbations, rendent un système trop complexe pour être complètement décrit à une seule dimension. Les aspects géométriques influencent aussi fortement l'évolution de l'amplitude. Ceci est un sujet à approfondir dans le cas des zones aveugles et spécialement pour la technique d'initialisation, c'est-à-dire le dernier sujet étudié dans cette thèse.

Lors de la simulation des signaux de temps de vol avec le code 1D full-wave, les sauts au-dessus des zones aveugles ont été lissés en raison de la conservation du flux électromagnétique et de l'effet tunnel. Une baisse de l'amplitude du signal est également observée sur la bande de fréquence d'effet tunnel. Sur les fréquences correspondant à la chute d'amplitude, les ondes diffusées deviennent évidentes et les modèles d'interférence sont visibles. Ces effets peuvent perturber de manière significative une technique de reconstruction qui échelonne le signal de perturbation en fonction de la profondeur de la perturbation, surtout si l'on tient compte de la bande de fréquence de sondage à

proximité de la bande d'évanescence. Une autre complication de cette approche est la description de perturbations multiples, comme par exemple une bosse suivie d'une vallée, c'est-à-dire un profil de densité typique d'un vortex. La signature de perturbation sur le changement de temps de vol est significative pour un cas de perturbation multiple. Il est pratiquement impossible de suivre toutes les combinaisons de perturbations possibles et de faire correspondre les formes respectives. Il existe cependant une autre approche qui peut être mise en oeuvre sans ces problèmes majeurs. Il s'agit d'une approche de base de données contenant les signaux de perturbation du temps de vol excessif. Avec cette approche, la bande de fréquence de sondage de la signature de perturbation s'étend bien au-delà des fréquences pour lesquelles il y a un effet tunnel, en particulier pour les perturbations plus importantes, et peut être reconstruite même avec des perturbations multiples complexes. Les perturbations multiples complexes peuvent être subdivisées en perturbations uniques et traitées séparément.

Comme première approximation, on a supposé que la base de données sur les perturbations avait des vallées sinusoidales. Si une autre forme est intéressante, la base de données peut être recalculée pour cette forme spécifique. En fin de compte, quelques formes différentes peuvent être disponibles si la situation indique la préférence d'une forme spécifique par rapport aux autres. Les études futures, y compris les simulations 3D ou une connaissance préalable de la forme de perturbation étudiée, peuvent dicter la forme à utiliser dans la base de données pour une estimation plus précise de la profondeur de la perturbation.

L'erreur induite dans la reconstruction de la perturbation causée par le bruit dans le temps de vol et les signaux  $f_{ce}$  a été décrite dans la Sec. 4.9.4 pour toute la gamme de paramètres couverts. Aucune région de paramètres n'a été trouvée avec une erreur extraordinairement élevée. Les sources d'erreur supplémentaires possibles sont les hypothèses faites sur le gradient du profil non perturbé, la largeur de la perturbation et la forme de la perturbation. Les hypothèses sur le gradient de profil non perturbé et la largeur de la perturbation varieront en fonction de chaque application. Dans les cas où des données sont disponibles pour une évolution claire et bien conduite du profil, ces hypothèses sont simples et précises. S'il n'y a qu'un seul balayage et que le profil inclut des perturbations de grande amplitude et à petite valeur de  $k$ , par définition, ces hypothèses ne seront pas exactes. Comme perspective d'avenir, l'hypothèse sur la forme estimée peut être corroborée par des prédictions théoriques ou des simulations numériques des perturbations étudiées.

Les effets au-delà de l'approximation WKB illustrés dans le Chap. 4 sont principalement limités à la bande liée à l'effet de tunnel et ont été évités dans la technique de

reconstruction des régions aveugles. Les effets d'ondes entières observés ont rarement une amplitude suffisante pour être distinguables dans un signal expérimental bruyant. L'extraction fiable d'informations à partir de ces effets ne sera possible que lorsque d'autres développements dans le domaine du matériel seront réalisés. De plus, l'amplitude de ces effets peut encore être fortement liée aux aspects géométriques 3D qui doivent être étudiés dans les simulations 3D pleine onde.

Même si d'autres recherches sont prévues sur les aspects géométriques 3D et les formes de perturbation décrites ci-dessus, la base de données de forme sinusoïdale 1D développée ici sera d'abord appliquée à des cas expérimentaux dans un proche avenir afin de démontrer la viabilité de cette approche pour déterminer le profil de densité à l'intérieur des zones masquées.

Le dernier sujet étudié était l'initialisation de la reconstruction du profil de densité. La première étape consistait à énumérer toutes les sources d'erreur possibles dans la technique d'initialisation et à calculer un repère de l'erreur transférée aux profils reconstruits. La tâche de benchmarking a produit une référence pour l'erreur attendue introduite dans le profil de densité reconstruit en fonction de la précision des différentes sources d'erreur possibles. L'erreur peut être supposée à peu près constante radialement, ce qui signifie qu'elle agit comme un décalage du profil de densité. Ces repères ont non seulement servi de référence pour connaître les barres d'erreur de profil, mais aussi pour démontrer les causes possibles d'erreur et leur importance. En raison des valeurs d'erreur élevées démontrées à partir de paramètres raisonnables, il est clair que la qualité de l'initialisation a un impact important sur la précision du profil reconstruit.

La plus grande source d'erreur émane d'une fausse supposition qui dit que la fréquence de coupure  $f_R$  est égale à la fréquence du cyclotron  $f_{ce}$  pour la première fréquence de palpage. Diverses simulations ont été effectuées avec une densité de départ critique minimale à laquelle il est ajoutée des perturbations à proximité de la position d'initialisation. Les observations de ces simulations ont établi les bases d'une recherche plus approfondie sur deux branches distinctes. Le premier porte sur la reconstruction des perturbations dans le bord du plasma complètement détachées du profil de densité principal. La seconde concerne la détermination du point d'initialisation de la reconstruction du profil principal en présence de ces perturbations. Pour le premier sujet, une base de données similaire à celle développée pour reconstruire les zones aveugles peut être calculée, cette fois en incluant les signatures de ces perturbations complètement détachées. En ce qui concerne le deuxième sujet, la première anomalie déjà observée qui tient compte des besoins est la divergence entre les signaux de l'onde complète et les signaux WKB autour du point d'initialisation. Puisque l'algorithme de reconstruction de profil utilise l'estimation de la

phase WKB, ces écarts doivent être corrigés pour améliorer la précision de l'initialisation. Ceci est vrai même sans aucune perturbation. Afin d'obtenir des résultats plus cohérents avec les signaux expérimentaux réels, de sorte que les adaptations correctes puissent être développées, ces simulations seront étendues à l'avenir à des simulations 3D à ondes entières dépendantes du temps.

L'introduction des perturbations de bord a conduit à trois scénarios distincts : la reconstruction des perturbations complètement détachées ; la reconstruction des perturbations entièrement rattachées et les perturbations qui interfèrent avec l'initialisation standard.

Les perturbations entièrement détachées peuvent être traitées sans aucun lien avec le profil de densité principal. Une approche de base de données peut également être développée dans ce cas, mais avec des formes de signaux et des contraintes différentes, en particulier pour la densité minimale détectable liée à la largeur de la perturbation. Des recherches supplémentaires sont encore nécessaires pour décrire pleinement la signature de ces perturbations dans le signal de temps de vol et reconstruire leur profil.

Les cas entièrement attachés ne perturbent pas l'initialisation et peuvent être identifiés et reconstruits avec la même méthodologie développée dans le Chap. 4.

La seule restriction supplémentaire à la procédure d'initialisation est la perturbation partiellement attachée. Dans ces cas, la bande de fréquence d'initialisation non perturbée est modifiée par la perturbation, typiquement dans la bande où la fréquence de sondage passe par-dessus la perturbation dans le profil principal. Le problème dans ces cas est le manque de fréquences de sondage interpolables qui aide à estimer le profil non perturbé. La meilleure approche dans ce cas est d'observer les balayages voisins pour estimer le temps de vol non perturbé et la fréquence de départ.

La procédure d'initialisation est toujours soumise au niveau de bruit du signal. Le bruit du signal du réflectomètre provient principalement de la micro-turbulence, de la diffusion du à des filaments, de l'émission de cyclotron électronique par le plasma, et même de réflexions autour de l'antenne dans certaines situations. Bien qu'il n'entre pas dans le cadre de ce travail d'accéder pleinement à chacun de ces composants, la procédure d'initialisation finale doit être comparée à différents niveaux de bruit de fond. Le "benchmarking" permet d'inférer la précision d'initialisation attendue et d'insérer des barres d'erreur adéquates.

Comme perspective d'avenir, les différentes formes de perturbation peuvent être étudiées à l'aide d'un code 3D pleine onde dépendant du temps. Les aspects géométriques des perturbations de bord possibles combinés à la forme du front d'onde de sondage constituent un système très complexe qui n'est pas entièrement décrit par une analyse

1D. Ces aspects géométriques supplémentaires sont censés réduire la contribution de la signature de la perturbation dans la plupart des cas, mais dans des cas spécifiques, ils peuvent même focaliser le faisceau de sondage et augmenter l'amplitude détectée et ainsi changer la contribution de la perturbation.

# Chapter 1

## Introduction

### 1.1 Nuclear fusion: a promising source of energy

The world population has been steadily increasing without any strong regulation. The combination of the population growth with economic development has been driving up the world's energy consumption, as can be seen in Fig. 1.1. Based on Fig. 1.1, the EIA (U.S. Energy Information Administration) projects that the world energy consumption will grow by 28% between 2015 and 2040.

Fig. 1.1 also shows the strong dependency on fossil fuels for most of the energy production. The usage of fossil fuels for energy production is not a viable long term solution. First, their exploitation cause a bad environmental impact with the emission of greenhouse gases, as one example, being repeatedly reported as the main cause for the observed global warming, as e.g. in Refs. [2, 3]. Second, the fossil fuels reserves are quite limited. The reserves of the main fossil fuels, i.e. oil, gas and coal, were estimated in 2013 to be only 54, 55 and 115 years long, respectively, at the current extraction rate.

Not only the usage of fossil fuels are harming the environment, this scenario is leading to a severe energy crisis. A transition is necessary into energy sources that are renewable and friendly to the environment, as it is further elaborated in Ref. [4]. Although there is a significant expected increase of the contribution from weather dependent renewable sources (such as wind, solar and tides), it is not yet sufficient to meet the global demand. Additionally, they are implemented decentralized and rely on variable weather dependent sources to operate. Thus, not satisfying a centralized and continuous demand of large cities and industrial parks.

The generation of electricity in fusion reactors promises to play an important role towards meeting the long term energy demand without the issues of short term lack of reserves or environmental impact. Unlike the nuclear fission of heavy elements, the

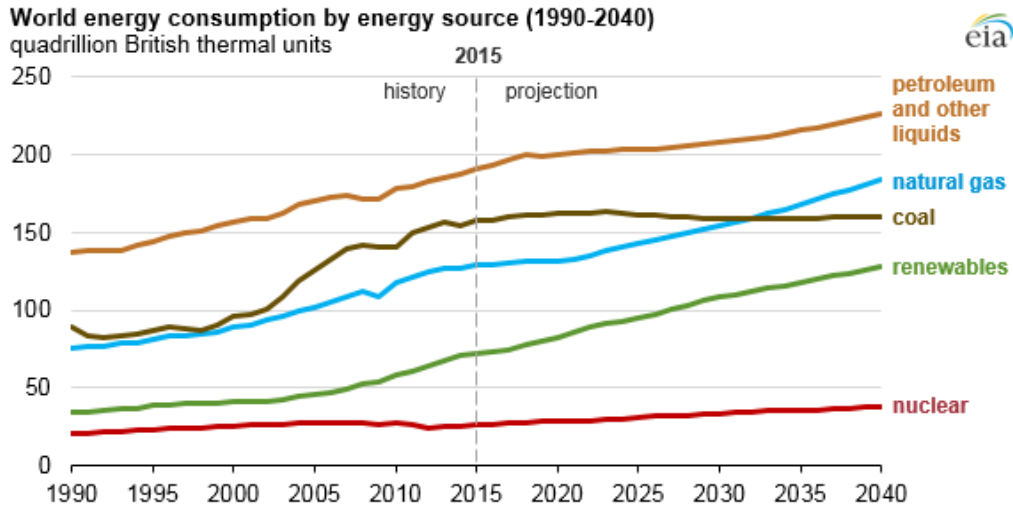


Fig. 1.1 Energy consumption history and projection from all energy sources. From Ref. [1].

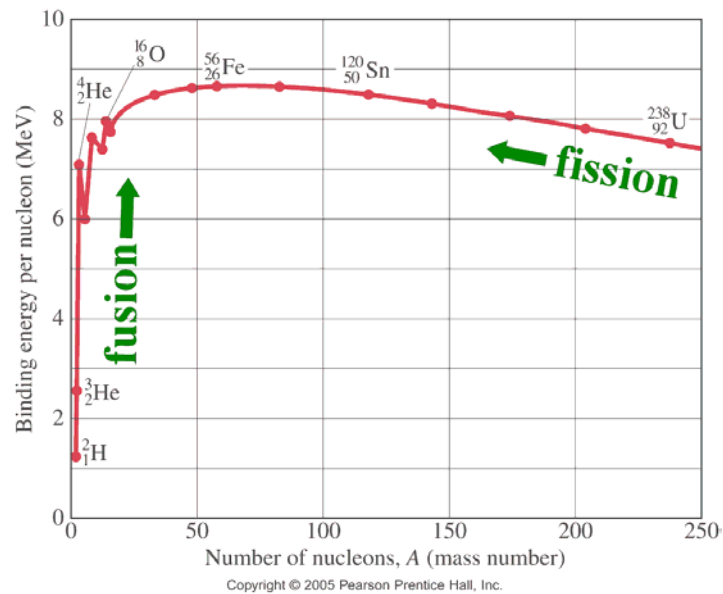


Fig. 1.2 The nuclear binding energy per nucleon as a function of the number of nucleons, which is also the mass number.

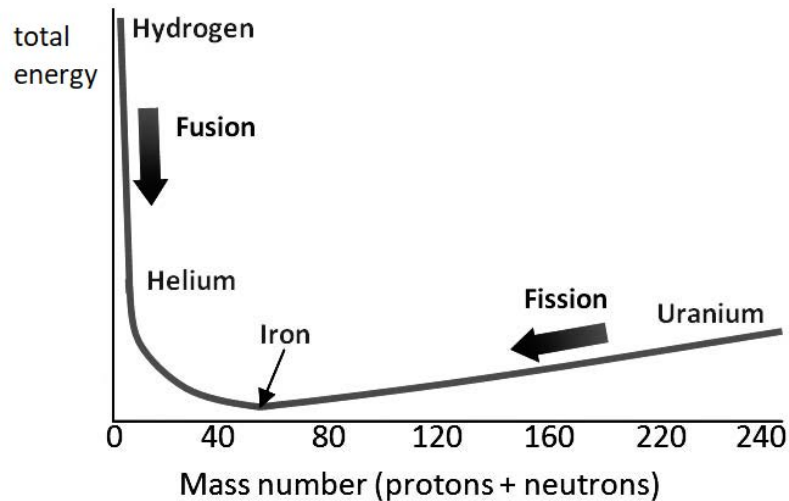


Fig. 1.3 The total nuclear energy per nucleon, combining the rest energy and the binding energy.

fusion of light elements do not generate any very long lived radioactive by-products. The natural nuclear reaction directions can be observed in Fig. 1.2.

The nuclear reactions are always going to be favourable in the direction of having a higher binding energy per nucleon. To observe the energy release behaviour, the rest mass and the binding energies of all nucleons have to be accounted together. Summing those up result in the qualitative behaviour depicted in Fig. 1.3.

In order to release energy, the nuclear reactions move into the direction of the iron element. The energy differences of the curve in Fig. 1.3 demonstrates why the fusion process, typically hydrogen into helium (because there lies the highest energy difference), generates three to four times more energy than in the fission process from uranium towards iron.

### 1.1.1 Confinement techniques

The release of energy from fusing light atoms have been known since 1920 when A. Eddington proposed the energy generation mechanism inside stars [5]. The development of the modern plasma physics started with the proposal to control the hydrogen bomb fusion reaction around 1952 [6]. Since then, various techniques have been proposed to magnetically confine a hot plasma, or more recently, the inertial confinement that starts

from a cold pellet of fuel [7]. The most successful techniques to date being the magnetic confinement devices.

The initial magnetic confinement machines were the pinch devices. All charged particles are trapped with a gyro motion around a near linear magnetic field line generated. At the extremities of the linear chamber, the plasma is confined between two magnetic mirrors. The force holding the plasma together is simply from the gradient of magnetic field in the extremities of the linear chamber. The particles moving towards the extremities decrease in the exit velocity as they feel stronger magnetic fields because the kinetic energy is transferred to the cyclotron motion. This effect occurs until they eventually turn back towards the plasma core. This principle ended up leading to high losses in the extremities because the collisional scattering forcing particles through the magnetic mirrors. To avoid these losses, the next devices were designed with a toroidal shape, connecting the ends of the magnetic field lines on themselves, resulting in toroidal magnetic field lines. Although the losses on the magnetic mirrors were extinguished, further adaptation are still necessary. The toroidal geometry results in a radial magnetic field gradient varying with  $1/R$ , where  $R$  is the major radius of the torus. All charged particles trapped in a magnetic field undergo a cyclotron motion. In the presence of the magnetic field gradient, this motion will cause a drift of the charged particles, as demonstrated in Fig. 1.4. The drifts occur because in the region with higher magnetic field the cyclotron radius is smaller, causing a tighter short turn, and the region with lower magnetic field, the turn is much longer. The magnetic field curvature in a toroidal configuration also cause drifts of the charged particles with similar amplitude and same directions. In this case, the drifts arise from the centrifugal force felt by the particles as they move along the field lines in their thermal motion. Since both effects have similar amplitude and same directions, they cannot compensate each other.

These charged particle drifts generate charge separation because each charge move in a different direction. The strong charge separation causes two major issues. First, it can lead to strong instabilities; and secondly, the vertical charge separation coupled to the perpendicular toroidal magnetic field results in a  $E \times B$  force, which unfortunately pushes the plasma outwards, ruining the confinement quality.

To solve for this charge separation, the magnetic field lines must connect the bottom region to the top region, so the charges can redistribute and neutralize themselves. Therefore it is necessary to create an additional poloidal component for the magnetic field. This poloidal component can be achieved by either twisting the toroidal field coils or by inducing a plasma current that generates a poloidal magnetic field component. When the poloidal field is generated by adapting the toroidal field coils, the device is of

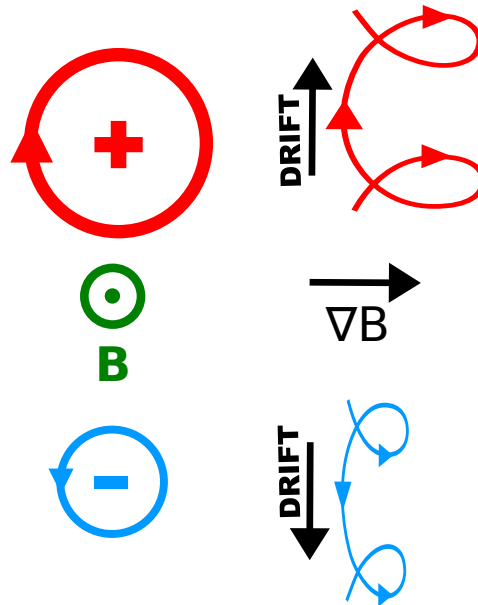


Fig. 1.4 Charged particle drifts from magnetic field gradient. The positive charges represent the plasma ions with larger cyclotron radius due to the larger mass, and the negative charges represent the electrons with smaller cyclotron radius due to the smaller mass.

a stellarator type, and when the poloidal component is induced by the plasma toroidal current, the device is of a tokamak design.

### Stellarators

There is ongoing research on several stellarator configurations. The LHD device (Large Helical Device), see [8], situated in Japan, is of the heliotron configuration and was the largest stellarator in the world since its completion in 1998 until the device W7-X (Wendelstein 7-X), see [9], of the helias configuration, started operation in Germany in the end of 2015, taking the position of the world's largest stellarator.

W7-X has a major radius of 5.5 meters and the plasma minor radius is 0.53 meters. The magnetic field in the axis is 3 Teslas.

Due to the lower confinement achieved, stellarators dragged behind until computer modelling techniques allowed refined optimization of the reactor geometries. Because stellarators have no toroidal plasma current and are able to run continuously, plasma stability is increased compared with tokamaks. Since the plasma can be more easily controlled and monitored, stellarators have an intrinsic potential for steady-state, continuous operation. The main disadvantages of this design is the typically greater aspect ratio

and the higher complexity of the machine's shape. Therefore, stellarators are much more complex than tokamaks to design and build. Nevertheless, the device W7-X has the most complicated geometry ever built, as can be seen in Fig. 1.5, and the first discharges already showed promising results. The projected field configuration and confinement quality already met the goal margins [10–12].

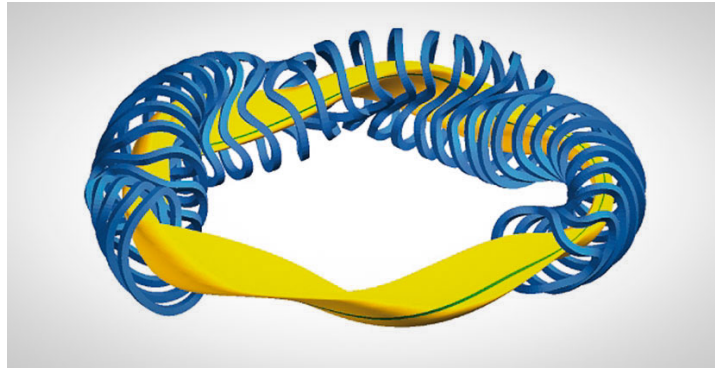


Fig. 1.5 Magnetic coils in blue and plasma shape in yellow for the stellarator Wendelstein 7-X. From Ref. [13].

The gap between experimental reactors and efficient energy generation is still larger for the stellarator designs compared to the tokamak design, since the ITER[14] tokamak will be the first reactor of its magnitude. The results of future campaigns in the stellarator W7-X is expected to shorten this gap, and can shed light in the potential of stellarator designs for the demonstration power plants, named DEMO machines[15].

## Tokamaks

The tokamak (toroidalnya kamera ee magnetnaya katushka – torus-shaped magnetic chamber) was designed in 1951 by Soviet physicists Andrei Sakharov and Igor Tamm. It is the most perfected design today with dozens of experiments in operation across the world. The largest tokamak in operation today is JET [16] with already demonstrated close to break-even condition (when the output energy equals the input energy). The next generation of reactors being built at the moment are of the tokamak design, as the ITER reactor under construction. The next generation of reactors, the DEMO reactors, are expected to follow up on the progress of ITER and demonstrate continuous electricity generation.

The basis of the tokamak design is presented in Fig. 1.6. As already mentioned, the poloidal field component is generated by the plasma current induced by the central transformer.

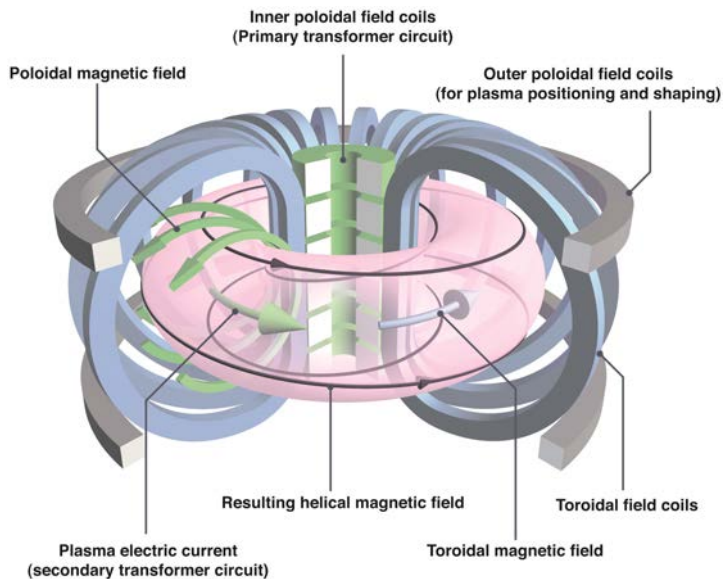


Fig. 1.6 The tokamak reactor design. The design is simplified due to the symmetrical coils and the poloidal field component is generated by the plasma current induced by the central transformer. The poloidal coils generate the toroidal magnetic field, while the toroidal coils are used to tune the plasma position. From Ref. [17]

Table 1.1 Main parameters of interest for this thesis for the tokamaks Tore Supra and WEST.

parameter	Tore Supra	WEST
plasma major radius	2.25 m	2.5 m
plasma minor radius	0.70 m	0.5 m
magnetic field on axis	4.5 T	3.7 T
plasma current	1.7 MA	1 MA

During this thesis, special attention was given to the tokamak Tore Supra [18]. It represents the magnitude of the latest generation of tokamaks, also including JET and ASDEX Upgrade [19], for example. The main features of Tore Supra are its superconducting toroidal magnets and its actively cooled first wall, enabling the research of the effects from long discharges, in the order of several minutes. Tore Supra ceased operation for upgrades and it was renamed to WEST (Tungsten (W) Environment in Steady-state Tokamak)[20]. The WEST upgrade has just completed the construction period and is being adjusted for its first campaign. The machine parameters of interest for this thesis are listed in table 1.1 for the tokamaks Tore Supra and WEST.

A cross-section comparing the two configurations is displayed in Fig. 1.7. The main changes are on the plasma facing components, changed from carbon to tungsten, and the magnetic configuration, changed from a limiter to a divertor configuration. The goals of these changes is to study the improved confinement and the materials stress of diverted plasmas on metallic environments, which is compatible to the discharges projected at the ITER tokamak.

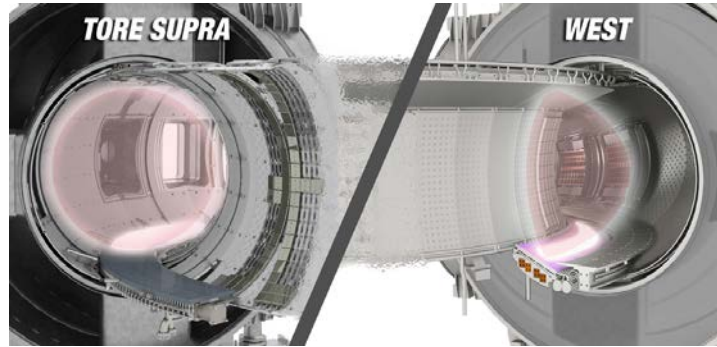


Fig. 1.7 Upgrade from Tore Supra to WEST. Left: The Tore Supra cross section, with carbon plasma facing components and a limited plasma configuration. Right: The WEST cross-section with tungsten plasma facing components and a diverted plasma configuration. From Ref. [17].

### 1.1.2 Optimization of the energy output

The most commercially advantageous fusion reaction is D+T (deuterium + tritium) because it requires a lower operating temperature to achieve a high reaction rate, as can be observed in the reaction cross-sections for three candidate reactions in Fig. 1.8.

As can be seen in Fig. 1.8 for the D-T reaction, increasing the temperature  $T$  increases the reaction rate until a maximum is achieved just below 100 keV. The final fusion output also depends on two additional factors: the plasma confinement time,  $\tau_E$ , and density  $n$ . J. D. Lawson calculated in 1955 the minimum value necessary to achieve a productive fusion reaction based on these three quantities, which is usually referred to as the triple product. This relation is known as the Lawson criteria [22] and written as:

$$n \cdot T \cdot \tau_E > 10^{21} \text{ (keV} \cdot \text{m}^{-3} \cdot \text{s)} \quad (1.1)$$

Surpassing this criterion under constant operation is the main goal of fusion research. The generation of a hot dense plasma depends only on the technological development

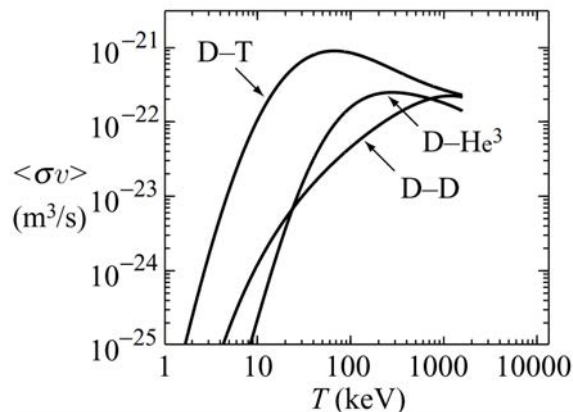


Fig. 1.8 Reaction cross-sections based on temperature for three fusion reaction candidates. From Ref. [21].

of the heating systems. Nevertheless, various different heating systems are normally employed together in conjunction. Therefore, reaching a bottleneck in one system still allows for compensation on another system, relaxing this requirement. The heating sources normally applied are: the ohmic heating by driving a toroidal current through the plasma; neutral beam injection; ion cyclotron heating; and electron cyclotron heating.

With the required density and temperature achieved, comes the most critical aspects in a fusion reactor: achieving a high energy confinement time and having the reactor chamber able to handle the power output. The development of materials to withstand the harsh environment in a fusion reactor is a dedicated research field with many challenges. Although there isn't appropriate existing materials for all parts inside the reactor, new materials are still being proposed and investigated. The materials engineering aspects are not relevant for this thesis. The last aspect is the one more connected to the research in this PhD: the confinement of the plasma. This aspect can be divided into two topics, first, is to achieve a stable confinement (avoiding ejection of plasma bursts); and second, is to have an effective confinement of the injected energy.

On the first topic, the stable confinement of the plasma is important for preventing damage to the plasma facing components. For this reason the plasma position and the edge density profile should be monitored in real-time for safety reasons in an operational reactor.

On the second topic, the energy confinement time is directly related to the radial transport of particles and heat. Understanding the transport physics allows to predict and control the energy confinement time, which enables efficient power generation in a fusion reactor. The classical transport theory assumes a random walk model due to collisions

from the inherent thermal velocity of the particles. Additional effects were incorporated in the neoclassical transport theory, where the cross-field drifts and trapped particles due to the magnetic geometry are taken into account. In the end, the observed transport in magnetic confined plasmas experiments exceeds the neoclassical expectation by an order of magnitude or more. This enhanced anomalous transport has been known for decades [23], and it is well established to be due to the fluctuations in the plasma parameters [24], also known as turbulence. Although this thesis does not focus on the turbulence mechanisms, it is important to mention that the turbulence feeds on inhomogeneities in the plasma. One of such driving mechanisms is the density gradient. Therefore, it is very important for the research in this topic to have an accurate measurement of the density profile to extract accurate effective transport coefficients. An accurate density profile enables a direct comparison between the fluctuation properties obtained from experimental data and from gyrokinetics codes (such as GYSELA and GENE). Such a comparison is of prime interest as this allows for validating both the density profile experimental assessment and the gyrokinetics models. Moreover, this contributes to better understand the various kinds of turbulent fluctuations observed in tokamak plasmas (ballooning, Ion Temperature Gradient or Trapped Electron Modes) and can be extended to ongoing study on the links between quasi-coherent modes and electron transport.

These topics discussed above show how important it is to have reliable, fast and accurate density profile measurements.

## 1.2 Main physics used in this thesis

Common density diagnostics used in fusion experiments of various sizes are the Li ion beam [25–27] and Langmuir probes [28, 29]. These techniques are not able to penetrate the dense and hot plasma core in the current generation of reactors, let alone in the next generation of reactors that are envisaging to demonstrate commercial operation. Physical probes are completely destroyed in such a harsh environment and the Li beam needs extreme power to penetrate deeper into the plasma, ceasing to be a non-perturbative diagnostic.

The only methods able to measure the full electronic density profile in a commercial fusion reactor are based on probing the plasma with electromagnetic waves. It is the only way to obtain an unperturbed measurement from the plasma edge until the hot and dense plasma core. A brief discussion on all diagnostics based on electromagnetic waves is covered in Sec. 1.3, while the focus of this thesis is on the reflectometry technique.

The physics that covers the concepts of the reflectometry technique is introduced in Sec. 1.2.1.

### 1.2.1 Waves in plasmas

The reflectometry technique is based on probing the plasma with injected electromagnetic waves. This section explains the main properties of an electromagnetic wave propagating in a plasma. The Maxwell's equations that dictate the propagation of electromagnetic waves in vacuum are:

$$\nabla \times \mathbf{E} = -\frac{\partial \mathbf{B}}{\partial t}, \quad (1.2)$$

$$\nabla \times \mathbf{B} = \mu_0 \mathbf{j} + \mu_0 \varepsilon_0 \frac{\partial \mathbf{E}}{\partial t}, \quad (1.3)$$

with  $\mathbf{E}$  being the wave's electric field,  $\mathbf{B}$  the magnetic field,  $\mathbf{j}$  the electric current,  $\mu_0$  the vacuum permeability, and  $\varepsilon_0$  the vacuum permittivity.

The dependency on  $\mathbf{B}$  can be eliminated if taking the rotational of Eq. 1.2 and inserting it in Eq. 1.3, to get:

$$\nabla \times (\nabla \times \mathbf{E}) + \frac{\partial}{\partial t} \left( \mu_0 \mathbf{j} + \varepsilon_0 \mu_0 \frac{\partial \mathbf{E}}{\partial t} \right) = 0. \quad (1.4)$$

The current term  $\mathbf{j}$  can be rewritten from Ohm's law:

$$\mathbf{j}(\mathbf{k}, \omega) = \boldsymbol{\sigma} \mathbf{E}(\mathbf{k}, \omega), \quad (1.5)$$

where  $\boldsymbol{\sigma}$  is the conductivity tensor.

Inserting Eq. 1.5 in Eq. 1.4 leads to:

$$\mathbf{k} \times (\mathbf{k} \times \mathbf{E}) + i\omega(\mu_0 \boldsymbol{\sigma} \cdot \mathbf{E} - \varepsilon_0 \mu_0 i\omega \mathbf{E}) = 0, \quad (1.6)$$

which can be rewritten substituting  $\varepsilon_0 \mu_0$  by  $1/c^2$ , as:

$$\left( \mathbf{k}\mathbf{k} - k^2 \mathbf{1} + \frac{\omega^2}{c^2} \boldsymbol{\varepsilon} \right) \cdot \mathbf{E} = 0, \quad (1.7)$$

where  $\mathbf{1}$  is the dyadic and  $\boldsymbol{\varepsilon}$  is the dielectric tensor:

$$\boldsymbol{\varepsilon} = \left( \mathbf{1} + \frac{i}{\omega \varepsilon_0} \boldsymbol{\sigma} \right). \quad (1.8)$$

Eq. 1.8 represents three homogeneous simultaneous equations for the three components of  $\mathbf{E}$ . They only have non-zero solutions when the determinant of the matrix to the left of  $\mathbf{E}$  is zero.

In order to obtain the conductivity tensor  $\boldsymbol{\sigma}$ , the ions are considered stationary, i.e. the currents originate from the electrons, the plasma is assumed isotropic, and the cold plasma approximation is also assumed. The cold plasma approximation is valid for injected electromagnetic waves travelling at phase velocities close to the speed of light in plasmas whose thermal electron speed is  $v_t \ll c$ , thus the thermal particle motions can be neglected. From these assumptions and the equation of motion for electrons, the conductivity tensor is inserted in Eq. 1.8, with the solution being the general form of the dispersion relation, known as the Appleton-Hartree formula for the refractive index  $N$ , as obtained in Ref. [30]:

$$N^2 = 1 - \frac{X(1-X)}{1-X - \frac{1}{2}Y^2 \sin^2 \theta \pm [(\frac{1}{2}Y^2 \sin^2 \theta)^2 + (1-X)^2 Y^2 \cos^2 \theta]^{1/2}}, \quad (1.9)$$

with the electromagnetic waves propagating at an angle  $\theta$  with respect to the background magnetic field, and

$$X = f_{pe}^2/f, \quad (1.10)$$

$$Y = f_{ce}/f, \quad (1.11)$$

where  $f_{pe}$  is the electron plasma frequency,  $f_{ce}$  is the electron cyclotron frequency.

Since for reflectometry the probing waves are injected perpendicular to the magnetic field direction, it is assumed  $\theta = \pi/2$ . As such, two polarization solutions remain. They are depicted in Fig. 1.9.

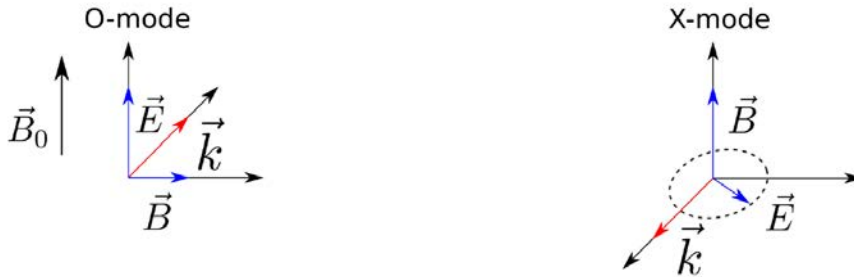


Fig. 1.9 Propagation and field directions for O-mode and X-mode polarizations. Adapted from Ref. [31].

Each electric field component can then be written for the O-mode polarization:

$$E_x = E_y = 0, \quad (1.12)$$

and for the X-mode polarization:

$$\frac{E_x}{E_y} = -i \cdot \frac{1 - X - Y^2}{XY}, \quad E_z = 0. \quad (1.13)$$

In these cases, the general refractive index solution from Eq. 1.9 reduced to, for the O-mode polarization:

$$N_O^2 = 1 - X, \quad (1.14)$$

and for the X-mode polarization:

$$N_X^2 = 1 - \frac{X(1 - X)}{1 - X - Y^2}. \quad (1.15)$$

A cut-off for a probing frequency is the point at which the refractive index goes to zero and the impinging wave is reflected. Taking  $N = 0$  in Eqs. 1.14 and 1.15, the cut-off frequency profiles can be determined for the O-mode polarization:

$$f_O = f_{pe}, \quad (1.16)$$

and for the X-mode polarization:

$$f_{L,R} = \frac{\pm f_{ce} + \sqrt{4f_{pe} + f_{ce}^2}}{2}, \quad (1.17)$$

where  $f_L$  is the left-hand polarization corresponding to the solution with the minus sign, and  $f_R$  is the right-hand polarization corresponding to the solution with the plus sign.  $f_R$  is sometimes also referred to as the upper-hybrid cut-off, for being close to the upper-hybrid resonance, or the upper cut-off, for having higher frequency than the lower cut-off  $f_L$ .

Fig. 1.10 shows an example of density and magnetic field to demonstrate what are the corresponding cut-off profiles. The cut-off profiles corresponding to this case are depicted in Fig. 1.11.

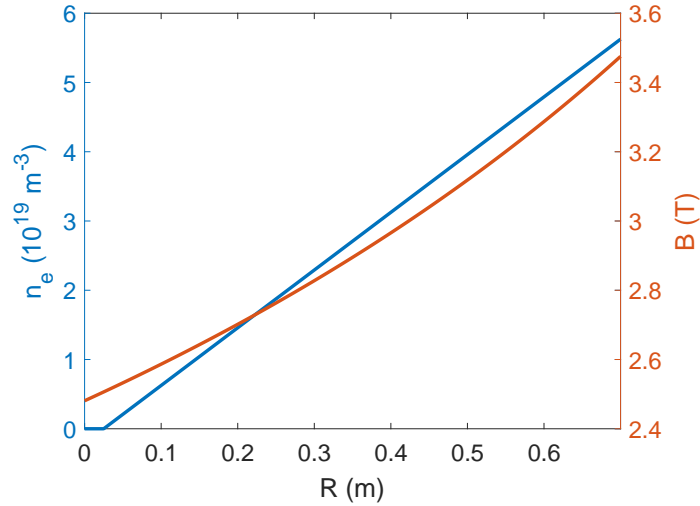


Fig. 1.10 Linear density profile from 5 cm in front the antenna to 0.7 m at the plasma center, and magnetic field profile with the typical  $1/R$  dependency and 3.5 T strength at the plasma center. The maximum density is in the order of magnitude typical of Tore Supra discharges.

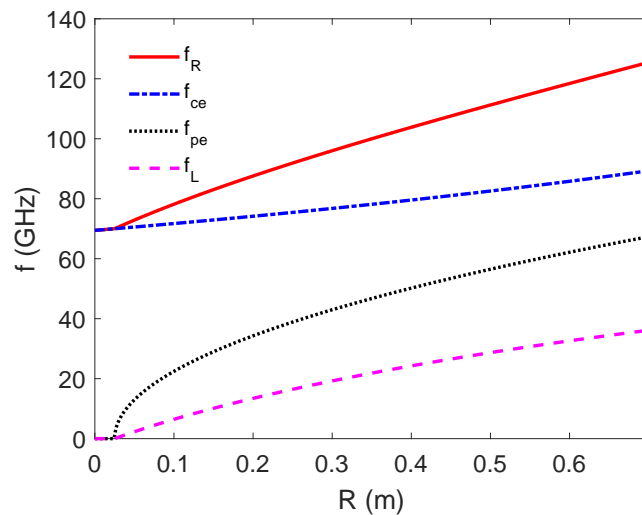


Fig. 1.11 The solutions obtained for the O-mode and X-mode cut-off profiles, based on the  $f_{pe}$  and  $f_{ce}$  profiles originating from the density and magnetic field profiles assumed in Fig. 1.10.

### 1.2.2 Wave scattering

There are many situations during a discharge that the appearance of a large perturbation can create a blind area in the cut-off profile. Such large perturbations are not well described by the traditional density profile reconstruction scheme, as investigated in Chap. 3. Chap. 4 focuses on the description of these structures from synthetic reflectometry signals. Various time-dependant full-wave features are observed on those signals, such as frequency mixing, wave tunnelling, resonances and scattering. All full-wave effects are sufficiently explained as they appear in the full-wave synthetic signals of Chap. 4, apart from the broader topic of wave scattering. This phenomenon is very frequent in the synthetic signals of Chap. 4, and also in Chap. 5.

For the density profile reconstruction algorithm, the probing waves have a clear cut-off at the first position where the probing frequency,  $f_{prob}$ , equals the cut-off frequency, i.e.  $f_R$  for the X-mode right hand polarization. However, the probing microwaves that travel through a perturbation can also be scattered. The scattering contribution plays an important role in turbulence studies. An example of spectral studies of turbulence using reflectometer signals is found in Refs. [32, 33], and another example in the link between density and phase spectra is found in Refs. [34, 35]. Even more directly connected, the scattered waves are the main contribution analysed in Doppler reflectometry [36]. This section does not aim to cover the aspects treated in these mentioned references, or to develop the current theoretical description or numerical models any further. Instead, it serves to provide a qualitative background necessary to understand the ongoing phenomena observed in the signals analysed in Chaps. 3 and 4.

Even before reaching a cut-off, the probing microwaves interact with plasma waves. The plasma waves are normally density fluctuations, but can also be magnetic field fluctuations in the case of the X-mode polarization. This interaction can lead to scattering that follow the Bragg rule:

$$k_f = 2k_{inc}\sin(\theta/2), \quad (1.18)$$

where  $k_f$  is the fluctuation wavenumber,  $k_{inc}$  is the incident probing wavenumber, and  $\theta$  is the scattering angle.

The scattering is maximized for the direction of backwards propagation. In this case,  $\theta = \pi$  and the backscattering wave meets the Bragg resonant rule:

$$k_f = 2k_{inc}. \quad (1.19)$$

When a probing wave approaches the cut-off position, the incident wavenumber  $k_{inc}$  goes to zero following the WKB approximation, leading to:

$$k_{inc} = k_0 N, \quad (1.20)$$

where  $k_0$  is the vacuum wavenumber of the probing wave and  $N$  the refractive index.

This means that the Bragg resonant condition ( $k_0 N$ ) is greater far from the cut-off location, and decreasing towards the cut-off location. This means that the farther the probing wave is from the cut-off, the larger is the fluctuation wavenumber  $k_f$  necessary to fulfil the resonant condition of Eq. 1.19. The large wavenumber translates to higher fluctuation level. Therefore, small amplitude fluctuations cause backscattering closer to the cut-off location and high amplitude fluctuations cause backscattering farther away from the cut-off location. Furthermore, this leads to the interpretation that as  $N$  decreases, the resonant condition will eventually be satisfied before the cut-off location, generating the main contribution to the phase variation. This was demonstrated for one scattering model in the one-dimensional case either analytically in Ref. [37] and numerically in Ref. [38].

An initial study on the various scattering regimes was introduced in Ref. [39] for the O-mode polarization in 1D. The analytical expressions for the scattering amplitude led to Ref. [40] to include an analysis of the maximum phase variations for different perturbation shapes. A feature that enables a better interpretation of the incident wavenumber in respect to the Bragg condition close to the cut-off, is the description of the incident wavenumber by the Airy functions, i.e. the Airy wavenumber,  $k_A$ , which corresponds to an area where the WKB solution does not describe well the probing wave. The Airy wavenumber is directly proportional to the vacuum wavenumber and the local density gradient length.

The different scattering regimes observed in Ref. [40] were distinguished as:

1. **Small wavenumbers**, when  $k_f \ll k_0$ . In this case, the scattering is only originated in the cut-off vicinity. By computing the Airy wavenumber at the cut-off location, the fact that  $k_f < k_A$  dictates that the Bragg resonant rule is never satisfied along the entire wave propagation. In this case, any phase modulation is only due to the oscillation of the cut-off layer.
2. **Large wavenumbers**, when  $2k_A < k_f < 2k_0$ . This regime can still be separated into two cases, i) spatial; and ii) spectral.

In the large wavenumber case, for the condition that  $k_f \gg 2k_A$ , Bragg scattering is expected to occur. The distinction between the two regimes is made by comparing the half-wavelength of the perturbation,  $l_f$ , to a critical length, defined as:

$$l_c^2 = \frac{Lk_f}{k_0^2}, \quad (1.21)$$

with  $L$  being the local density gradient length.

When  $l_f > l_c$ , the scattering is of the spatial case, and when  $l_f \ll l_c$ , it is of the spectral case. In the spatial case, the phase modulations reproduce the spatial shape of the fluctuation, whereas in the spectral case, the phase modulations reproduce the spectral features of the perturbation. Furthermore, for a less physical but interesting perturbation shape containing sharp edges, like a square wheel, the broad spectrum of the perturbation translates into a broad spectrum in the phase modulations.

The analytical description of the backscattering regimes has been extended in Ref. [41] to the X-mode polarization. The stable/unstable regimes were computed by the Mathieu equation, and the backscattering amplitude could be computed applying the Floquet theorem.

A result that was demonstrated for both O and X polarizations, in Refs. [40] and [41], respectively, is that the efficiency of the scattering decreases as the fluctuation becomes farther from the cut-off.

High amplitude perturbations have already been reported in two occasions to be able to produce strong scattering in non-linear regimes. First, demonstrated analytically in 1D for backscattering in ITER scenarios for O and X-mode with 0.5 – 2% density fluctuation level, and secondly, demonstrated numerically in 2D for specific forward scattering scenarios with fluctuation levels above 5% in oblique incidence for Doppler reflectometry. Even though it is much less efficient to satisfy the forward scattering condition, it was observed that for very large fluctuation levels and long propagation paths, a process of cumulative forward scattering can also take place [42]. This process was inferred in simulations with fluctuation levels above 5%, because the cumulative forward scattering can be trapped in cavities created by such large perturbations, as seen in Ref. [43].

The main application of interest for this thesis on the scattering waves is on the signals from large perturbations that introduce blind areas to the frequency swept signal. Although these fluctuations are of large amplitude, they have a typical wavelength much larger than the probing wavelength in vacuum. Therefore, any spectral resonance between the probing wavenumber and the perturbation wavenumber is going to be due to a localized broad spectrum of the perturbation shape. Therefore, smooth narrow

band perturbations have much less scattering compared to the broad spectrum of sharp boundaries like the square wheel example.

As a first step to the investigation of the reconstruction initialization and the reconstruction over blind areas, only a one dimensional code is employed to simplify the analysis. As such, all geometrical effects are neglected. They can appear in the form of focusing or defocusing of the probing beam, or in mode conversions (as demonstrated in the presence of density and magnetic fluctuations in Refs. [44, 45]). It is also clear from observing Eq. 1.18 that not all values for  $\theta$  are possible in 1D. In fact, only zero and  $\pi$  are possible, simplifying the obtained solution.

In principle, the scattered waves can be analysed related to the perturbation shape and size directly. However, due to the large perturbations of interest in this thesis, the scattering produces more localized information along the perturbation instead of a full picture of the perturbation at once. As it was mentioned, the efficiency of the scattering is higher when probing closer to the cut-off, causing parts of the perturbations to be much more efficient in producing scattering than others. Furthermore, due to the inherent noise levels of the observed experimental signals, the information from the scattering contribution are partially destroyed. Also adding the fact that the 1D model is used in this thesis as a first approach to this problem, it gives a very simplified picture of an experimental situation. Therefore, the scattering information is not used to determine features of the perturbation in this first approach. In the future, if further features of the perturbations are needed and the scattered amplitude can be confirmed to be above the noise levels, this quantitative approach can be investigated using a 3D time-dependant code. This approach falls onto the inverse scattering problem [46], as it also appears in the solitons theory, e.g. in Ref. [47].

### 1.3 Non-perturbative density diagnostics

As already mentioned in Sec. 1.2, the dense and hot core plasmas in current generation tokamaks and future power plants are only accessible via electromagnetic waves. The current techniques that employ electromagnetic waves to infer the density profiles are Thomson scattering, interferometry and reflectometry. Both the Thomson scattering and interferometry techniques probes the plasma with a much higher frequency than the reflectometry technique. Therefore, unlike the reflectometry technique, the probing waves do not find a cut-off along the propagation path.

The Thompson scattering diagnostics relies on the incoherent scattering of a laser (usually a Nd:YAG laser with  $\lambda = 1064nm$ ) by the plasma electrons. The electron

density is computed from the amplitude of the signal. The electron temperature is also recovered from the signal's spectral width. Because incoherent scattering is inefficient, powerful pulsed laser ( $>1\text{J}$  per pulse) are used to rise the signal above the background noise level. The laser repetition rate (typically 30 Hz) impose the time resolution. The spatial resolution is set by the spot size of the optical system along the beam path. In the low density and temperature edge region, the cross-section is even lower and the signal to noise ratio is much degraded. Systems have been developed with more than a hundred viewing lines and several lasers that provided increased time resolution. Thomson scattering diagnostics are installed on almost all tokamaks as they provide simultaneous local density and temperature measurements. However, the noise level is high compared to other techniques. The poor time resolution makes this diagnostic unsuitable for studies involving fast profile evolution and real-time profile monitoring.

Like reflectometry, interferometry is based on the phase delay induced by crossing the plasma. However, interferometry works at much higher frequency, well above any plasma cut-off. The line integrated density along the line of sight is proportional to the phase increment, which is proportional to the average refractive index along the probing path. The line integrated density accuracy is very good, in the order of  $10^{17}\text{m}^{-3}$ , and it is typically used for real-time plasma control and energy confinement time calculations.

By using various probing paths, the multi-chord interferometry is able to measure the density radial profile. The time resolution can be as high as  $1\mu\text{s}$ , but the radial resolution and accuracy is poor due to the limited number of lines (usually  $\leq 10$ ) and the inversion process, which assumes a homogeneous density over each flux surface. In Tore Supra, the interferometry provided density profiles with 11 radial positions and typically millisecond time resolution [48].

The reflectometry technique is the only diagnostic able to perform a fast acquisition across the full profile length and provide a localized measurement. The localized characteristic is paramount for turbulence studies that require the local density gradient and fluctuation spectra.

### 1.3.1 Basic principles of reflectometry

The probing microwaves propagate from outside the plasma, thus the density increases along the path until a position where the refractive index goes to zero, a cut-off position, and the injected wave is reflected. The reflected wave is detected back in the antenna for processing. In the typical pulse radar application, the time-of-flight measured is directly proportional to the distance travelled, since the medium has a constant refractive index and the probing frequency is fixed. In the profile reflectometry case, on the other hand,

the frequency is swept and the refractive index changes along the propagation path. These features add significant complexity to the data interpretation.

For determination of the density profile, the probing frequency is continually swept in order to detect many cut-offs along the plasma radius. This system is called FMCW (Frequency Modulation Continuous Wave). With the hardware advancements it is becoming possible to perform much quicker sweeps. The latest generation of the Tore Supra reflectometers achieved a sweep as fast as  $1 \mu s$ , and are now referred to as an ultrafast sweep reflectometer [49].

To determine a density profile two quantities must be computed: the cut-off density and the radial position corresponding to each cut-off. This procedure depends on the polarization of the probing waves. First, the density of at the cut-off is discussed, and after, the procedure to determine the radial positions.

For the O-mode polarization, the cut-off frequency is the plasma frequency, giving the electron density at the cut-off directly from the probing frequency by isolating the electron density,  $n_e$ , in Eq. 1.22:

$$f_{pe} = \frac{1}{2\pi} \sqrt{\frac{e^2 n_e}{m_e \varepsilon_0}}, \quad (1.22)$$

where  $e$  is the electron charge,  $m_e$  the electron mass, and  $\varepsilon_0$  the permittivity in vacuum.

For the X-mode polarization, the cut-off frequency is a function of both the plasma frequency and the cyclotron frequency. The electron cyclotron frequency profile,  $f_{ce}$ , is calculated from the magnetic field profile,  $B$ , since  $f_{ce} = eB/m_e$ . The magnetic field must be determined by other diagnostics. After applying the inversion method to determine the radial position of the cut-off, the value of  $f_{ce}$  is determined and the electron density is computed from isolating  $f_{pe}$  in Eq. 1.17, with the cut-off frequency  $f_{L,R}$  substituted by the probing frequency.

The inversion technique that computes the cut-off positions from the reflectometry signal is not discussed in this chapter. It is treated in Chap. 3. Instead, this section describes the reflectometry signals available for analysis.

The injected microwaves can be described as:

$$S_0(t) = A_0(t) \cos[\varphi(t)], \quad (1.23)$$

where  $A_0$  is the injected wave's amplitude and  $\varphi(t)$  is the wave's phase.

Because the amplitude varies much slower than the phase, the probing frequency can be written as:

$$f(t) = \frac{1}{2\pi} \frac{\partial \phi(t)}{\partial t}, \quad (1.24)$$

which inserted in Eq. 1.23 results in:

$$S_0(t) = A_0(t) \cos \left[ 2\pi f_0 t + \pi \frac{f_1 - f_0}{T_{sweep}} t^2 \right], \quad (1.25)$$

with  $T_{sweep}$  being the sweeping period taken to sweep from the initial frequency  $f_0$  until the frequency  $f_1$ .

The sweeping rate,  $V_s$ , can be defined as:

$$V_s = \frac{f_1 - f_0}{T_{sweep}}. \quad (1.26)$$

Then, the probing frequencies can be rewritten as:

$$f(t) = f_0 + \frac{f_1 - f_0}{T_{sweep}} t = f_0 + V_s t. \quad (1.27)$$

After injecting the frequency modulated signal, the microwaves propagate into plasma until they reach a cut-off; one for each probing frequency. Then, these waves with incremented phase are detected back at the reflectometer antenna. However, it is not technologically possible today to resolve a signal in the tens of GHz range. So, the injected signal is split and one part is sent to a reference wave guide. The reference waveguide is used to delay the reference signal to compensate for the propagation time across the waveguides and vacuum, and reunite in time with the signal injected after the propagation through the plasma. The injected signal that propagated through the plasma is named  $S_{in}$ , and the reference signal is named  $S_{ref}$ . Using the expression in Eq. 1.27, these signals can be written as:

$$S_{in}(t) = A_{in}(t) \cos \left[ 2\pi f_0 t + \pi \frac{f_1 - f_0}{T_{sweep}} t^2 - \phi_{in}(t) \right], \quad (1.28)$$

$$S_{ref}(t) = A_{ref}(t) \cos \left[ 2\pi f_0 t + \pi \frac{f_1 - f_0}{T_{sweep}} t^2 - \phi_{ref}(t) \right]. \quad (1.29)$$

Then, the two signals go through a mixer, resulting in  $S(t)$ :

$$S(t) = S_{in}(t) \times S_{ref}(t), \quad (1.30)$$

$$S(t) = \frac{A_{in}(t)A_{ref}(t)}{2} \times \left\{ \cos \left[ 4\pi f_0 t + 2\pi \frac{f_1 - f_0}{T_{sweep}} t^2 - \phi_{in} - \phi_{ref} \right] + \cos \left[ \phi_{in} - \phi_{ref} \right] \right\}.$$

The second cosine is much lower in frequency, containing only the additional phase from propagating through the plasma, while the first cosine contains the higher frequencies from the probing and sweeping frequencies (the carrier frequencies). In order to extract the contribution from the plasma propagation the signal goes through a low-pass filter, removing the contribution from the left cosine. Consequently, the resulting signal can be written as:

$$S(t) = \frac{A_{in}A_{ref}}{2} \times \cos \left[ \phi_{in} - \phi_{ref} \right], \quad (1.31)$$

and the phase increment from propagating through the plasma:

$$\phi_{plasma} = \phi_{in} - \phi_{ref}. \quad (1.32)$$

This phase can be extracted simply by taking the angle of the signal in Eq. 1.31. The angle extraction, if performed in Matlab, comes in the range  $[-\pi, \pi]$ . To obtain the complete phase evolution, it's still necessary to be unwrap it, by adding  $2\pi$  every time the signal jumps from  $\pi$  to  $-\pi$ . The phase increment signal is the information necessary for the profile reconstruction techniques discussed in Chap. 3.

The frequency that is obtained from the phase increment  $\phi_{plasma}$  is named the beat frequency,  $f_b$ , which according to Eq. 1.24 can be written as:

$$f_b(t) = \frac{1}{2\pi} \frac{\partial \phi_{plasma}}{\partial t} = \frac{\partial \phi_{plasma}}{\partial f} \frac{\partial f}{\partial t} = \tau(f) \times V_s, \quad (1.33)$$

with the quantity  $\tau(f)$  being the time-of-flight. The time-of-flight of each frequency represents the time taken for that frequency to propagate to the cut-off position and back to the antenna.

### 1.3.2 I/Q demodulation

The heterodyne reflectometry systems allow to demodulate the phase and amplitude separately by the I/Q method[49, 50]. The I/Q demodulator generates a cosine and a sine signals, equivalent to Eq. 1.31. This way the phase and the amplitude can both be determined, according to these expressions:

$$A(t) = \frac{1}{A_0} \sqrt{S_{\sin}^2 + S_{\cos}^2}, \quad (1.34)$$

$$\phi(t) = \arctan(S_{\sin}/S_{\cos}). \quad (1.35)$$

The amplitude information is used in the analysis of blind areas in the cut-off profile, as discussed in Chap. 4, and also in the investigations on the initialization position, as discussed in Chap. 5.

Some noise sources in reflectometry are easily distinguished from the injected microwaves if the signal is analysed in the frequency domain. These can be trapped waves or additional reflections on the antenna region, for example. The reflectometer signal can be observed in the frequency space by taking the spectrogram of the complex signal  $Ae^{j\phi}$ . This signal can be used as a guide to check if any additional reflection is present and need any additional filtering. The filtering technique is based on the tomographic analysis demonstrated in Refs. [51, 52]. In order to illustrate an example with all the reflectometer information, Fig. 1.12 shows a time-of-flight signal from a synthetic signal probing the core plasma for a simple linear density profile on a background magnetic field of 4 Teslas.

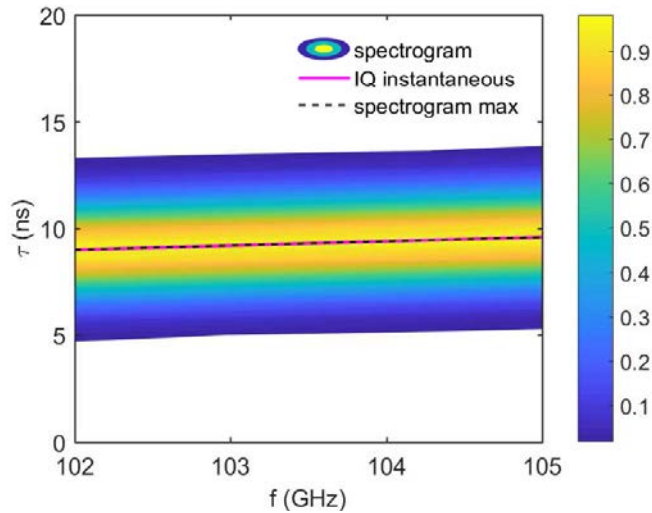


Fig. 1.12 Simplest example of the reflectometer time-of-flight signals, illustrating synthetic noiseless signals from probing the plasma core of a linear density profile on a background magnetic field of 4 Teslas. The amplitude on the spectrogram is normalized, as shown in the colorbar.

The spectrogram signal is obtained just as mentioned above, using the spectrogram of the complex reflectometer signal. The output of the spectrogram gives the beat frequency, which can be directly translated to time-of-flight using Eq. 1.33. The IQ instantaneous signal is directly the measured phase, given by Eq. 1.35, or by taking the angle of the complex signal, which in this case was then transferred to time-of-flight by Eq. 1.33. The spectrogram max signal is just the maximum of the spectrogram. This signal can be used as a guiding center for the tomography filtering technique.

Fig. 1.12 is not intended to show any particular feature at this moment, it only serves to demonstrate what is the obtained signals from the techniques described above. It is a simple noiseless synthetic signal from probing a linear profile without any fluctuations. Surely in this case the instantaneous signal matches well the spectrogram max signal, but as will be seen in the next chapters, this will not always be the case. The analyses on the reflectometer signal are always based on observing the compatibility between these signals. Any additional reflections, trapped waves and frequency mixing event become clear in the spectrogram graph. When these events can be identified in the spectrogram, the filtering techniques can be applied to try to isolate the main branch from the additional, normally unwanted, contribution. In the end, after applying the optimized filtering techniques aided by the spectrogram graph, the instantaneous signal is used for further analysis. The spectrogram is normally only used as a guide to improve the instantaneous filter due to the inherent higher resolution on the instantaneous signal.

The accuracy obtained on a reflectometry density profile depends on the quality of the signal (how clean the signal is from additional reflections, polarization and noise), the data extraction method and on the data analysis methods. The quality of the signal rely on the experimental design and the discharge conditions. The design of reflectometry systems is not in the scope of this thesis. The data extraction methods have already undergone significant improvements, as demonstrated in Refs. [51, 52]. The focus of this thesis is on the data analysis aspect.

The accuracy of the reconstructed density profiles depends on three factors from the data analysis: *i*) the inversion method from the phase increment to the density profile; *ii*) the description of local perturbations; and *iii*) the technique to determine the first profile position. Each of these topics are investigated in detail in the Chaps. 3, 4 and 5, respectively. The inversion method that determines the density profile does not take into account any features in the initialization or the description of blind areas, which is why these topics can easily be treated separately.

## 1.4 Objectives and outline of this thesis

As already mentioned in Sec. 1.1.2, it is necessary to monitor and investigate the confinement quality in fusion plasmas to optimize the energy output. Thus, it is clear how paramount it is to have good density profile measurements that can operate in reactor conditions. To this end, a radar-based method called “reflectometry” has been developed during the past decades and is now widely used in current experiments. Reflectometry will be an essential diagnostic for ITER as it will provide electron density measurements in the plasma edge and divertor regions with high spatial and temporal resolutions. Among the various existing reflectometry techniques, the fast frequency sweeping system is particularly important, as it is able to continuously probe the density and its fluctuations from the far scrape-off layer up to the core plasma. One relevant system to the topics developed here is the low field side X-mode reflectometer. Its first operation priority is to measure the density profile with the desired minimum spatial accuracy of 5 mm[53]. Although the technical capabilities of such diagnostics are promising, the reliability of derived physical quantities can be limited by the difficulties of interpreting the reflectometer signal. The reconstruction of electron density profile is usually affected by various kinds of uncertainties, including, for example, systematic radial shifts. The improvements on the reflectometry diagnostics becomes more crucial for each new generation of machines and to follow up the transport research. The goal of this PhD is to evaluate and improve as much as possible all the factors that contribute to the final accuracy of the density profile, in the point of view of the data analysis.

The theoretical maximum experimental accuracy of a reconstructed profile has already been shown [54, 55]. The experimental reflectometer design and the data extraction techniques have seen significant improvement in the last two decades, see [56, 57]. However, no systematic evaluation of the accuracy from the data analysis point exists to date. This thesis aims to evaluate the data analysis current status and work on improvements on it. In order to evaluate and improve the profile accuracy, three aspects are explored in the data analysis front.

The first aspect is the recursive method used to compute the reflection positions of each probing frequency. Currently, there is no publication that presents a systematic evaluation on the accuracy of the profile reconstruction algorithm. The algorithm currently in use for the X-mode polarization was firstly introduced in 1987 by Bottollier-Curtet [58] and has been the standard reconstruction algorithm ever since, with only minor revision. This topic is investigated in Chap. 3.

The second aspect is the identification and description of blind areas in density depletion zones. This issue has never been taken into account so far. It is investigated in Chap. 4 and it is applicable to both X and O-mode polarizations.

The third and last topic, is the initialization of the profile reconstruction in X-mode. It is currently performed as published in the Refs. [51, 57], and is subject to an error of up to 1 cm [57] in Tore Supra depending on the measurement conditions. The set-up in Tore Supra is well optimized, specially because the antenna is far from the plasma edge. Other less optimized set-ups can result in even higher initialization errors. This topic is further investigated in Chap. 5.

All topics mentioned above are to be investigated with synthetic data in the first approach. Only with synthetic data the accuracy of a reconstructed profile can be inferred. After developing the reconstruction methods, the next step is to demonstrate the improved reconstruction techniques in realistic experimental scenarios, using previous discharges from the database of the Tore Supra and JET tokamaks. After these methods are successfully demonstrated, they will be implemented in the data acquisition routine in the WEST tokamak, and in the future, in ITER.

# Chapter 2

## Numerical tools to simulate the reflectometer signals

### 2.1 Simulations using the WKB approximation

Under the WKB approximation, the refractive index ( $N$ ) goes to zero as the probing wave goes to the cut-off position. At the cut-off position, the wave is reflected back with an additional  $\pi/2$  in phase. On a plasma with electronic frequency profile  $f_{pe}$ , over a background magnetic field resulting in an electronic cyclotron profile  $f_{ce}$ , the phase increment for a probing frequency  $f$  over a path from  $A$  to  $B$  can be written, as given in Ref. [30]:

$$\phi(B) - \phi(A) = \frac{2\pi f}{c} \int_A^B N(f, f_{pe}(x), f_{ce}(x)) dx, \quad (2.1)$$

where  $c$  is the speed of light.

For the X-mode polarization, the refractive index can be written as:

$$N = \sqrt{1 - \frac{X(1-X)}{1-X-Y^2}}, \quad (2.2)$$

with

$$X = \frac{f_{pe}^2}{f^2}, \quad Y = \frac{f_{ce}}{f}. \quad (2.3)$$

In order to simulate the phase measurement of a frequency swept reflectometer, the Eq. 2.1 can be computed for all probing frequencies along the probing path. Each frequency has a unique cut-off location that has to be determined beforehand in order to know the integration path. For each probing frequency, the algorithm typically scans the propagation path until the condition  $f_{prob} = f_{cutoff}$  is satisfied for the first time. After each cut-off is located, the algorithm computes the corresponding phase and moves to the next probing frequency. This is how the signal  $\phi(f)$  is computed.

## 2.2 1D full-wave wave equation solver

In order to account for full-wave effects in the simulated phase-shift and time-of-flight signals, 1D full-wave codes were used to simulate the microwave propagation across the plasma. Initially, a stationary code was used based on the resolution of the Helmholtz equation for a purely monochromatic wave [59]. However, the main interest for the research in this thesis is on frequency swept reflectometry. In this case, the time-dependant effects of the frequency sweep plays an important role on the simulated signals. Therefore a time-dependant 1D wave equation solver code was used for all the signals computed and displayed throughout this thesis. The code used was developed in Ref. [41].

The initial assumptions to develop the code were *i)* the cold plasma approximation, i.e. the plasma thermal velocity is small compared to the probing wave phase velocity; *ii)* high frequency fields, i.e. only the high frequency electromagnetic fields are taken into account. Which means that the movement of ions and neutrals are negligible compared to the electrons, and therefore are not taken into account. *iii)* non-dissipative media, i.e. external currents and collisions are neglected, making the plasma a non-dissipative media.

The system of equations to be solved involves the simultaneous resolution of the electron movement equation, given in Eq. 2.4, and the wave propagation equation that is derived from the Maxwell's equations, as given in Eq. 1.6.

$$m_e \frac{\partial \vec{v}}{\partial t} = -e\vec{E} - e\vec{v} \wedge \vec{B}, \quad (2.4)$$

where  $m_e$  is the electron mass and  $\vec{v}$  the electron velocity.

In the unidimensional case, the coupled equations to be solved can be written as a system of four equations:

$$\begin{aligned}
\left[ \frac{\partial^2}{\partial t^2} + \omega_{pe}^2 \right] E_x &= -\omega_{pe}^2 B_0 v_y, \\
\left[ \frac{\partial^2}{\partial t^2} - c^2 \frac{\partial^2}{\partial x^2} + \omega_{pe}^2 \right] E_y &= \omega_{pe}^2 B_0 v_x, \\
\frac{\partial v_x}{\partial t} &= -\frac{e}{m_e} E_x - \omega_{ce} v_y, \\
\frac{\partial v_y}{\partial t} &= -\frac{e}{m_e} E_y - \omega_{ce} v_x,
\end{aligned} \tag{2.5}$$

with  $\omega_{pe}$  and  $\omega_{ce}$  as functions of the radius, and the field and velocity components as functions of the radius and time.

To simulate the propagation of waves into the plasma, the profiles of  $\omega_{pe}$  and  $\omega_{ce}$  are defined and kept constant during the simulation. A space before and after the plasma is set to be vacuum. This way the perfectly matched boundary can be set to absorb any reflected waves or any wave that crossed the full simulation domain. In the initial vacuum zone, the injected microwaves can be defined as an electric field on the  $E_y$  component and must obey the condition:

$$\frac{\partial}{\partial t} E_y(x, t = 0) = -c \frac{\partial}{\partial x} E_y(x, t = 0). \tag{2.6}$$

Since the cold plasma model is assumed, no initial thermal velocity is set for the electrons.

To improve the code stability, it was assumed  $1 - c^2 \frac{\delta t^2}{\delta x^2} = 0$ , and to minimize the numerical dispersion, it was assumed  $\delta x = \delta t \implies c^2 = 1$ . Furthermore, to simplify the system of equations, the field and velocity components have been normalized as:

$$\tilde{v}_x = \frac{v_x}{v_D}, \quad \tilde{v}_y = \frac{v_y}{v_D}, \quad \tilde{E}_x = \frac{E_x}{E_0}, \quad \tilde{E}_y = \frac{E_y}{E_0}, \tag{2.7}$$

where  $v_D = \frac{E_0}{B_0}$  is the electron drift velocity and  $E_0$  is the injected electric field amplitude.

The field component  $E_y$  was discretized with a third order finite difference scheme, resulting in:

$$E_i^{j+1} = \frac{1}{1 + \frac{\omega_{pe}^2(i)}{4}} \left[ E_{i+1}^j + E_{i-1}^j \frac{\omega_{pe}^2(i)}{2} E_i^j + \omega_{pe}^2 v_{xi}^j \right] - E_i^{j-1}, \tag{2.8}$$

with  $i$  being the discretization in space, and  $j$  in time.

The field component  $E_x$  was discretized following the fourth order Numerov method, with the second derivative on time of the  $E_x$  approximated by a fourth order Taylor series. The resulting  $E_x$  component is then written as:

$$E_i^{j+1} = \frac{2 - \frac{5}{6}\omega_{pe}^2}{1 + \frac{\omega_{pe}^2}{12}} E_i^j - E_i^{j-1} \frac{\omega_{pe}^2}{1 + \frac{\omega_{pe}^2}{12}} v_{yi}^j. \quad (2.9)$$

The coupled velocity components starts with the following equations:

$$\frac{\partial \tilde{v}_x}{\partial t} = -\omega_{ce} \tilde{E}_x - \omega_{ce} \tilde{v}_y, \quad (2.10)$$

$$\frac{\partial \tilde{v}_y}{\partial t} = -\omega_{ce} \tilde{E}_y - \omega_{ce} \tilde{v}_x. \quad (2.11)$$

To continue with a simpler notation, these components are re-written as:

$$\begin{aligned} \tilde{v}_x(t) &= f(\tilde{E}_x, \tilde{v}_y), \\ \tilde{v}_y(t) &= g(\tilde{E}_y, \tilde{v}_x). \end{aligned} \quad (2.12)$$

Applying the fourth order Runge-Kutta scheme [60], over a step  $h$  in time that is equal to  $\Delta t$ , the velocity components are discretized as:

$$\begin{aligned} \tilde{v}_x(t+h) &= \tilde{v}_x(t) + \frac{1}{6}(k_1 + 2k_2 + 2k_3 + k_4), \\ \tilde{v}_y(t+h) &= \tilde{v}_y(t) + \frac{1}{6}(l_1 + 2l_2 + 2l_3 + l_4), \end{aligned} \quad (2.13)$$

with the  $k$  and  $l$  components given by:

$$\begin{aligned} k_1 &= hf \left[ \tilde{E}_x(t), \tilde{v}_y(t) \right], & l_1 &= hg \left[ \tilde{E}_y(t), \tilde{v}_x(t) \right], \\ k_2 &= hf \left[ \tilde{E}_x(t+h/2), \tilde{v}_y(t) + l_1/2 \right], & l_2 &= hg \left[ \tilde{E}_y(t+h/2), \tilde{v}_x(t) + k_1/2 \right], \\ k_3 &= hf \left[ \tilde{E}_x(t+h/2), \tilde{v}_y(t) + l_2/2 \right], & l_3 &= hg \left[ \tilde{E}_y(t+h/2), \tilde{v}_x(t) + k_2/2 \right], \\ k_4 &= hf \left[ \tilde{E}_x(t+h), \tilde{v}_y(t) + l_3 \right], & l_4 &= hg \left[ \tilde{E}_y(t+h), \tilde{v}_x(t) + k_3 \right]. \end{aligned}$$

### 2.2.1 Code's numerical dispersion

The code was thoroughly validated in Ref. [41] when comparing the code solution to well-known theoretical solutions. The code error was always below 1% when discretizing the injected waves using 50 points per wavelength at the highest probing frequency. Nevertheless, it is useful to observe the numerical dispersion for the typical cases of interest in this thesis in order to optimize the code's execution time and verify the obtained numerical error.

The numerical dispersion can be observed when plotting the normalized wave amplitude after propagation through the plasma. First, the dispersion is observed for varying values of points per wavelength, as presented in Fig. 2.1. Next, Fig. 2.2 shows the dispersion obtained for varying values of the injected wave's frequency sweeping rate.

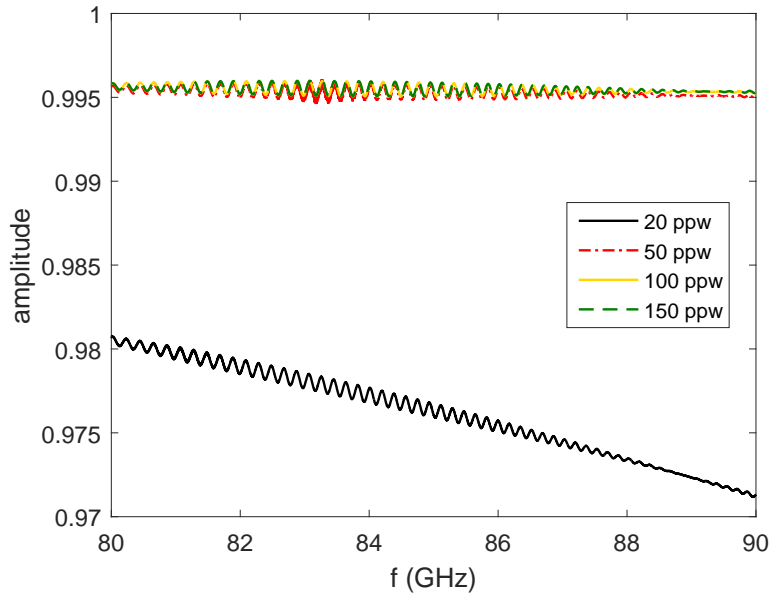


Fig. 2.1 Effect of numerical dispersion from the choice of the number of points per wavelength for the simulation of a linear density profile and 50 GHz/us frequency sweeping rate.

More than 2% dispersion is observed if using only 20 points per wavelength for the simulation. Increasing the number of points per wavelength decreases the numerical dispersion until it saturates at around 100 points per wavelength with the signal's dispersion of less than 0.5%. For the sweeping rate dependency, less than 0.5% dispersion is observed if sweeping the probing frequency at 50 GHz/us, which is faster than any existing device. Sweeping the frequency much faster will increase the numerical dispersion,

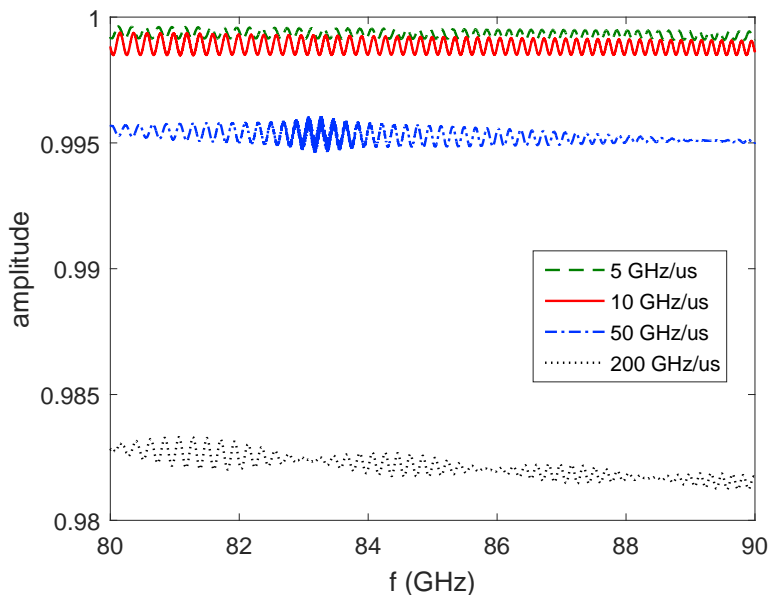


Fig. 2.2 Effect of numerical dispersion from the frequency sweeping rate used in the simulation of a linear density profile and fixed 50 points per wavelength.

which is just below 2% when sweeping at 200 GHz/us. An additional tool explored to decrease the numerical dispersion, was to use variables with quadruple precision. Although a decrease of the numerical dispersion was observed, the computational cost to run quadruple precision variables turned out to be much greater than increasing the number of points per wavelength.

The methods investigated in this thesis are aimed at their application in the latest generation and next generation devices. As such, the sweeping rate used is typical of the fastest sweeping rate available today, around 20 GHz/us. With these dispersion results in mind, all results analysed in this thesis were performed with 50 points per wavelength to obtain numerical dispersions below 0.5%.

### 2.3 Phase and time-of-flight extraction

When running the code developed above, the wave propagation in time is simulated. There is still the task of extracting the reflectometer signal afterward. The first approach to determine the phase evolution of the full-wave simulations was to count the zeros of the electric field amplitude at the output signal in the vacuum zone. The obtained phase evolution was accurate, specially if fitting the zero crossing point or increasing the number

of points per wavelength in the code. However, this method does not work well when the reflected signal contain fluctuations or fast phase variation. Even worse if the reflected signal is not monochromatic. It is common to have frequency mixing if the cut-off profile is not monotonic. In such cases, a method that can take into account the different frequencies has an enormous advantage. The I/Q demodulation technique[49, 50] for heterodyne reflectometry is capable of handling multi reflection cases. Furthermore, since this is the method applied in experimental signals, if the numerical signals are extracted with the same technique, they can be directly compared to each other. For these reasons, this is the data extraction technique used in the synthetic signals throughout this thesis.

In order to use the I/Q data extraction technique, the code computes a sin and a cos signal propagation simultaneously. With these signals, the I/Q demodulator can be replicated by constructing the I/Q sine and cosine outputs as:

$$\begin{aligned} S_{\cos}(t) &= S_{\cos}^{inj} S_{\cos}^{ref} + S_{\sin}^{inj} S_{\sin}^{ref}, \\ S_{\sin}(t) &= S_{\cos}^{inj} S_{\sin}^{ref} - S_{\sin}^{inj} S_{\cos}^{ref}, \end{aligned} \quad (2.14)$$

where  $S^{inj}$  refers to the injected signal and  $S^{ref}$  refers to the reflected signal. In order to replicate the experimental delay line on the reference signal, the reflected signal has to be subtracted by the vacuum propagation period.

With the sine and cosine contributions, the I/Q signals can be computed exactly the same way as for the experimental data, as introduced in 1.3.2, resulting in signals compatible with the ones displayed in Fig. 1.12.



# Chapter 3

## X-mode inversion methods

### 3.1 Introduction

The aim of this chapter is devoted to the improvement of the density profile reconstruction method using X-mode reflectometry. The initial ideas developed here were presented in the Refs. [61–63], and the final results have been published in Refs. [64, 65].

The reconstruction method published by Bottollier-Curtet and Ichchenko in 1987 [58] has been the standard method of density profile reconstruction method ever since, with only minor revision. Although it is theoretically possible to increase the accuracy of the reconstructed profile simply by increasing the number of frequencies considered for the reconstruction algorithm, the practical frequency resolution is limited not only by the resolution of the equipment, but more importantly, by the presence of many sources of noise. The artificial addition of more frequency points by interpolating the signal is also not viable because it can add artificial errors from any misrepresentation of the real signal. This effect is observed further on when investigating the reconstruction of blind areas in Fig. 4.1. Furthermore, real-time monitoring applications benefit from faster reconstruction algorithms, which has a direct relation to the number of frequency steps used in the reconstruction. Therefore, the only alternative to improve the reconstruction accuracy is to improve the position evaluation of each frequency step. Only synthetic data are used for this research. It is the only way to know the true density profile, enabling the verification of the accuracy of the reconstruction method applied.

The procedure followed was to assume functions each more complex than the linear to describe the refractive index shape in each integration step, as done in Sec. 3.3. The stability and accuracy obtained when using parabolic and fixed or adaptive fractional power functions are compared to the previous method in Sec. 3.4 and after tested against spurious events and phase noise in Secs. 3.5 and 3.6. The conclusions on these

investigations led to an optimization of the best integration shapes in relation to the plasma parameters, in Sec. 3.8. A procedure that can be performed for any profile shape.

This chapter is concluded with a demonstration in Sec. 3.9 of the achieved improvements when applying the optimized reconstruction scheme in one very demanding case, with the additional constraint of using less probing frequencies.

The first step in the profile reconstruction investigation is to review the current standard method in the following section.

## 3.2 Overview of the reconstruction method of Bottollier-Curtet

Two cut-off branches are available to probe with the X-mode polarization. The left hand polarization in lower frequencies and right hand polarization in higher frequencies. These cut-off frequency profiles are given by [6]:

$$f_{L,R} = \frac{\mp f_{ce} + \sqrt{f_{ce}^2 + 4f_{pe}^2}}{2}, \quad (3.1)$$

with

$$f_{ce} = \frac{eB}{2\pi m_e}, \quad f_{pe} = \frac{1}{2\pi} \sqrt{\frac{n_e e^2}{m_e \epsilon_0}}, \quad (3.2)$$

where  $f_L$  is the left hand polarization cut-off frequency corresponding to the minus sign,  $f_R$  is the right hand polarization cut-off frequency corresponding to the plus sign,  $f_c$  the electron cyclotron frequency,  $f_{pe}$  the plasma frequency,  $e$  the electron charge,  $m_e$  the electron mass,  $B$  the magnetic field,  $n_e$  the electron density, and  $\epsilon_0$  the vacuum permittivity. Furthermore, the dispersion relation reads:

$$N = \sqrt{1 - \frac{X(1-X)}{1-X-Y^2}}, \quad (3.3)$$

with

$$X = \frac{f_{pe}^2}{f^2}, \quad Y = \frac{f_{ce}}{f}, \quad (3.4)$$

where  $N$  is the refractive index and  $f$  the injected frequency.

The reconstruction method of Bottollier-Curtet computes the spatial step from the phase shift associated to the frequency step. To find the phase shift, one compares the measured phase shift (including the total path of the probing waves) to the numerically calculated phase shift under the WKB approximation up to the last known position. A representation of each of these components is found in Fig. 3.1. The numerical phase shift from point  $A$  to  $B$  is computed integrating the profile of refractive index, as in Eq. 3.5, given in Ref. [30].

$$\phi(B) - \phi(A) = \frac{2\pi f}{c} \int_A^B N(f, f_{pe}(x), f_{ce}(x)) dx, \quad (3.5)$$

where  $N$  is the refractive index,  $f$  is the launched wave frequency and  $c$  is the speed of light in vacuum.

In the case of X-mode reflectometry, the integral of the refractive index is too complex to be determined analytically. A method like the well established Abel inversion for the O-mode polarization cannot be developed in this case. The algorithm developed by Bottollier-Curtet assumed a linear refractive index profile between the known positions, and therefore a trapezoidal integration is used at every spatial step. For the trapezoidal integration scheme, the area under the refractive index in the last spatial step can be calculated as the area of a right triangle. The next position,  $x_n$ , in terms of the previous position,  $x_{n-1}$ , and the refractive index  $N_{n-1}$  at position  $x_{n-1}$ , reads, according to Eq. 3.5:

$$\begin{aligned} \Delta\phi_{x_{n-1}}^{x_n} &= W \frac{2\pi f_n}{c} N(f_n, x_{n-1}) \times (x_n - x_{n-1}), \\ \therefore x_n &= x_{n-1} + \frac{c \Delta\phi_{x_{n-1}}^{x_n}}{W 2\pi f_n N(f_n, x_{n-1})}, \end{aligned} \quad (3.6)$$

with a weight factor  $W = 1/2$  for the linear case, and  $\Delta\phi_{x_{n-1}}^{x_n}$  being the total phase shift of a frequency step  $f_{n-1}$  to  $f_n$ . Explicitly from the evaluation of Fig. 3.1,  $\Delta\phi_{x_{n-1}}^{x_n}$  can be written as:

$$\Delta\phi_{x_{n-1}}^{x_n} = \Delta\phi_{f_{n-1}}^{f_n} - [\phi_{x_0}^{x_{n-1}}(f_n) - \phi_{x_0}^{x_{n-1}}(f_{n-1})]. \quad (3.7)$$

with  $\Delta\phi_{f_{n-1}}^{f_n}$  being the experimental measurement and  $[\phi_{x_0}^{x_{n-1}}(f_n) - \phi_{x_0}^{x_{n-1}}(f_{n-1})]$  numerically computed.

Reconstructing the profile with the recursive Eq. 3.6 and the weight factor  $W=1/2$  results in an unstable reconstruction method. A stabilization factor was introduced for the reconstruction to converge. The numerically computed phase shift of each frequency step was averaged with the previous step. Considering approximations in the phase expression, it was later proposed by Bottollier-Curtet [66] that in the vicinity of the reflection point (where the refractive index goes to zero), the integral of the refractive index reduces to using  $W = 2/3$ , instead of the  $1/2$  from the trapezoidal case. The same result was obtained later when the trapezoidal integration was performed over the dielectric permittivity instead of the refractive index, as proposed by Shelukhin [67]. Following these results, the methodology remains to integrate all the previously determined positions with the trapezoidal scheme, and only the last position with the integration weight factor of  $2/3$ . This is valid for every frequency step computed.

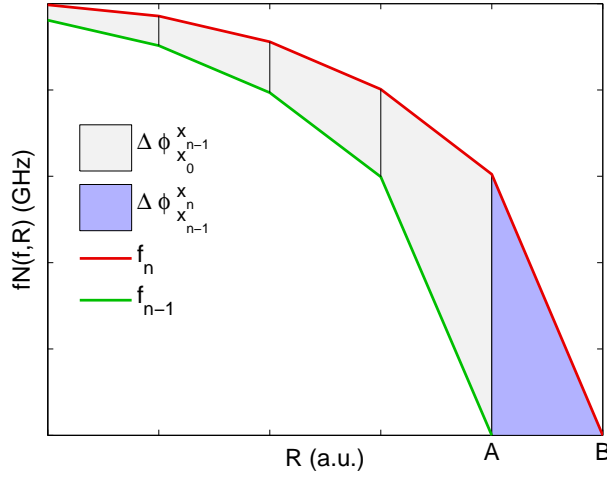


Fig. 3.1 Reconstruction scheme comparing the phase shift to the trapezoidal integration of the injected frequency times the refractive index as in Eq. 3.5, as a function of the plasma radius starting at the edge and going towards the core. Based on Bottollier-Curtet's paper[58].

### 3.3 New approaches on the reconstruction method

When the probing wave is propagating with a frequency well above the local cut-off frequency, the refractive index is almost constant and close to the value of one. In this case, the trapezoidal integration of the refractive index is accurate. On the other hand, near the reflection position, the refractive index changes abruptly to the value of zero, and it is not well described by a linear function. Envisaging a reconstruction more accurate, stable and less sensitive to noise and turbulence, the usage of functions more complex than linear in the last integration step of the refractive index are investigated. The accuracy of the recursive method depends mainly on the integration method at the last radial step for each probing frequency. The integration method used through the previous steps will only contribute to the final error at the same order of magnitude as in the last step if the radial step becomes greater than 5 cm, a condition not explored here. The first step taken to improve the linear shape in the last integration steps was to implement parabolic shapes. Two schemes are proposed to find parabolas that describe the refractive index profile. The parabolas are found from the local plasma properties, meaning that the used parabola is different for every frequency step. Then a square root profile is assumed for all frequency steps, since it has the same behaviour of the refractive index, of high gradient close to zero. Lastly, functions of the type  $x^\alpha$ , with  $\alpha$  between zero and one, depending on the local plasma parameters. The following three sections (3.3.1, 3.3.2 and 3.3.3) describe how to implement these integration shapes, followed by a comparison of the accuracy obtained with them on different profile shapes. The reconstruction stability and the noise impact are discussed afterwards, and lastly, a section is devoted on the relationship between the exponent in  $x^\alpha$  shapes, to the local plasma properties and the additional advantages from implementing this method.

#### 3.3.1 Parabolic integration shapes

In order to determine a parabolic profile for each integration step, three parameters are necessary to describe a parabola. Furthermore, the position of the cut-off is not yet known, and in fact, it is the parameter to be computed. Thus, in total, four boundary conditions must be assumed. They are: 1) the area under the last integration step, which is related to the phase shift measurement; 2) the refractive index is zero at the reflection position; 3) one point (index, position) before the reflection position; and 4) the point (index, position) two steps before the reflection position. An additional boundary condition can be the continuity of the refractive index slope at the position prior to the reflection point. This condition was also assumed in the development process, leading to

an additional parabolic method where this condition replaced the condition 4. However, the obtained accuracy was equivalent and the method was more sensitive to noise and density fluctuations. This comparison was discussed in Ref. [62].

The four boundary conditions are written in full in Eqs. 3.8 to 3.11. For simplicity, the positions are written as  $x$ , with  $x_n$  being the reflection point,  $\Delta x = x_n - x_{n-1}$ , and the ordinate values of  $f_n N(f, R)/c$  are written as  $y_n$ .

$$\Delta\phi_{x_{n-1}}^{x_n} = a \frac{(\Delta x)^3}{3} + b \frac{(\Delta x)^2}{2} + c\Delta x, \quad (3.8)$$

$$0 = ax_n^2 + bx_n + c, \quad (3.9)$$

$$y_{n-1} = ax_{n-1}^2 + bx_{n-1} + c, \quad (3.10)$$

$$y_{n-2} = ax_{n-2}^2 + bx_{n-2} + c. \quad (3.11)$$

The parameter  $c$  can be isolated in Eq. 3.9 and inserted in Eqs. 3.10 and 3.11. Then,  $b$  can be isolated in Eq. 3.11 and inserted in Eq. 3.10 to have an expression depending only on  $a$ . Solving this way for  $a$ ,  $b$  and  $c$  leads to the solutions in Eq. 3.12.

$$\begin{aligned} a &= \frac{y_{n-1} - y_{n-2}(x_{n-1} - x_n)/(x_{n-2} - x_n)}{x_{n-1}^2 - x_n^2 - (x_{n-2}^2 - x_n^2)(x_{n-1} - x_n)/(x_{n-2} - x_n)}, \\ b &= \frac{y_{n-2} - a(x_{n-2}^2 - x_n^2)}{x_{n-2} - x_n}, \\ c &= -ax_n^2 - bx_n. \end{aligned} \quad (3.12)$$

Adding the phase-shift from Eq. 3.8 leads to:

$$a \frac{(\Delta x)^3}{3} + b \frac{(\Delta x)^2}{2} + c\Delta x - \Delta\phi_{x_{n-1}}^{x_n} = 0, \quad (3.13)$$

with the parabola parameters  $a$ ,  $b$  and  $c$  given by Eq. 3.12. This way, numerically finding the appropriate root of this complicated equation solves for  $x_n$ . Readily available tools can be implemented for this task, such as the Matlab functions *fzero* and *fsolve*.

In order to solve for all  $x_n$ , two previous positions were assumed known. Therefore, the implementations described here started with the standard linear Bottollier-Curtet method for the first steps. The first position is also not suitable for the parabolic method. The flat derivative at the vacuum boundary enforced a strong condition for the parabola that is hard to satisfy, making the method diverge in some occasions. This way, the parabolic method is implemented starting at the fourth frequency step.

Additional constraints are also necessary to make the method stable when there are spikes in the phase shift measurement. The method is restrained to only return positions between the previous position and the linear solution (i.e. the parameter  $a$  cannot be positive). If this condition is broken in any reconstruction step, the linear solution is implemented only for that step.

### 3.3.2 Square root integration shapes

By observing an example of index profile, it can be noted that the slope of the index profile tends to be steeper near the reflection position, resembling a square root function. Due to this fact, a square root profile is also taken into account in this section.

If a square root function is integrated, and the result is compared in terms of a multiplication of horizontal and vertical displacements,  $dx$  and  $dy$ , one finds that the area of a square root is equal to  $(2/3)dxdy$ . Therefore, assuming a square root index shape in the last integration step is equivalent to using the weight factor  $W$  equals to  $2/3$ , which turned out to be equivalent to the other assumptions already mentioned [66, 67]. The index shape in this method is therefore constant across all frequency steps.

### 3.3.3 $x^\alpha$ integration shapes

In the conditions of high density, density gradient and a small radial step, the square root function fits almost perfectly the refractive index. If these conditions are not well satisfied, which is typical of plasma edge conditions, the index shape changes away from a square root function towards a step function, as depicted in Fig. 3.2. In order to adapt the integration shapes to these changes, this section proposes the implementation of functions of the type  $x^\alpha$ , with  $\alpha$  as a function of the plasma radius. In the same manner that the integration of the square root function was shown to result in  $W = 2/3$ , functions of the type  $x^\alpha$  can be demonstrated to lead to a generic form of  $W = 1/(\alpha + 1)$ . Therefore, the factor  $W$  varies between one when  $\alpha = 0$  and  $2/3$  when  $\alpha = 1/2$ .

The accuracy of all methods listed so far are compared in the next section (Sec. 3.4) for the cases of a linear profile in  $f_R$  and a typical scenario in Tore Supra. In this section, instead of pursuing how to find the profile of the best  $x^\alpha$  shapes, it is demonstrated the  $W$  profile for the typical Tore Supra case of the next section. This way, the obtained accuracy and stability of the method can be compared with the other methods presented, and in Secs. 3.7 and 3.8, the possible procedures to find the  $W$  profile is elaborated.

The Tore Supra test case of the next section (Sec. 3.4) has a low edge density and density gradient and a pedestal at the position of 12 cm. The frequency profiles for

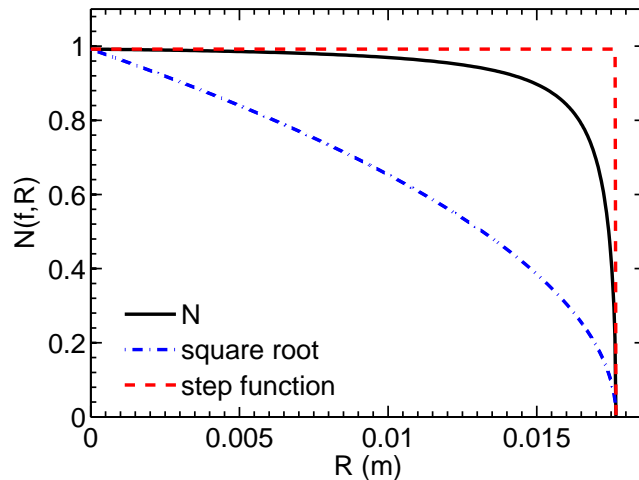


Fig. 3.2 The shape of the refractive index  $N$  in typical edge conditions is compared to a square root and a step function. Probed in the right hand polarization with a frequency slightly above the initialization at  $f = f_c$ . The position  $R=0$  marks the initialization on the plasma edge and increases towards the plasma core.

this example are shown in Fig. 3.3, assuming the low background magnetic field of 2 T in the plasma center. For this case, the  $x^\alpha$  shapes, and therefore the  $W$  profile, are computed following the WKB approximation and depicted in Fig. 3.4. Although these figures describe the behaviour from the right hand polarization, the left hand polarization has almost identical results. However, due to technological constraints, the left hand polarization cannot be probed on very low densities, because  $f_L$  goes to zero. Therefore, the initial positions where the factor  $W$  is farther from  $2/3$  are not expected to be probed and the correction in  $W$  is less crucial.

### 3.4 Comparison of accuracy from all methods

In order to analyse the performance of each method, density and magnetic field profiles are assumed and the reconstruction is simulated. The plasma size, the maximum density and the magnetic field profile correspond to typical Tore Supra discharges. Also following the present data-acquisition characteristic, 500 probing frequencies are considered. To analyse the obtained accuracy of each method, the figures show the profile of discrepancy from the positions calculated to the correct cut-off positions for all probing frequencies. Since the magnetic field is assumed well known, the errors in density come from these errors in the calculation of the cut-off positions.

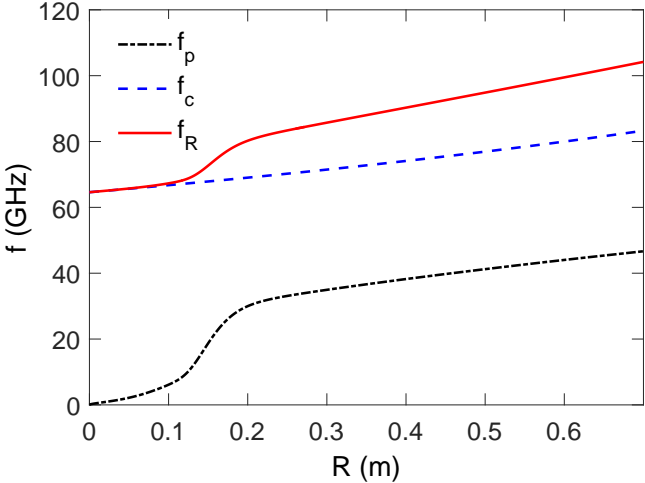


Fig. 3.3 Frequency profiles according to Eqs. 3.1 and 3.2 from a typical Tore Supra discharge including a pedestal located at R=12 cm and B=2 T at the plasma center.

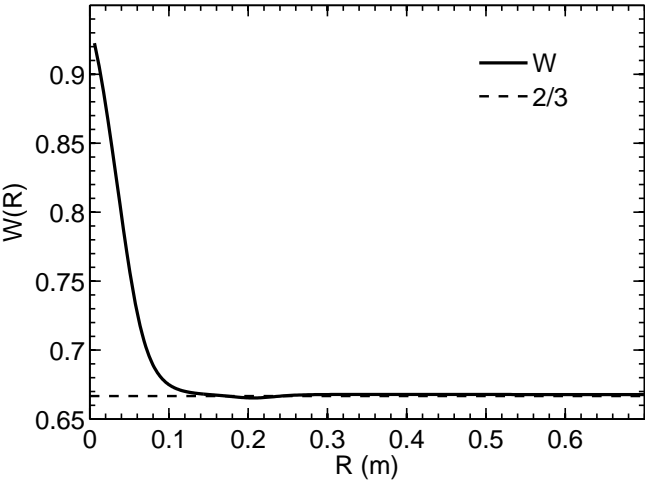


Fig. 3.4 Profile of weight factor W, as defined in Eq. 3.6, for the typical Tore Supra profile example as depicted in Fig. 3.3.

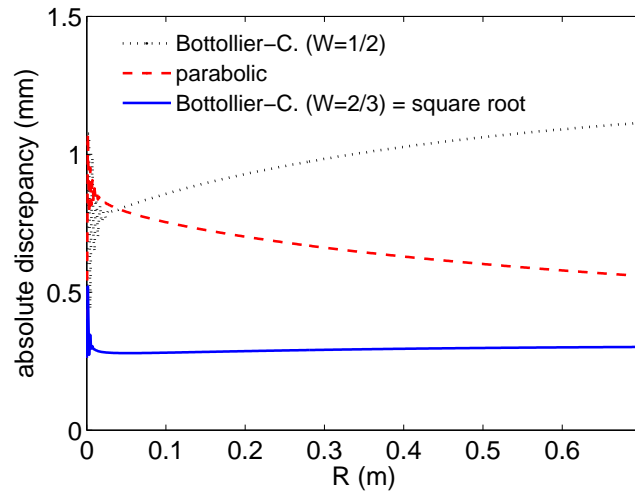


Fig. 3.5 Profiles of absolute radial discrepancy when reconstructing the density profile with the conditions of linear  $f_R$  profile, 500 probing frequencies and a precision of 0.1 mm in the initialization.

Initially, the simplest density profile shape is assumed: a density profile that results in a linear  $f_R$  profile. This way, the basic characteristics of each method are visible without additional features from the profile shape.

The comparison between the obtained discrepancy profile for the methods of Bottollier-Curtet linear, parabolic and the square root are presented in Fig. 3.5. The linear Bottollier-Curtet solution and the parabolic methods start with the same accuracy of 1 mm in the first reconstruction positions, which is expected since the parabolic method is implemented starting at the fourth position. When going to the core positions, the parabolic method becomes more accurate while the linear Bottollier-Curtet method becomes less accurate. The parabolic method showed an improvement compared to the linear Bottollier-Curtet method in the core region without needing the stabilization averaging trick introduced in the linear method. When the weight factor  $W$  is taken as  $2/3$ , e.g. when the integrating shape is assumed to be a square root, the error in the edge region is just above half millimeter and quickly converges close to 0.3 mm across the entire profile.

Having in mind these main characteristics, the reconstruction of a more complex density profile shape can be simulated to emphasize some features and demonstrate other features. The next example is a density profile shape routinely observed in Tore Supra and other latest generation tokamaks. It consists of a low density and density gradient in the edge region, followed by a pedestal with high density gradient and back to low

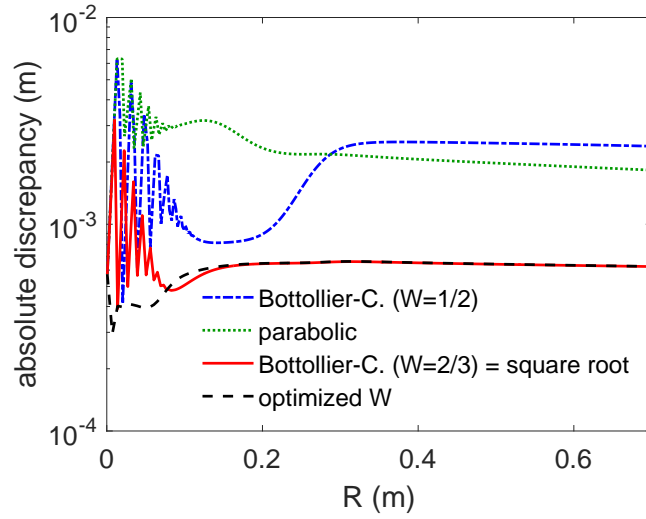


Fig. 3.6 Profiles of absolute radial discrepancy when reconstructing the density profile with the conditions of 500 probing frequencies, a precision of 0.1 mm in the initialization and the Tore Supra example profiles as depicted in Fig. 3.3.

density gradient around the plasma center. In this case, the method with the integration shapes  $x^\alpha$  optimized for this profile shape is also included in the comparison, which can be found in Fig. 3.6.

In Fig. 3.6, the parabolic method doesn't show an improvement from the linear Bottollier-Curtet method. Reinforcing the feature observed before, the parabolic shape is specially inaccurate to describe the refractive index shape at edge conditions.

The method with the square root index shape shows more features in this case. First, the edge region, where the plasma has a low density and density gradient, is less accurate, with oscillations peaking up to 3.2 mm. Then, the valley around 12 cm marks the pedestal, where the density gradient is at maximum. When the density gradient increases, the radial step decreases for a fixed frequency step, resulting in a more accurate determination of the probing positions. In addition, the refractive index profile is better described by a square root shape at the core region, due to higher density and density gradient, and when smaller radial steps occur, i.e. the approximation used in Bottollier-Curtet PhD thesis [66].

If the refractive index shape is adapted for the edge region with the shape  $x^\alpha$  as introduced in Sec. 3.3.3, the edge inaccuracy and oscillations from the square root method disappear. This method achieved a precision level around 0.6 mm through the entire profile. In practice, the reconstruction accuracy in this case will be determined by the noise and turbulence levels and the precision in the initialization. The method to

estimate this implemented profile of the integration weight factors  $W$  is elaborated in Sec. 3.8.

### 3.5 Stability of the inversion method

The linear Bottollier-Curtet's algorithm (when  $W=1/2$ ) turned out to be unstable and a stabilization mechanism was introduced. The measured phase shift of each frequency step is averaged with the value of the previous step. In order to analyse the stabilization mechanisms, the expression used to calculate each new position from Eq. 3.7 is rewritten in Eq. 3.14, for a simpler referencing.

$$x_n = x_{n-1} + \frac{1}{W} \frac{\Delta\phi}{N}, \quad (3.14)$$

with  $\Delta\phi$  as given in eq. 3.7 and  $N$  being  $N(f_n, x_{n-1})$ .

First, the averaging with the previous step, as in the linear Bottollier-Curtet solution, was tested for every component of Eq. 3.14 (the radial step, the phase shift and the value of  $N$ ). The conclusion is that there is no preferred component to be averaged. The best component to average varies depending on the profile to be reconstructed. Next, the numerical stability is investigated with a fixed local integration factor  $W$  which is always the case apart from the parabolic method, where a new parabola is computed in each step.

To investigate the role of each element of Eq. 3.14 in the stability of the reconstruction method, the evolution of the error in each of these elements was observed along a reconstruction. This is possible since the correct positions and profiles are known. First, it was noted that the error in the evaluation of  $N(x_{n-1})$  and  $\Delta\phi_{x_{n-1}}^{x_n}$  comes from an error in the determination of  $x_{n-1}$ . Meaning that an error in the position  $x_n$  is due to not using the ideal value for  $W$ , plus the error propagated from the previous position into  $\Delta\phi$  and  $N$ . The propagation of these three error sources can be evaluated by equating them as in Eqs. 3.15 to 3.17, for an error in  $\phi$ ,  $W$  and  $N$ , respectively, where the elements on top are summed with an error and the bottom elements have a multiplicative factor as a percentage error.

$$\frac{1}{W} \frac{(\Delta\phi + \Delta\phi')}{N} = \frac{1}{W} \frac{\Delta\phi}{N} + \frac{1}{W} \frac{\Delta\phi'}{N}, \quad (3.15)$$

$$\frac{1}{\delta W} \frac{\Delta\phi}{N} = \frac{1}{W} \frac{\Delta\phi}{N} + \left(\frac{1-\delta}{\delta}\right) \frac{1}{W} \frac{\Delta\phi}{N}, \quad (3.16)$$

$$\frac{1}{W \epsilon N} \frac{\Delta\phi}{N} = \frac{1}{W} \frac{\Delta\phi}{N} + \frac{1}{W} \left(\frac{1-\epsilon}{\epsilon}\right) \frac{\Delta\phi}{N}. \quad (3.17)$$

Equating these error sources show how each element influence the error propagation. All steps are subject to the error of not using the ideal local value of  $W$ , plus the error propagating. The errors in the evaluation of the phase shift will be multiplied by the factor  $1/WN$ , whereas the errors in the refractive index and weight factor are multiplied by  $\Delta\phi/WN$ . Furthermore, any error in each element of Eq. 3.14 induces an oscillation. For example, an excess in  $x_n$  causes an excess in the computed  $\Delta\phi_0^n$  for the frequency  $f_{n+1}$ , which causes an under evaluation of  $\Delta\phi_n^{n+1}$ , resulting in under evaluating  $x_{n+1}$ . These errors are damped or not depending on the error multiplicative factors written in Eqs. 3.15 to 3.17.

The combination of these facts shows that the more efficient scenario to damp errors is when  $WN$  is greater because the error is multiplied by  $1/WN$  in the next step. Furthermore, the reconstruction damps the previous errors when  $1/W$  is between one and two (the step function and linear cases). For  $1/W$  equals or greater than two there is no damping of errors. Since there is no error damping and an additional error is introduced in every step by not using the perfect value of  $W$ , the system becomes unstable. This interpretation explains why it is observed that the square root integration shape converges, unlike the linear integration, and when the factor  $W$  and  $N$  are closer to one, any error introduced is damped more efficiently. This last feature is observed in the edge conditions in the next section. A last remark is that this error damping analysis is based on the true local values of  $W$ . For example, if using  $W = 1$  when it is not the ideal value (expecting to have an improved error damping), results in the damping properties not being of  $W = 1$ , but of the ideal local value, and in addition an error is introduced from the excess in  $W$ , as it was shown in Eq. 3.16.

## 3.6 Noise analysis

This section demonstrates how different sources of noise impacts the reconstruction accuracy. First, a spike of 1% is added in the phase shift of a single frequency, and latter,

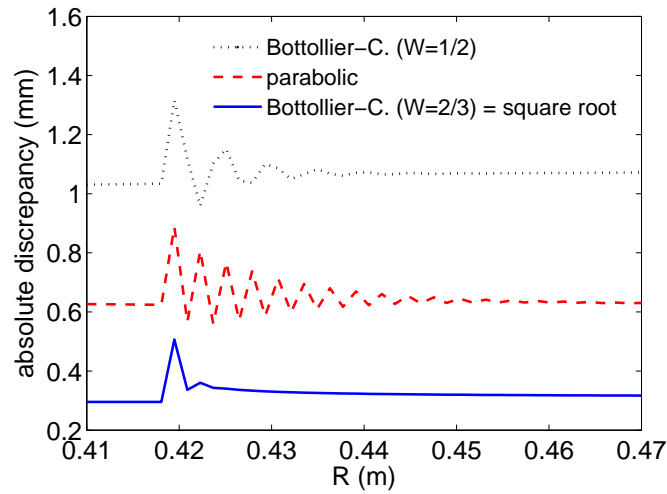


Fig. 3.7 Radial discrepancy when reconstructing the density profile with a 1% spike in the phase shift of a single frequency and conditions of 500 probing frequencies, a precision of 0.1 mm in the initialization and the linear  $f_R$  profile.

varying levels of white noise are added to the phase shift. The radial error at the location where the phase shift spike was introduced is presented in Fig. 3.7.

Fig. 3.7 shows that an error introduced is damped faster for the square root method. The parabolic method enforced boundary conditions to find the parabolas and this made the error propagate longer. The fluctuations stay even longer if the parabolas are computed using the boundary condition of constant derivative at the previous point. A spike in the probing frequency and a density perturbation were also tested, but the comparison between the different methods had the same features as presented in the phase shift case in Fig. 3.7.

Next, white noise is added to the phase shift data, as a percentage of the average value, to simulate the experimental noise in the Tore Supra example. Fig. 3.8 shows the obtained accuracies for the method with optimized  $W$  at different levels of noise. From the interpretation on the results of the last section (Sec. 3.5), one can observe how the edge region is very efficient in damping the noise introduced since  $1/WN$  is minimized and the factor  $W$  is optimized. This is an interesting feature of this method since the edge region is typically more prone to noise and fluctuations in tokamaks.

The core region, on the other hand, saturates at a higher value for higher noise levels. The linear Bottollier-Curtet and the square root method showed the exact same behaviour, having the same discrepancies in the edge region for all noise levels and increasing in the core always keeping the same difference between them. The parabolic

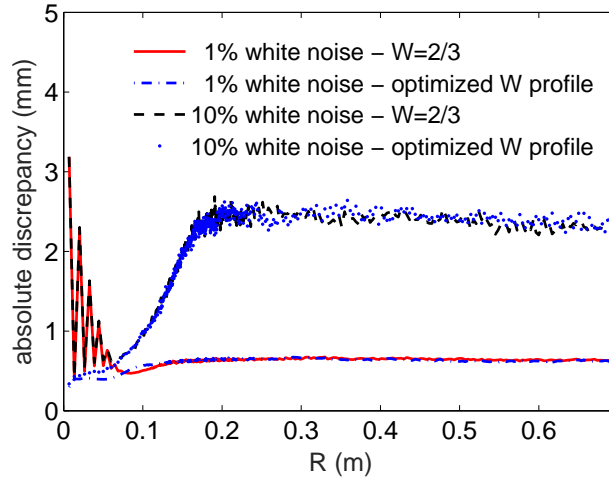


Fig. 3.8 Radial discrepancy when reconstructing the density profile with different levels of white noise in the phase shift data and conditions of 500 probing frequencies, a precision of 0.1 mm in the initialization and the typical low B Tore Supra example profile. Each discrepancy profile is the average of 500 reconstructions.

method is not represented because it was able to find the parabolas only with a maximum noise level up to 1%. Beyond this level of noise, the method is unable to associate parabolas for the data in too many cases and the method collapses to the linear solution.

In a different perspective, the white noise was introduced in the time-of-flight data, followed by smoothing and extraction of the phase. This data treatment process introduced an additional accuracy shift of 1 mm in the core region even when no noise was introduced. This feature depends on the technique implemented and the shape of the signal. A complete investigation of all treatment techniques with different signal shapes is beyond the scope of this paper. On the bright side, this methodology did not increase the saturation accuracy in the core as the noise level is increased. The increase of the white noise introduced can be translated into fluctuations around the noiseless solution, which can be associated to bigger error bars. For a 20% noise level, these error bars are close to 0.5 mm in the edge region and 1 mm in the core region.

After covering the obtained accuracy and robustness of the reconstructions with optimized  $W(R)$ , the next two sections (Secs. 3.7 and 3.8) start the discussion of how the profile of  $W$  can be obtained.

### 3.7 Approaching the optimal $W(R)$ profile from iterative reconstructions

One possible way to optimize the  $W(R)$  profile is to use an iterative method. After reconstructing a profile, a better integration factor  $W$  can be manually computed from the refractive index shape for each frequency step. These optimized factors can be used to reconstruct the profile in the next frequency sweep. The iterations can continue over and over. Certainly this iterative approach is only valid for fast sweeping rates, since the profile cannot change abruptly and significantly from one sweep to the next.

Without any additional input and assuming the typical Tore Supra profile as introduced in Fig. 3.3, the optimization saturated after five iterations, achieving the same accuracies demonstrated in the optimized  $W(R)$  case of Fig. 3.6.

Another way to speed up the optimization is to assume a pre-determined shape for  $W(R)$  at the first reconstruction, based on the observed  $W(R)$  profile observed at Fig. 3.4 for the expected profile shape. The  $W(R)$  of Fig. 3.4 can be well described starting at one in the first frequency, decreasing linearly until reaching the value of  $2/3$  at the pedestal position. The pedestal position is well known in typical Tore Supra conditions and does not vary much from shot to shot. In any case, the sensitivity of the iterations to the pedestal position can be tested. For such test, a case with an under evaluated pedestal is assumed. This case is depicted in Fig. 3.9 with the estimated pedestal position set at 0.13 m. All test cases in this section have the test profile just as the standard Tore Supra case depicted in Fig. 3.3, but with the pedestal moved to 0.175 m to allow for more testing range around the pedestal.

Even on the first reconstruction with the fitted  $W(R)$ , the obtained accuracy is already improved compared to the fixed value of  $2/3$ . The obtained accuracy lies between the square root and the optimized  $W(R)$  accuracies as seen in Fig. 3.6. Even with the pedestal under estimated in Fig. 3.9, the first iteration is already saturated and further iteration does not change the obtained profile for  $W(R)$ .

For comparison, an over evaluation case is depicted in Fig. 3.10, with the pedestal estimation set at 0.22 m.

The case with the over evaluated pedestal in Fig. 3.10 also converges after only one iteration. The reconstruction with the initially estimated  $W(R)$  is also achieving an accuracy in between the square root and the optimized  $W(R)$  reconstructions as seen in Fig. 3.6. In this case, it is slightly more accurate (closer to the optimized  $W(R)$  accuracy), but at a such low amount that would not matter in an experimental set up due to the experimental noise level.

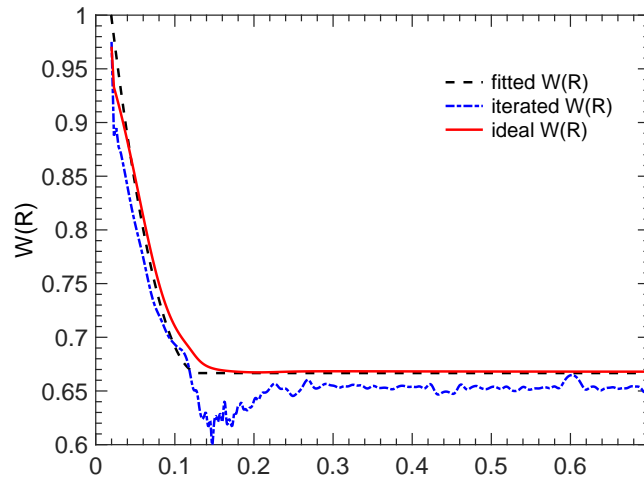


Fig. 3.9 Ideal and estimated integration factors  $W(R)$ . The fitted case assumed one at the first probing frequency and goes linearly to  $2/3$  at the pedestal position assumed at 0.13 m. The iteration process already converges after the first iteration, not changing significantly with further iterations. The input frequency profiles are the same as in Fig. 3.3 but with the pedestal moved to 0.175 m

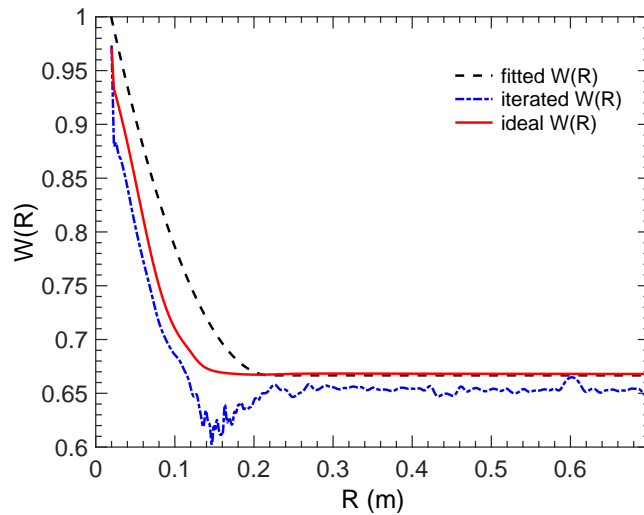


Fig. 3.10 Ideal and estimated integration factors  $W(R)$ . The fitted case assumed one at the first probing frequency and goes linearly to  $2/3$  at the pedestal position assumed at 0.22 m. The iteration process already converges after the first iteration, not changing significantly with further iterations. The input frequency profiles are the same as in Fig. 3.3 but with the pedestal moved to 0.175 m.

In both iterative processes in Figs. 3.9 and 3.10, the main change in the  $W(R)$  profile is in the outmost edge region. Near the pedestal the iterative optimization is not improving from the constant  $W = 2/3$ . Thus, another option for the iteration is to iterate only the first frequency step and refit towards the pedestal. This way the iteration is even easier to perform. Fig. 3.11 shows a case with the pedestal position well estimated initially, and one case with only the first position is iterated. The estimation of the  $W(R)$  profile is even closer to the ideal value in the case with only the first frequency step iterated and the rest fitted towards the pedestal. The obtained accuracy for this case is equivalent to the optimized  $W(R)$  profile as shown in Fig. 3.6.

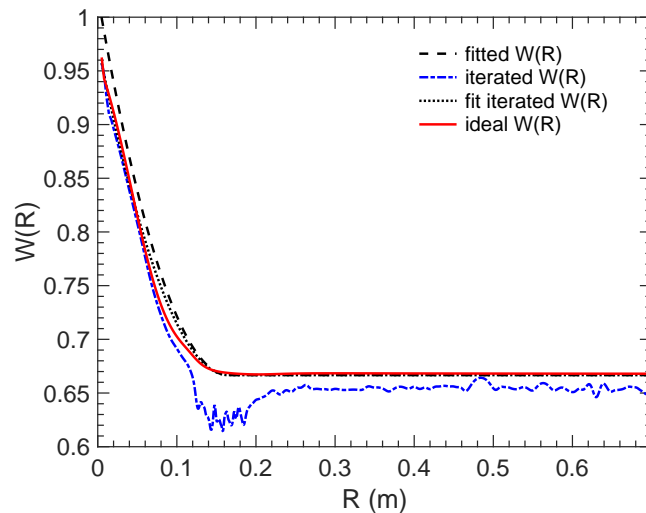


Fig. 3.11 Ideal and estimated integration factors  $W(R)$ . The fitted case assumed one at the first probing frequency and goes linearly to  $2/3$  at the pedestal position assumed at 0.175 m. The iteration process already converges after the first iteration, not changing significantly with further iterations. This case also includes an iteration performed only on the first frequency step, with the remaining factors again fitted towards  $2/3$  at the pedestal position. The input frequency profiles are the same as in Fig. 3.3 but with the pedestal moved to 0.175 m..

The profile reconstruction with the fitted  $W(R)$  profile already offers increased accuracy compared to the fixed  $W = 2/3$ . The iteration improves even further the obtained accuracy, reaching the fully optimized accuracy as displayed in Fig. 3.6, labeled optimized  $W(R)$ . This solution is easily implemented in such cases, where the pedestal is evident and its position well known.

In cases where there is no pedestal, the pedestal is not well defined, or its position is not well known, another solution need to be developed. In the next section (Sec. 3.8), a

solution is developed to estimate the optimal  $W$  at each frequency step based on the local plasma parameters.

### 3.8 Obtaining the ideal refractive index shape from the plasma properties

The analyses in Secs. 3.4-3.6 demonstrate the accuracy and stability improvements when optimizing  $W$  everywhere. In this section, the procedure to find the profile of the optimized  $W$  is elaborated.

From the simplified Tore Supra example used in Secs. 3.4-3.6, the profile of  $W$  was given in Fig. 3.4. In this case, one can implement a linear fit in  $W$ , from the edge value to  $2/3$  in the pedestal position. The precision of the pedestal position was tested to not be crucial for the obtained accuracy. The bottlenecks of this implementation are the edge  $W$  value and the validity of the assumed shape, i.e. a well defined transition from low density and gradient to high gradient. The initial  $W$  value can start at one and be improved either iteratively or by the expression in Eq. 3.28 developed below. Nevertheless, an initial reconstruction is necessary to estimate an initial profile of  $\nabla f_R$  for computing the expression in Eq. 3.28 and this method provides a good initial reconstruction of the density profile.

The next step is to determine the profile of refractive index shape, which gives  $W$ , based on the local plasma properties. The first and most natural step is to observe what is the best function of the type  $x^\alpha$  to fit the index profile at different probing positions depending on the integration length. For the example Tore Supra profile these relations are presented in Fig. 3.12.

At all plasma positions the value of  $\alpha$  converges to  $1/2$  for  $dR$  going to zero. As the reconstruction step  $dR$  increases,  $\alpha$  goes to zero depending on the local plasma parameters. The first approach would be to fit the evolution of  $\alpha$  versus  $dR$ , and relate the fitting parameters to the local plasma properties, but two major difficulties arise when doing so. First, the step length is not yet known in a reconstruction step, it is in fact the quantity to be calculated. Second, the fitting parameters do not have a straight forward relation to fit against the plasma properties. To solve these problems, the relations of  $\alpha$  can be expressed in terms of a known quantity, e.g. the step in the probing frequency or the refractive index value at the previous position  $x_{n-1}$ , i.e.  $N_{n-1}$ . The refractive index was chosen over the frequency step because the relations are simpler to fit. Since the refractive index is zero at the reflection position and goes towards one as the reconstruction step increases, the parameter  $\alpha$  can be adjusted taking this range into

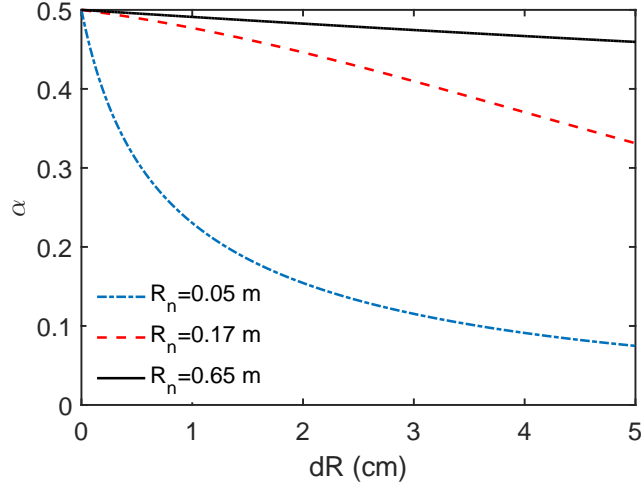


Fig. 3.12 Optimized index shape function  $x^\alpha$  by the radial integration length at three different radial positions.

account, as in the proposed shape function in Eq. 3.18. The second issue is suppressed if a term is added to account for the evolution of  $\alpha$  with the variation of  $N_{n-1}$ . From these features a shape function can be proposed as:

$$x^\alpha = x^{0.5-0.5\beta(N_{n-1})}. \quad (3.18)$$

In order to solve for  $\beta$ , it is assumed that the plasma parameters that dictate the refractive index shape are the local cut-off frequency  $f_R$  (i.e. the probing frequency) and the gradient of the frequency cut-off profile,  $\nabla f_R$ .

In Fig. 3.13 it is shown two example relations for two different probing positions in the same example Tore Supra conditions for a 5 cm radial step. When probing the plasma core, since the density in the previous probing position is not close to vacuum, the refractive index  $N_{n-1}$  is small, which makes the relation  $\beta(N_{n-1})$  well described by a linear function of  $N_{n-1}^2$ . This is seen in Fig. 3.13 for the position of 0.65 m. On the other hand, when probing in the edge plasma with low density as also exemplified in Fig. 3.13, the refractive index is close to one and the  $\beta(N_{n-1})$  behaviour in this region needs a correction from the linear solution. In addition, the same pair  $(f_R, \nabla f_R)$  from the position 0.65 m in Fig. 3.13 could appear in the edge region in different conditions. To ensure that the entire range of refractive index is taken into account, so that the solution obtained is valid for any general condition, the fittings were separated into two parts. First, the linear regime is fitted with  $N_{n-1}$  from zero to 0.25, and after, the correction

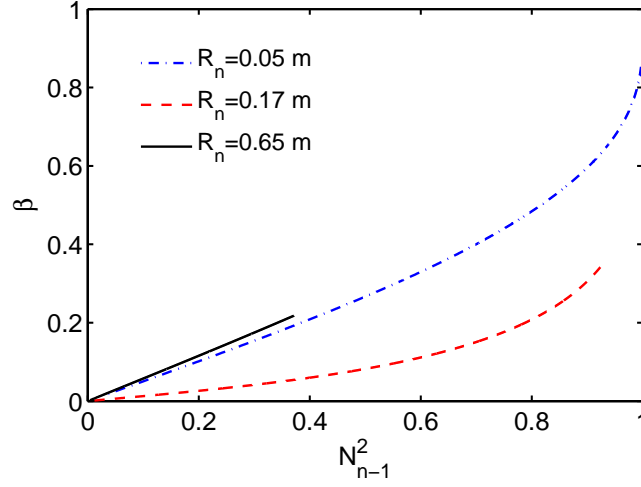


Fig. 3.13 The  $\beta$  parameter from the refractive index fitting shape given in Eq. 3.18, as a function of  $N_{n-1}^2$ , taken at three example radial positions for the example of typical Tore Supra profiles as given in Fig. 3.3.

on the linear solution. The distinction is necessary here because the boundary conditions of each regime are different and explained as follow.

To map the  $\beta$  relations against all possible values for  $f_R$  and  $\nabla f_R$ , new density and magnetic field profiles are assumed for each value of  $(f_R, \nabla f_R)$ . The dependency on  $\nabla^2 f_R$  is neglected here and therefore the assumed profiles are enforced a constant  $\nabla f_R$  everywhere. The  $\nabla f_R$  is a combination of  $\nabla f_{pe}$  and  $\nabla f_{ce}$ , but  $\nabla f_{ce}$  has a positive curvature fixed by the background magnetic field. Which results in a negative  $\nabla f_{pe}$  for a constant  $\nabla f_R$ . If  $\nabla f_R$  is too low, enforcing a constant  $\nabla f_R$  profile results in negative values for the electron density, which is unphysical. When solving the linear regime, the initial density can be increased as necessary and the density profile can have a negative gradient while having positive density and constant  $\nabla f_R$ . The minimum value of  $\nabla f_R$  achieved when fitting the linear regime was 8 GHz/m. In any case, if  $\nabla f_R$  goes to zero, the WKB solution of a sharp reflection also breaks down and full wave effects would have to be considered. The upper limit solved was 200 GHz/m, but it is not as important since at very high gradient the step size is negligible,  $N_{n-1}$  goes to zero and the square root solution is very precise. The solved probing frequency range is from 35 GHz to 250 GHz, because below this value the fitting shapes assumed start to be less adequate, and above is limited by the combination of the gradients assumed.

After the linear regime is solved, the correction part is fitted using a different sweeping tactic. The initial density cannot be increased to compensate for the negative density

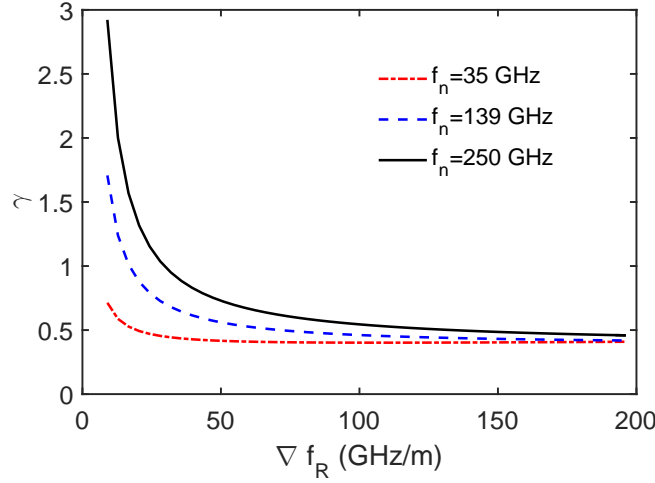


Fig. 3.14 The  $\gamma$  parameter from index fitting shape as given by eq. 3.19 versus the cut-off profile gradient.

profile curvature. All density profiles assumed start with vacuum in the edge to ensure the range of  $N_{n-1}$  until the value of one. The minimum  $\nabla f_R$  solved in this case was frequency dependent, and goes linearly from 12 GHz/m when probing at 35 GHz, up to 40 GHz/m when probing at 120 GHz. Even though the ranges are shorter for the correction part, it is still a broad range because the correction is only relevant near the initialization frequencies when  $N_{n-1}$  is much closer to one. The corrections were fitted assuming the shape  $ax^b$ . The value of  $b$  doesn't vary much and therefore it was fixed at 3.44, or 4.44 if related to  $N_{n-1}$  not squared. Therefore, the relations of  $\beta(N_{n-1})$  can now be written in full as:

$$x^\alpha = x^{0.5-0.5\beta(N_{n-1})} = x^{0.5-0.5(\gamma N_{n-1}^2 + \delta N_{n-1}^{4.44})}. \quad (3.19)$$

These relations of  $\gamma$  and  $\delta$  can be found in Figs. 3.14 and 3.15, respectively. The linear relations are fitted with functions of the following expression:

$$\gamma(f_R, \nabla f_R) = p_1(f_R)/(\nabla f_R - p_2(f_R)) + p_3(f_R), \quad (3.20)$$

and the correction part with the same shape, but with parameters named with  $q$ , as:

$$\delta(f_R, \nabla f_R) = q_1(f_R)/(\nabla f_R - q_2(f_R)) + q_3(f_R). \quad (3.21)$$

Using this function shape, all fitted relations have an accuracy around 1% for all probing frequencies. The last step is to know the parameters  $p_n$  and  $q_n$  as a function of

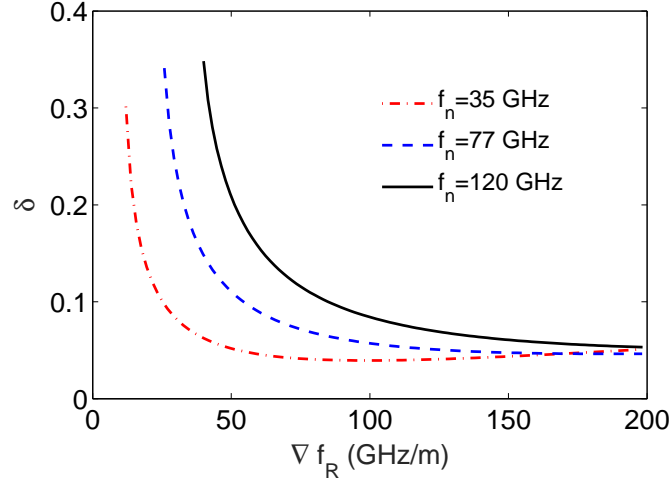


Fig. 3.15 The  $\delta$  parameter from index fitting shape as given by Eq. 3.19 versus the cut-off profile gradient.

$f_R$ . They are smooth well-behaved functions of  $f_R$ , well fitted by high order polynomials as given in Eqs. 3.22 to 3.27.

$$p_1 = a_1 f_R^2 + b_1 f_R + c_1, \quad (3.22)$$

$$p_2 = a_2 f_R^6 + b_2 f_R^5 + c_2 f_R^4 + d_2 f_R^3 + e_2 f_R^2 + f_2 f_R + g_2, \quad (3.23)$$

$$p_3 = a_3 f_R^4 + b_3 f_R^3 + c_3 f_R^2 + d_3 f_R + e_3, \quad (3.24)$$

$$q_1 = a'_1 f_R^3 + b'_1 f_R^2 + c'_1 f_R + d'_1, \quad (3.25)$$

$$q_2 = a'_2 f_R^2 + b'_2 f_R + c'_2, \quad (3.26)$$

$$q_3 = a'_3 f_R^5 + b'_3 f_R^4 + c'_3 f_R^3 + d'_3 f_R^2 + e'_3 f_R + f'_3, \quad (3.27)$$

All parameters  $a_i$  to  $g_i$  are given in table 3.1, while the parameters  $a'_i$  to  $f'_i$  are given in table 3.2. The quality of the fit is expressed as the RMS value of the residuals, computed as a percentage to the average value of that parameter.

Lastly, the optimized integration weight factors  $W$  can be written, in full, as:

$$W(N_{n-1}, f_R, \nabla f_R) = \frac{1}{\alpha(N_{n-1}, f_R, \nabla f_R) + 1}, \quad (3.28)$$

with  $\alpha(N_{n-1}, f_R, \nabla f_R)$  given by Eq. 3.19, and  $\gamma$  and  $\delta$  given by Eqs. 3.20 and 3.27 and tables 3.1 and 3.2, respectively.

Table 3.1 Fitted  $p_1$ ,  $p_2$  and  $p_3$  parameters with  $f_R$  in GHz.

$p_1$	$p_2$	$p_3$
RMS = 0.3%	RMS = 0.5%	RMS = 0.04%
$a_1 = -3.251 \times 10^{-5}$	$a_2 = 6.423 \times 10^{-13}$	$a_3 = 3.098 \times 10^{-11}$
$b_1 = 0.08323$	$b_2 = -6.247 \times 10^{10}$	$b_3 = -2.148 \times 10^{-8}$
$c_1 = -1.136$	$c_2 = 2.476 \times 10^{-7}$	$c_3 = 5.937 \times 10^{-6}$
	$d_2 = -5.136 \times 10^{-5}$	$d_3 = -7.614 \times 10^{-4}$
	$e_2 = 5.940 \times 10^{-3}$	$e_3 = 0.3843$
	$f_2 = -0.3676$	
	$g_2 = 11.43$	

Table 3.2 Fitted  $q_1$ ,  $q_2$  and  $q_3$  parameters with  $f_R$  in GHz.

$q_1$	$q_2$	$q_3$
RMS = 0.02%	RMS = 0.1%	RMS = 0.04%
$a'_1 = 2.237 \times 10^{-7}$	$a'_2 = -6.599 \times 10^{-5}$	$a'_3 = -8.132 \times 10^{-12}$
$b'_1 = -6.005 \times 10^{-5}$	$b'_2 = 0.2252$	$b'_3 = 3.746 \times 10^{-9}$
$c'_1 = 0.0430$	$c'_2 = 0.3522$	$c'_3 = -6.902 \times 10^{-7}$
$d'_1 = -0.3808$		$d'_3 = 6.360 \times 10^{-5}$
		$e'_3 = -2.948 \times 10^{-3}$
		$f'_3 = 0.08253$

This final expression allows to optimize the weight factors  $W$  at all frequency steps and achieve the accuracy shown in Sec. 3.4, Fig. 3.6, for any profile shape that satisfies the boundary conditions assumed in this section. In the next section, the Eq. 3.28 and the parameters in tables 3.1 and 3.2 are used to optimize the  $W$  profile and reconstruct the density profile of a worst case example, given in Fig. 3.17, including the complication of using less frequency steps.

### 3.9 Reconstructions with less probing frequencies

Up to now, all profile reconstructions obeyed the rule of more probing frequencies resulting in better accuracy, which is mainly because the refractive index shape is better described by a square root function the smaller is the radial step. In addition, the error introduced by miscalculating the area under the refractive index curve is proportionally bigger to the increase of the radial step, emphasizing the previous feature. With the results of Sec. 3.8, however, the mismatch in the shape of the refractive index can be corrected. Therefore, the profile can be reconstructed using less probing frequencies without a significant loss of accuracy.

Using less probing frequencies speeds up the reconstruction algorithm, allowing for monitoring of faster density profile evolution. This was tested for the Tore Supra example profile when reducing the number of frequencies from 500 to 100 and speeding up the reconstruction for roughly about five times, depending on the computer conditions. In this case, the fluctuations in the edge region peak at 1 cm when the factor  $W$  is fixed at  $2/3$ . When  $W$  is optimized for all steps, the discrepancy profile goes back to values below 1 mm.

Other situations that the reconstruction accuracy is significantly improved by optimizing the  $W$  factor are scenarios with very low or very high background magnetic fields. The refractive index in each previous positions,  $N_{n-1}$ , is closer to one the greater is the difference between  $f_{ce}$  and  $f_{pe}$ , which causes the factor  $W$  to increase resulting in a degradation of the reconstruction accuracy when using a fixed  $W$ , as in the square root method. To demonstrate this scenario, a low density profile linear in  $f_R$  with  $\nabla f_R = 20 \text{ GHz}/m$  is assumed. In this condition, no pedestal is present and it is not clear where the square root function describes well the refractive index shape. In addition, the number of probing frequencies for the reconstruction is reduced to 50. The resulting frequency profiles are depicted in Fig. 3.16.

Applying the method developed in the last section gives the optimized  $W$  for each probing frequency. In this case, the  $W$  profile is never too close to the square root method

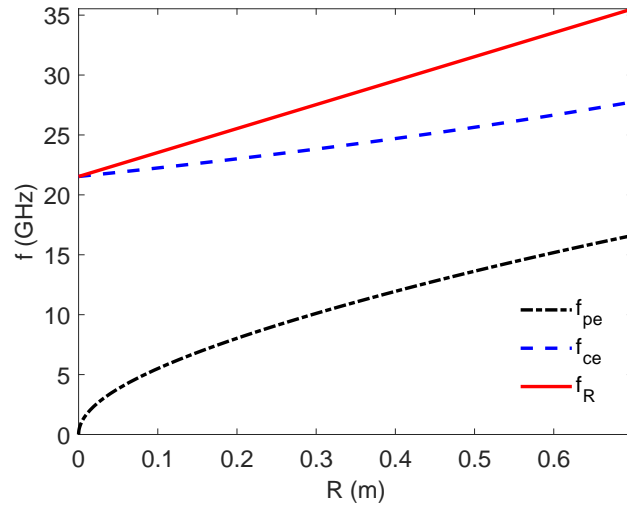


Fig. 3.16 Low density and magnetic field case with enforced linear profile in  $f_R$ , with  $\nabla f_R = 20 \text{ GHz/m}$ . This case represents the worst case scenario for the reconstruction algorithm if not optimizing the integration factors  $W$ .

solution of  $2/3$ . The  $W$  profile is always above  $0.7$ . The accuracy of the reconstructed profiles before and after optimizing the  $W$  profile is depicted in Fig. 3.17. A maximum error of  $0.4 \text{ mm}$  is observed in the reconstructed profile when the  $W$  profile is optimized. If reducing even more the number of probing frequencies, the radial steps become too large. In such cases, the error in the trapezoidal integration before the last step surpasses the error from integrating the last radial step. For all cases explored here, the error in the trapezoidal integration surpasses the error in the last step when the radial step surpasses  $5 \text{ cm}$ .

The reduction on the number of frequency steps was also tested in the Tore Supra example with the introduction of white noise in the time of flight and phase-shift data. When a low level of white noise is introduced, up to  $1\%$ , no difference is observed between the cases with  $500$  or  $100$  frequencies. For higher levels of noise the discrepancy in the core raises, doubling the noiseless value at around  $10\%$  noise level.

### 3.10 Conclusions

Following the recent advances and demands in the reflectometry techniques, deeper understanding and additional improvements on the density reconstruction method was investigated here in the data analysis front. A crucial point in the reconstruction method

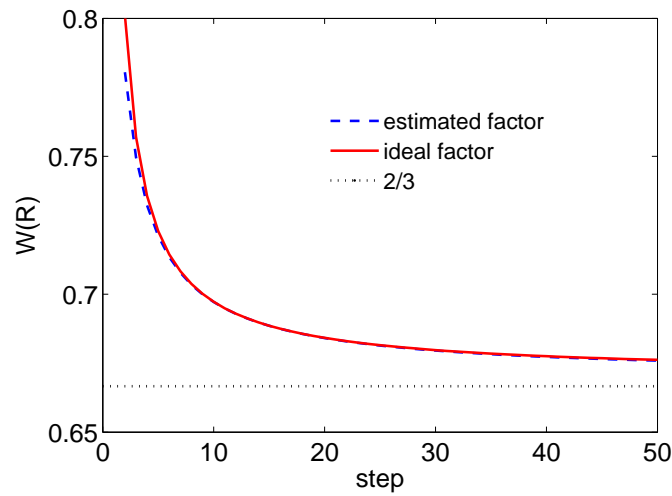


Fig. 3.17 Example of the optimization of the weight factor  $W(R)$ , as defined in Eq. 3.6, for a linear  $f_R$  profile and only 50 probing frequencies.

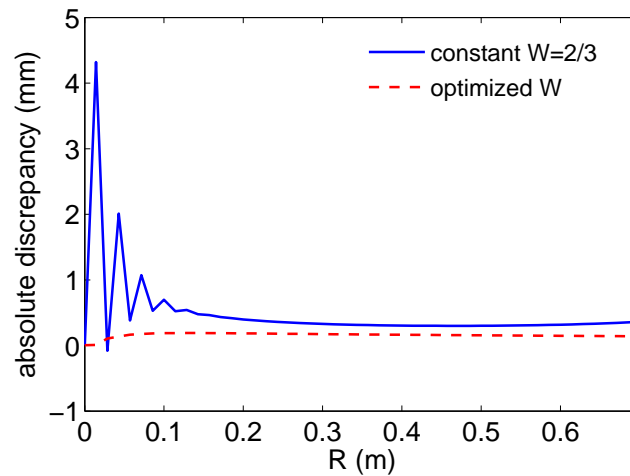


Fig. 3.18 Comparison of the absolute discrepancy profiles between a constant  $W = 2/3$  and the optimized  $W$  depicted in Fig. 3.17.

is the assumed refractive index shape in the integration over each radial step. It was demonstrated that using the radially optimized fractional power functions improved the reconstructed profile accuracy and stability because these functions describe well the true refractive index shape. Although the use of a square root profile achieved good results in the core plasma, it is not the best suited shape in the edge plasma. In this region, the power of the fractional power functions can be very close to zero in the first reflected frequencies. The adaptation of the power of these functions according to the plasma

profile showed an accuracy improvement in the edge plasma profile of up to two orders of magnitude. The exact improvement depends on the initialization precision and the profile to be reconstructed.

The comparison between all methods investigated also showed how the reconstruction is more stable when not using any information of the previously calculated positions to determine the next position, or even, forcing smoother variation on any of the reconstruction terms. All these procedures were demonstrated to delay the error damping capability of the reconstruction method when spurious events and phase noise were introduced. In addition, the analysis on the reconstruction stability deduced a better damping of errors for higher values of  $WN_{n-1}$ , which is typical of edge conditions.

When reconstructing a well known density profile shape containing a clear pedestal transition, the optimized integration shapes could be easily proposed. The bottlenecks of this implementation are: an evident transition to the pedestal; and the accuracy of the integration factor assumed in the first reconstruction step. The method elaborated in Sec. 3.8 suppresses these issues. It can be used to determine the entire profile of integration factors for any profile shape. Optimizing the integration factors also allow to use a reduced number of probing frequencies to reconstruct the profile without any accuracy loss, as demonstrated in two examples. This feature enables the real-time monitoring of faster density profile evolution.

The first experimental application on the results developed in this chapter were demonstrated for the first time in data from the Tore Supra database. This work was performed after the manuscript deposition and therefore it is included in Appendix A.

# Chapter 4

## Blind areas in frequency swept reflectometry

During a discharge in fusion experiments, many phenomena can introduce perturbations in the density profile. The small scale turbulence fluctuations generate an overall change in the acquired phase signal and the inversion process of the fluctuation properties is investigated via a transfer function, as initially approached in [68] and more recent developments are found in [69]. For isolated perturbations, the signature in the reflectometer signal is related to the size of the perturbation. The spectrum of the phase signal can be used to describe the perturbation shape in some small scale cases (in the order of the probing wavelength), as presented in [40]. In this situation, the probing electric field is still close to the unperturbed profile situation. Here, on the other hand, bigger perturbations, out of the Born approximation validity, are investigated, focusing on perturbations that introduce a valley in the density profile that is large enough such that the probing microwaves have no reflection inside the valley and the probing electric field is no more close to the unperturbed case. This situation can occur during massive gas and pellet injections [70], MHD activity [71] and in hollow profiles that emerge during the initiation of heating systems [72]. If the reconstruction method does not incorporate identification and reconstruction tools for these blind regions, big discrepancies can appear in the reconstructed profile. An example is shown in Fig. 4.1 using the WKB phase as the input signal and the standard Bottollier-Curtet algorithm with a fixed integration weight factor  $W$  equals  $2/3$  for all frequency steps. It is clear that the standard reconstruction does not describe well the perturbation. Furthermore, if the oscillations are smoothed, the perturbation can be neglected entirely, or even worse, a shift can be introduced in the reconstructed profile after the perturbation, as seen in Fig. 4.1.

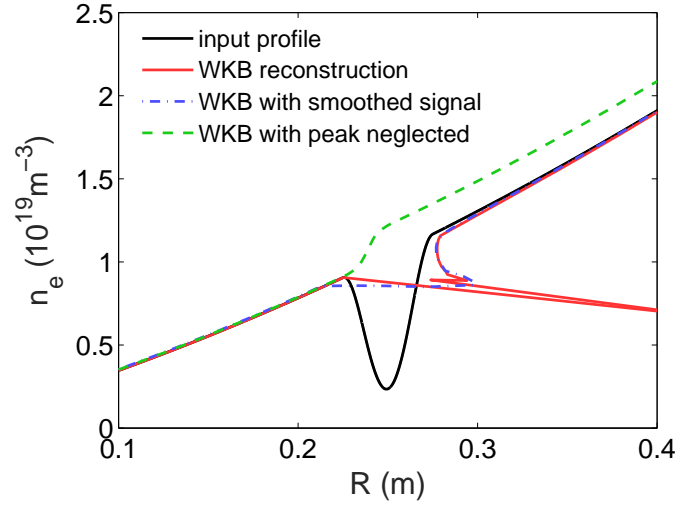


Fig. 4.1 Input and reconstructed density profiles containing a blind region. The profile was reconstructed with the standard Bottollier-Curtet algorithm with  $W = 2/3$  using three different treatments in the phase signal.

Even though the probing microwaves have no reflection inside the blind region, there is information to be explored from the higher frequencies that propagate through the perturbation. The parameters necessary to describe a perturbation are: the perturbation width; the perturbation depth; and the perturbation shape. For simplicity, the first perturbations investigated have a well known shape and width and are inserted in a region with linear  $f_R$  profile. This way the density profile can be reconstructed using an unperturbed signal, which can be from a previous sweep or an interpolation of the phase signal with the perturbation signature removed. Afterward, the perturbation signature is evaluated to determine its properties. To determine the perturbation depth, a signature in the time-of-flight signal is scaled to the perturbation depth (for an assumed width and shape). As a proof of concept, this procedure is developed in the next section for signals simulated using the WKB approximation. Afterward, the reflectometer signal is simulated with a 1D full-wave wave equation solver to take into account full-wave effects such as tunneling, wave-trapping, interference and scattering. Then, the influence of the perturbation shape on the perturbation signature is demonstrated, and lastly, the reconstruction techniques are discussed.

## 4.1 Proof of concept in WKB framework

In this section, a proof of concept is done using the simplest simulation of the measured phase signal. The phase is computed under the WKB approximation, as presented in Eq. 3.5, and the time-of-flight can be directly calculated taking the phase derivative with respect to the probing frequency. The simplest interpretation of this problem is to relate the jump amplitude in the time-of-flight signal when going through the valley, to the depth of the perturbation with an assumed shape and a fixed width. In Fig. 4.2, it is shown the time-flight signal computed under the WKB approximation for the input profile presented in Fig. 4.1.

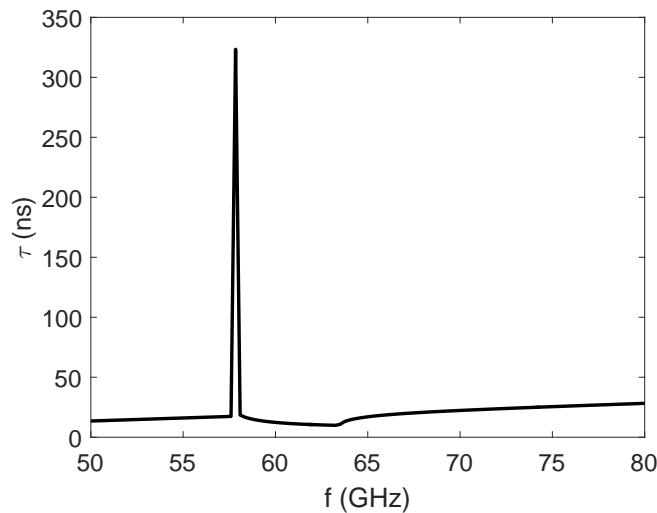


Fig. 4.2 Time-of-flight during a frequency sweep, computed under the WKB approximation for the example input density profile of Fig. 4.1.

The height of the peak present in the phase increment signal, i.e. the time-of-flight can be directly related to the perturbation depth, as long as the perturbation width and shape are fixed. In Fig. 4.3, it is illustrated the obtained relation when inserting sine shaped perturbations with a fixed width and radial position, on fixed profiles of  $f_{pe}$  and  $f_{ce}$ .

Using this relation, one can reconstruct a perturbation profile that is inside of the boundary condition assumed. All possible profile shifts can be avoided if the time-of-flight signal over the perturbation is skipped entirely when applying the profile reconstruction. After determining the unperturbed profile, the perturbation is estimated with the relation in Fig. 4.3 and inserted back into the reconstructed profile.

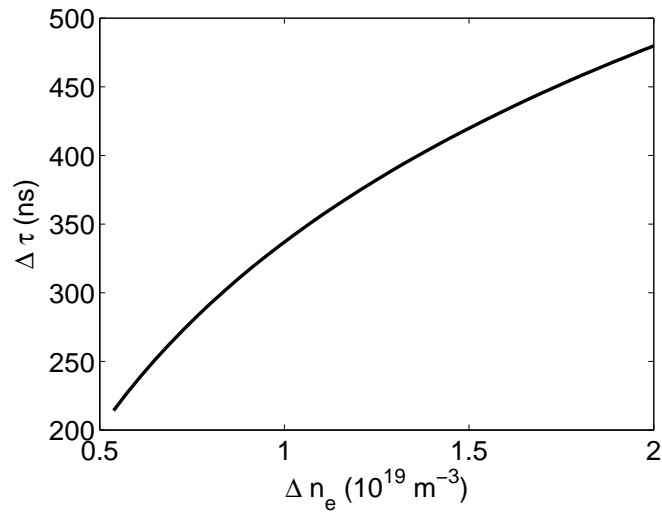


Fig. 4.3 Relation of the time-of-flight jump to the depth of a sine shaped perturbation with a fixed width and radial position, inserted on fixed profiles of  $f_{pe}$  and  $f_{ce}$ .

Applying this procedure to the example case of Fig. 4.1 results in the reconstructed profile presented in Fig. 4.4.

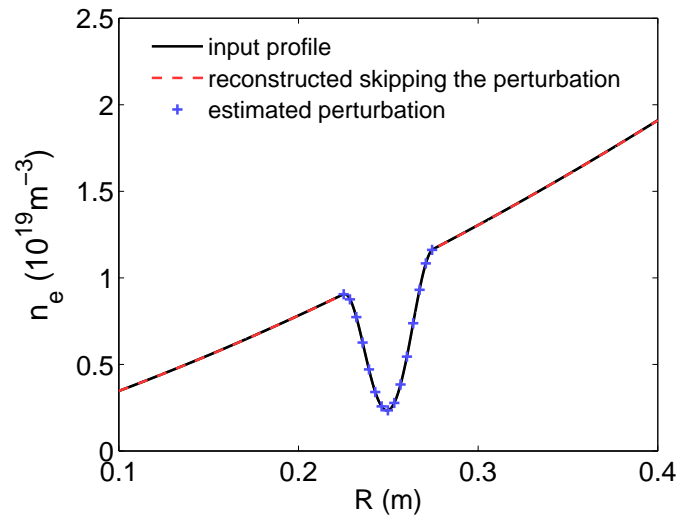


Fig. 4.4 Input and reconstructed density profiles. The reconstructed profile is divided into a regular reconstruction skipping the perturbation, plus the estimated perturbation. The perturbation is estimated using the relation in Fig. 4.3 for a sine shaped perturbation with a fixed width.

The procedure described above can successfully reconstruct the density profile of blind regions under the assumed conditions. However, the experimental signals are more complex than the WKB solution. In the next sections, a full-wave, 1D wave equation solver code is used to simulate the time-of-flight signals. Not only the WKB solution is out of its domain of validity in some parts, but in addition, time-dependent full-wave phenomena are present in the full-wave simulated signals. Therefore, these additional effects must be taken into account to build new relations like the one demonstrated in Fig. 4.3 for the valley estimation from experimental data. Moreover, these relations will vary with the perturbation parameters of shape and width, and the local profile parameters of  $\nabla f_R$  and  $f_{ce}$ , thus, these dependencies are also taken into account. Lastly, there is information on the time-dependent full-wave effects that theoretically can be investigated to deduce the perturbation shape.

## 4.2 Introduction to time dependent full-wave effects in the simulated signals

In order to investigate the full-wave effects from the blind regions covered here, the perturbations are introduced in a linear cut-off frequency profile ( $f_R$ ). Since the phase evolution depends not only on the density but also on the magnetic field, working in the  $f_R$  framework allows to account for both the density and the magnetic field together. Later on, the dependency on the  $f_{ce}$  profile is also taken into account when generalizing the determination of the perturbation signature. It becomes more crucial when investigating perturbations near the plasma edge, where the density can be very low and  $f_R$  approaches  $f_{ce}$ . Before then, the  $f_{ce}$  profile is fixed for all the following analyzes of full-wave effects, focusing in perturbations in the core plasma of latest generation tokamaks. For such, the magnetic field strength is fixed at 3.2 teslas at the plasma center and a standard tokamak 1/R radial dependency. The density profile is assumed linear from the edge until reaching  $6 \times 10^{19} m^{-3}$  in the center. Consequently, the perturbations placed halfway between the plasma edge and the plasma center have density near  $3 \times 10^{19} m^{-3}$ , magnetic field at three teslas, and are probed at around 100 GHz.

In this section, the perturbations are subtracted exclusively from the  $f_R$  profile with a sine squared shape, ranging from zero to pi, and size in the scale much larger than the probing wavelength in vacuum. The sine squared shape was chosen for its characteristics of having null magnitude and derivative each half wavelength. This allows for smooth local implementation on top of the assumed profile. An example of such a perturbation is presented in Fig. 4.5, with 6.4 cm width and varying depth. The respective time-of-flight

signals extracted with the IQ detection technique, as introduced in Sec. 1.3.1, are presented in Fig. 4.6.

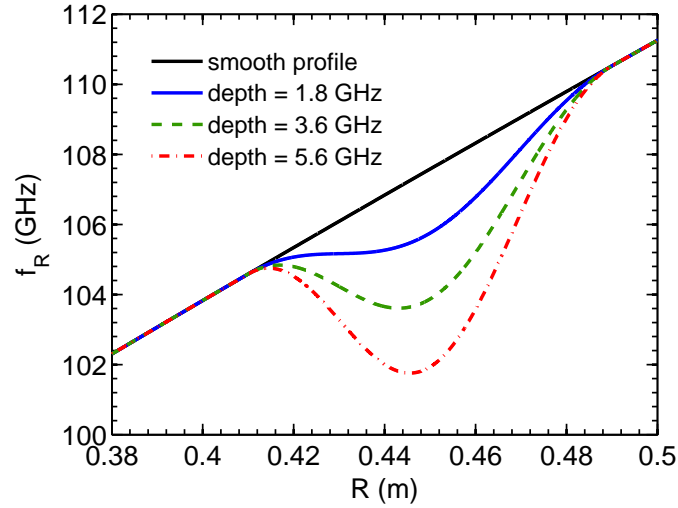


Fig. 4.5 Linear  $f_R$  profiles with sine square shaped valleys of different depths.

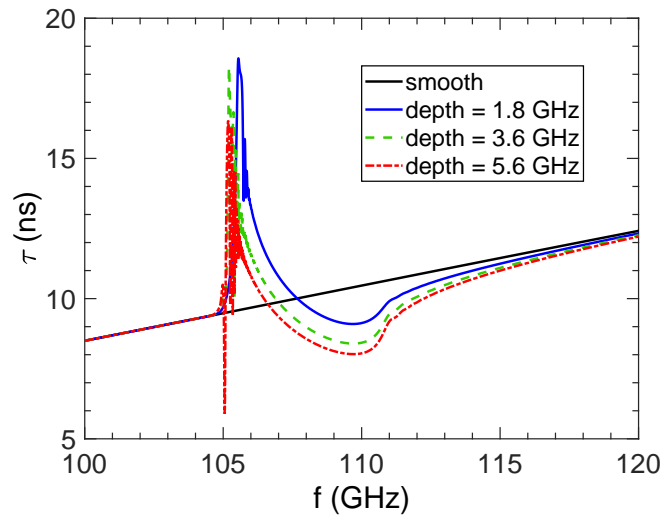


Fig. 4.6 Time-of-flight signals from the profiles introduced in Fig. 4.5, calculated with the IQ method as presented in section 1.3.1. The sweeping rate used was  $20 \text{ GHz}/\mu\text{s}$ .

As can be seen in Fig. 4.6, the height of the peak in time-of-flight is no longer a good scaling parameter to the perturbation depth, as done in the previous section when the phase is computed in the WKB framework. The reason is because of the presence of big

fluctuations in the vicinity of the time-of-flight peak. Other features along the higher frequencies need to be explored in order to extract information from the perturbation size. But first, all full-wave effects are discussed in order to clarify all features in the full-wave signals. There is a brief explanation below of which are the full-wave effects encountered, and a more detailed observation of each effect is presented in separated sections below.

The fluctuations around the time-of-flight jump are interferences due to the frequency mixing caused by the time-dependent effects around the perturbation. As the probing frequency is swept and arrives at the jump frequency, there will be a small band of frequencies that will partially tunnel into the perturbation. The tunneling effect is further explored in Sec. 4.3. In the most complicated scenarios, the tunneling interfaces followed by the valley can act as a system of three partially reflecting mirrors. Between the three mirror system, specific frequencies can be trapped for a longer period and return mixed in the reflected signal. The frequency mixing also occurs when the plasma is probed just above the perturbation frequency. In this case, the probing wave propagates much slower through the perturbation because it is close to its cutoff frequency. All these effects contribute to the frequency mixing generating the interference observed around the time-of-flight jump.

The interfaces between the tunneling boundaries and the valley can be interpreted as cavities that can fulfill a resonance condition [73]. When this condition is fulfilled, a spike is seen in the time-of-flight signal at the resonant frequency. Some resonance cases are observed in Sec. 4.4.

The reflection coefficient of each interface in such three mirror system can be computed from the refractive index jump, according to Ref. [74]. Steep jumps in refractive index can also lead to strong Bragg backscattering for the probing frequencies above the perturbation. This effect is demonstrated analytically in Ref. [75], and can be observed in Sec. 4.5 for a square perturbation.

These new full-wave features introduced above are discussed in more detail in Secs. 4.3, 4.4 and 4.5, followed by an analysis on the perturbation shape. The influence on the time-of-flight signal from the perturbation skewness and kurtosis is discussed in Secs. 4.6.1 and 4.6.2, respectively.

Lastly, the reconstruction technique is discussed. As can be seen in Fig. 4.6, the size of the jump in the time of flight signal is not anymore a good scaling feature of the perturbation signature because this area is very prone to interferences. Instead, the inversion methods need to extract the information from the higher frequencies. An example method is proposed to estimate the size of  $\text{sine}^2$  perturbations in Sec. 4.7 using

the integral of the perturbation signal, followed by a discussion on multiple perturbations in Sec. 4.8 and a general procedure regardless of the perturbation shape and size in Sec. 4.9.

### 4.3 The amplitude drop related to the tunneling and frequency mixing effects

An additional information from the full-wave signal is the receiving wave amplitude extracted using the IQ detection method, as seen in Fig. 4.7 for the cases in Fig. 4.5.

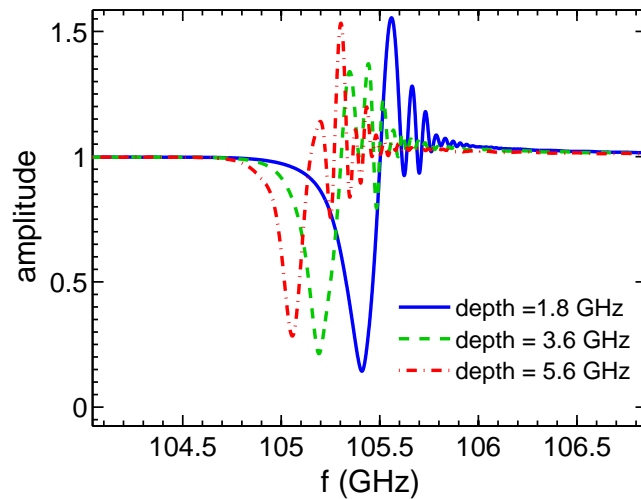


Fig. 4.7 Amplitude from the profiles introduced in Fig. 4.5 with valleys of 8 cm width, calculated with the IQ method as presented in Sec. 1.3.1, swept at 20 GHz/ $\mu$ s.

The drop in the amplitude signals reveal the existence of a valley in  $f_R$ , even if no blind region is introduced. The amplitude changes are due to the electromagnetic flux conservation and the frequency mixing effect. Apart from the electromagnetic flux conservation, as the probing frequency approaches the jump over a blind region, the microwaves start to partially tunnel into the perturbation causing the IQ amplitude to decrease. The frequencies that partially tunneled into the perturbation eventually return to the antenna later on. This is why the amplitude drop is followed by an amplitude increase. As these delayed waves return to the antenna, they interfere with higher probing frequencies, which explains the fluctuations after the initial amplitude dip. The way these frequencies are mixed strongly depends on the quality factor of the cavities (inside the tunneling region or inside the perturbation) combined with the sweeping rate of

the probing frequency. The quality factors dictates the interference amplitudes and the sweeping rate dictates the interference bandwidth. For simplicity, all the analyzes on the time-dependent full-wave effects are done for the fixed sweeping rate of  $20 \text{ GHz}/\mu\text{s}$ , which is the fastest sweeping system in place today, as used in Tore Supra and ASDEX Upgrade.

Apart from the interferences due to the wave-trapping in the cavities, additional reflections can emerge from Bragg backscattering when the spectrum of the inserted perturbation contains wave-numbers fulfilling the Bragg rule. In the end, the interferences can originate from one or many of these sources. The case presented in Fig. 4.7 exhibits only one oscillating frequency after the amplitude drop. For the same perturbation shape and sweeping rate, reducing its width causes an interference to appear as soon as the amplitude starts to drop and an additional modulation frequency after the amplitude drop, as seen in Fig. 4.8 at 4 cm perturbation width. Another example is given in Fig. 4.9, where the barrier before the valley is reduced to 1 cm but the valley is extended to 40 cm. In this case, as soon as the amplitude starts decreasing, two very distinct interference frequencies are formed.

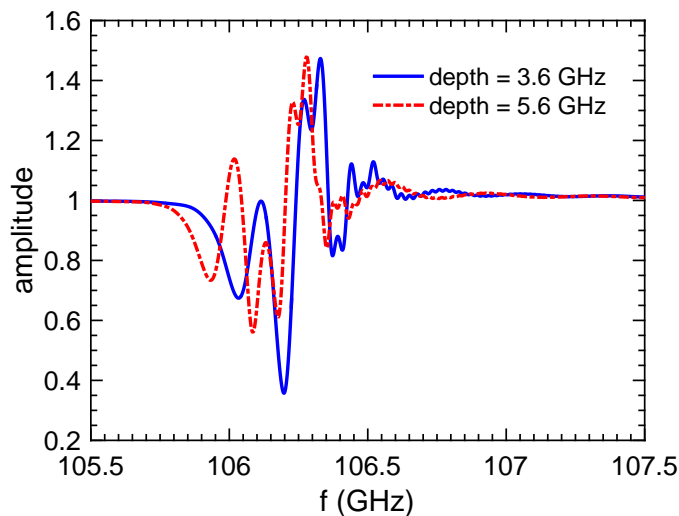


Fig. 4.8 IQ amplitude of sine squared valley perturbations as introduced in Fig. 4.5 but with width reduced to 4 cm. The probing frequency is swept at  $20 \text{ GHz}/\mu\text{s}$ .

The cases presented in Figs. 4.7, 4.8 and 4.9 demonstrate a few examples of difference mixes of multiple interferences. Although each interference frequency contain information from its origin, it is just not possible to discriminate such low amplitude mixed fluctuations due to the inherent noise level in experimental signals. Nevertheless, the bandwidth of

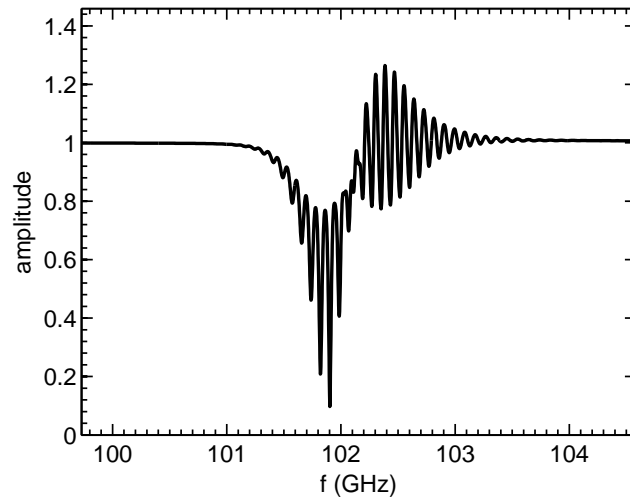


Fig. 4.9 IQ amplitude crossing a narrow barrier of 1 cm and jumping over a 40 cm wide perturbation. The probing frequency is swept at  $20 \text{ GHz}/\mu\text{s}$ .

the amplitude drop is still observable and this section now focuses on observing this feature in more detail.

The time at which the tunneled waves return is impossible to be accurately determined experimentally. The frequency at which the microwaves start tunneling, on the other hand, are related to the probing frequency and the barrier width. For the tunneled waves to be reflected back, they must have an evanescent path equal or longer than the width of the barrier to cross into the perturbation. The analytical expression for the fields of the evanescent wave is demonstrated in Ref. [74]. In practice, the tunneling band is explored in this section for varying probing frequencies and perturbation width. The simulations performed involved having a sine square bump on top of a plateau, as depicted in Fig. 4.10. After going through the top of the perturbation, the waves are damped in the end of the simulation grid on a perfectly matching layer.

The respective simulated amplitude signal over the middle perturbations is given in Fig. 4.11. Because in this condition no waves return after they go through the perturbation, the amplitude signals decrease until being zero. The rate of the amplitude drop is related to the probing frequency and the perturbation width. One way to measure the drop rate is to relate the half amplitude drop to the frequency band necessary to achieve it. Doing this for varying widths and probing frequencies lead to the relations in Fig. 4.12.

Fig. 4.12 shows that there is little dependency on the probing frequency, compared to the dependency on the perturbation width. Regardless of the presence of interferences,

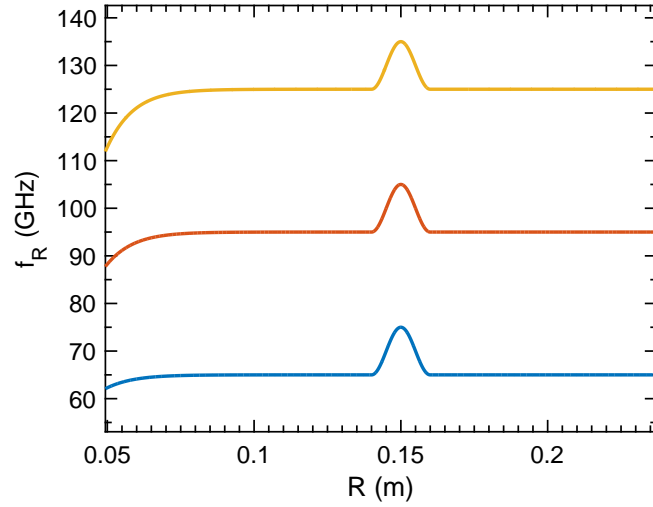


Fig. 4.10 Perturbations with sine square shape for the investigation of the tunneling over the perturbation tip at varying probing frequencies. To accommodate these probing frequencies, the bottom case was set with  $B_{core} = 2.3T$  and the plateau with  $n_{plateau} = 10^{19}m^{-3}$ , the top case with  $B_{core} = 2.65T$  and the plateau with  $n_{plateau} = 10^{20}m^{-3}$ , while the middle case kept the higher magnetic field and decreased the plateau density to  $4 \times 10^{19}m^{-3}$ .

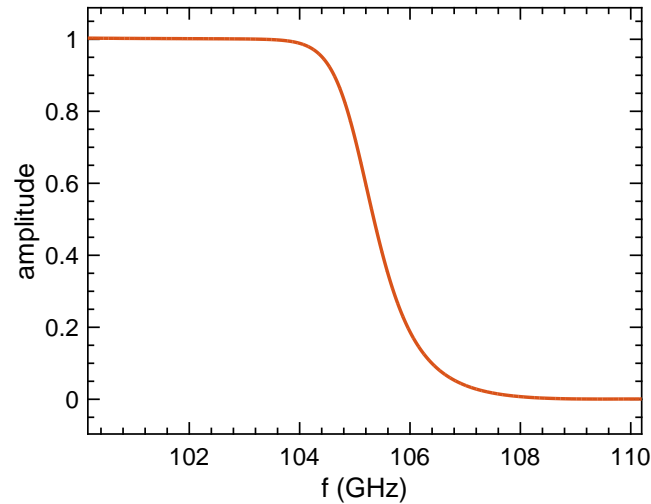


Fig. 4.11 Drop in amplitude from sweeping at  $20 \text{ GHz}/\mu\text{s}$  through the middle perturbation in Fig. 4.10 until no signal returns.

the initial frequency where the amplitude starts to decrease marks the start of the

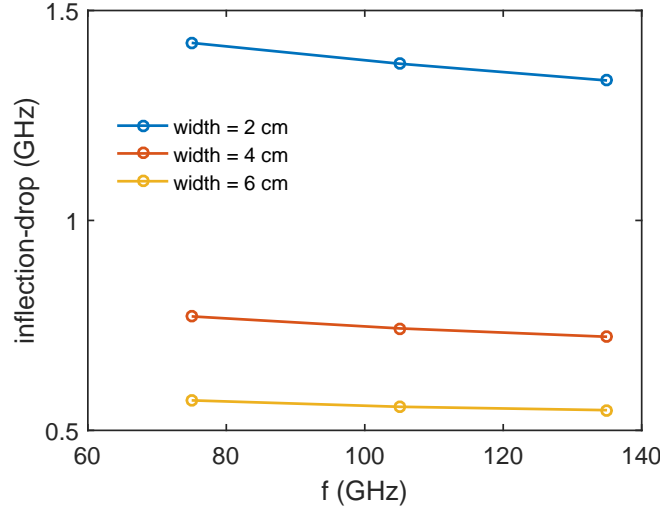


Fig. 4.12 The drop in amplitude observed for varying peak widths and probing frequencies at the sweeping rate of  $20 \text{ GHz}/\mu\text{s}$ .

tunneling effect. By knowing the injected frequency, and therefore the value of  $f_R$ , the radial evanescent wave amplitude can be computed, according to [74], by:

$$A_{ev} = A_0 e^{-k\chi r}, \quad (4.1)$$

with  $A_{ev}$  being the evanescent wave amplitude,  $A_0$  is the impinging wave amplitude, and  $\chi$  is the imaginary part of the refractive index.

By having the local plasma parameters to compute  $\chi$ , the path length of the evanescent wave can be computed, i.e. the thickness of the barrier on that probing frequency. This information gives part of the shape around the jump frequency. It can be used as a constraint on the shape assumed for the blind area.

The analysis on the rate of amplitude drop was done using the sweeping rate of  $20 \text{ GHz}/\mu\text{s}$ . Changing the sweeping rate affects the amplitude drop rate due to the electromagnetic flux conservation, and this has to be taken into account if transferring these results into a different set-up.

## 4.4 Resonances

If one cavity on the three mirror system has a high quality factor and resonates with a specific injected frequency, a resonance appears on the time of flight signal. Figs. 4.13 and 4.14 show a positive and a negative spike due to resonances. The response is sensitive

to the frequency sweeping rate because the quality factor of the cavity influences the build up and relaxation of the trapped waves.

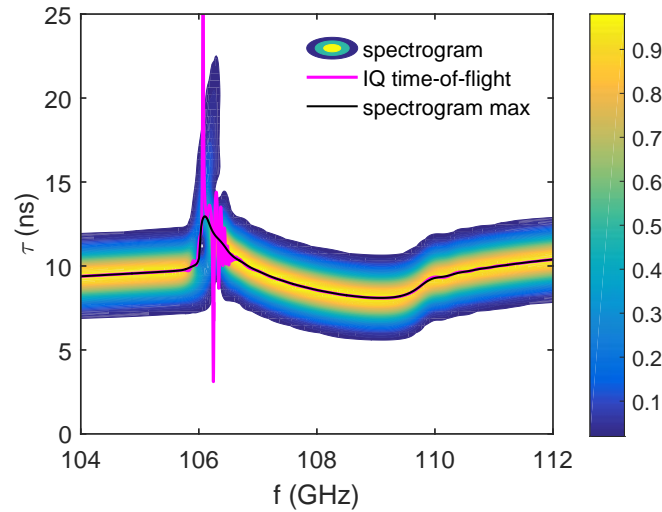


Fig. 4.13 IQ spectrogram and instantaneous frequency signals with a positive resonance case. The profiles used are the standard study case resulting in background density of  $3 \times 10^{19} m^{-3}$  and magnetic field of 3 teslas at the perturbation location. The perturbation introduced has a sine square shape with 5 cm width and depth in the density profile of  $0.66 \times 10^{19} m^{-3}$ .

For usual resonances on smooth perturbations, the injected waves are not trapped for a long time. This is observed on Figs. 4.13 and 4.14 because the spectrogram signal does not show any long lasting frequency after the peak in the time of flight. The resonance peak is apparent in the instantaneous frequency signal but seems to not significantly disturb the spectrogram signal. The modulation and resonances are very hard to identify in experimental data because of the innate noise level in experimental signals. Thus, the inversion technique is more robust if using a bigger bandwidth with the frequencies above the time of flight jump. In addition, the maximum of the spectrogram is the signal less sensitive to these modulations, compared to the instantaneous frequency signal.

In the next section, a square perturbation is introduced in the  $f_R$  profile to enhance the Bragg backscattering and the reflections in the three mirror system.

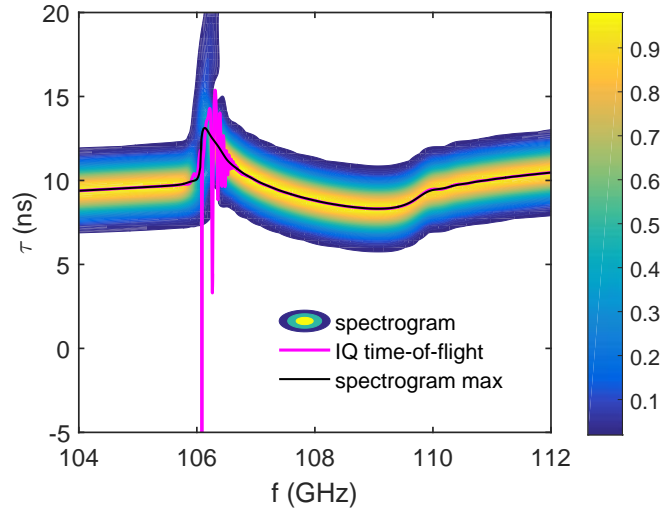


Fig. 4.14 IQ spectrogram and instantaneous frequency signals with a negative resonance case. The profiles used are the standard study case resulting in background density of  $3 \times 10^{19} m^{-3}$  and magnetic field of 3 teslas at the perturbation location. The perturbation introduced has a sine square shape with 14 cm width and depth in the density profile of  $0.66 \times 10^{19} m^{-3}$ .

## 4.5 Reflections and Bragg backscattering from square perturbations

As introduced in Sec. 4.3, the Bragg backscattering and the reflections in the perturbation three mirror systems are enhanced for a sharper and larger refractive index change. In order to illustrate a case with strong wave trapping, resonance conditions and Bragg backscattering, a square perturbation shape is introduced in the  $f_R$  profile as in Fig. 4.15.

The IQ spectrogram and instantaneous frequency signals are presented in Fig. 4.16. The instantaneous frequency signal shows many resonant frequencies and reflections. After the time-of-flight jump, two additional branches arise oscillating in the spectrogram. The upper branch belongs to waves that were trapped and arrive later in the antenna, and the lower branch belongs to reflections that occurred before the cut-off frequency, i.e. the Bragg backscattering component. The spectrogram maximum signal is still smooth and continuous but contain small fluctuations. In order to remove these effects from the main reflection in the cut-off, one can use tomography techniques to apply a narrow band filter that follows the beat frequency evolution, as introduced in [51]. The different frequency components being trapped inside the perturbation can also be

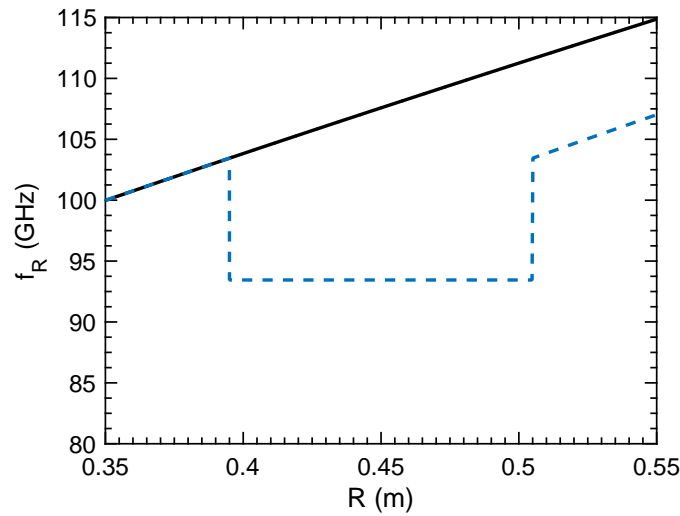


Fig. 4.15 Square perturbation to investigate the uniformity of the time-of-flight contribution across the perturbation.

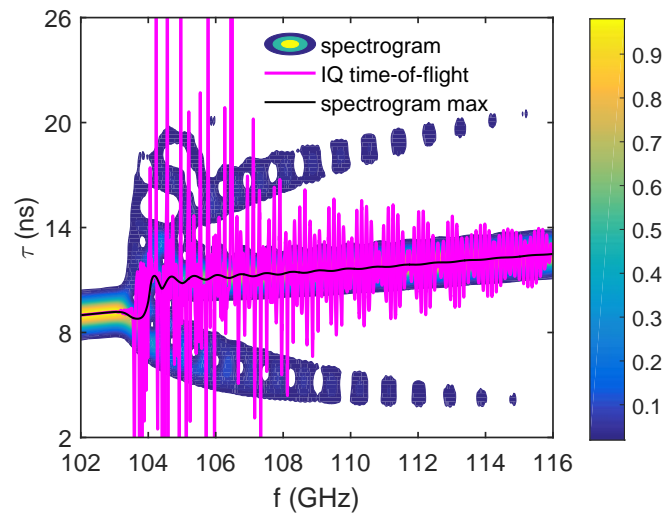


Fig. 4.16 IQ spectrogram and instantaneous frequency signals for the square perturbation on Fig. 4.15.

observed if plotting the spectrogram of the electric field inside the perturbation, as in Fig. 4.17. In this case it is more evident to see which are the trapped frequencies and how fast they exit the perturbation. The band around the first frequencies going through the perturbation are very well trapped and end up never fully exiting the perturbation during this short simulation. The tunneling of the lower frequencies are also visible,

although less intense, and are trapped for a short period. The elongation of a higher frequency, around half GHz above trapped frequency, shows a resonance, although not trapped shortly. The resonance condition seems to be roughly  $\pm 0.5$  GHz around the strongly trapped band. At these frequencies there is a small trapping of the tunneled frequencies and on the probing frequencies above. Although a square perturbation is not very realistic, additional echoes are seen quite often experimentally and this analysis can be extended to these cases. The square perturbation is analyzed again in the next section when investigating the shape influence on the time-of-flight jump.

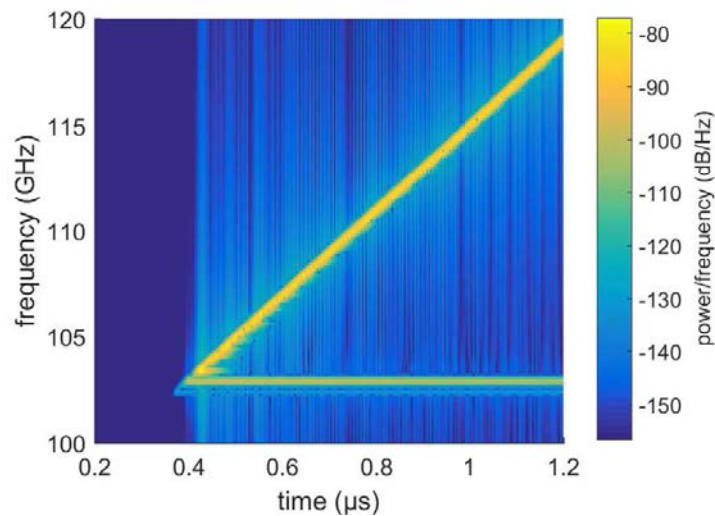


Fig. 4.17 Spectrogram of the electric field inside the square perturbation from Fig. 4.15.

## 4.6 Influence of the perturbation shape on the time-of-flight signal

The observation of all full-wave effects demonstrate that there is much more information in the reflectometer signals than just the amplitude of the time-of-flight jump. Moreover, the time-of-flight signal is highly susceptible to interference fluctuations around the jump. Therefore, analyzing the higher frequency band becomes a robust path. The occurrence of each full-wave effect is strongly linked to the width between the different interfaces. However, when exploring the time-of-flight signal in the higher frequencies band, the signal is also dependent on the shape of the perturbation. This section explores the influence of the perturbation shape by investigating the impact on the time-of-flight

signal by changing the perturbation skewness and kurtosis. The skewness is an indication of the asymmetry of a distribution around its mean value. It is mathematically defined as  $\gamma_1$  in Eq. 4.2, according to Pearson's notation [76].

$$\gamma_1 = \frac{\mu_3}{\mu_2^{3/2}}, \quad (4.2)$$

with  $\mu_i$  being the  $i$ th central moment, and  $\mu_2$  in particular, being the variance.

The kurtosis is an indication of how a distribution is concentrated near the mean value or more spread with long tails. It is mathematically defined as  $\beta_1$  in Eq. 4.3.

$$\beta_1 = \frac{\mu_4}{\mu_2^2}, \quad (4.3)$$

A moment  $\mu_i$  of an univariate probability density function  $P(x)$  can be defined as:

$$\mu_i = \langle (x - \langle x \rangle)^i \rangle \quad (4.4)$$

$$= \int_{-\infty}^{+\infty} (x - \mu)^i P(x) dx. \quad (4.5)$$

The skewness and kurtosis are investigated separately in the next two subsections.

#### 4.6.1 Effect from the perturbation skewness.

The skewness of a perturbation can be understood as the perturbation radial symmetry. The phenomenon was firstly observed by using skewed triangular shapes and noting how the time-of-flight evolved through the perturbation. To illustrate the effect of the radial non-uniform contribution to the time-of-flight signal, the symmetrical square perturbation of Fig. 4.15 is investigated. The resulting refractive index inside this perturbation can be observed in Fig. 4.18 for a probing frequency just above the time of flight jump.

The radially non-uniform refractive index distribution inside the perturbation, as seen in Fig. 4.18, is caused by the radially non-uniform ratio of  $f_{pe}$  to  $f_{ce}$ . Although this effect is visible, it is a second order effect and will be neglected in the perturbation reconstruction techniques in the plasma core, since this ratio will not vary much. This effect will be revisited when investigating blind regions in the presence of very low densities in the initialization study in the next chapter.

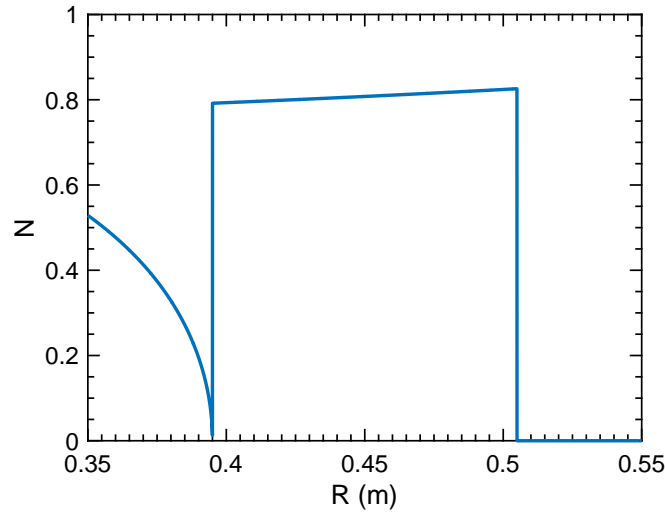


Fig. 4.18 Refractive index of a uniform square perturbation, as introduced in Fig. 4.15, when probed with a frequency just above the valley.

#### 4.6.2 Effect from the perturbation kurtosis.

The kurtosis of the perturbation is an indication if the perturbation is more concentrated in the center or in the extremities. To investigate this effect, three shapes of perturbation are introduced in the  $f_R$  profile, as depicted in Fig. 4.19.

The three shapes chosen have the same area in the  $f_R$  profile, i.e.  $\int_{width} f_R dR = const.$  Since the time-of-flight jump is related to the refractive index area over the perturbation, this effect can be seen in the refractive index profile across these perturbations, as given in Fig. 4.20 for a probing frequency just above the time of flight jump. They are related to the time-of flight because the area of the refractive index gives the phase, by Eq. 3.5, and the time-of-flight is the derivative of the phase.

Fig. 4.19 shows how the different perturbations have decreasing area in the refractive index profile as the kurtosis is increased (the perturbation becomes more elongated). The best way to make clear which radial positions contribute more to the time-of-flight jump, is to compute the profile of the differential time-of-flight when probing with a frequency slightly above the perturbation. The result is illustrated in Fig. 4.21. The total time-of-flight after crossing the perturbation is given by the area under the differential time-of-flight, as it is given in the legend of Fig. 4.21.

Fig. 4.21 shows how the perturbations cause a larger time-of-flight contribution the higher is the  $f_R$  in the borders of the perturbation, or equivalently, the more they are elongated if keeping a constant area. This happens because the probing waves propagate

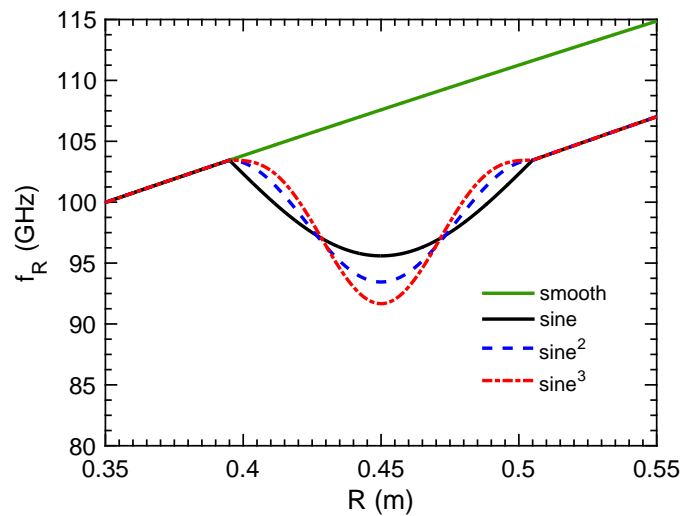


Fig. 4.19 Perturbations with varying kurtosis over a linear  $f_R$  profile.

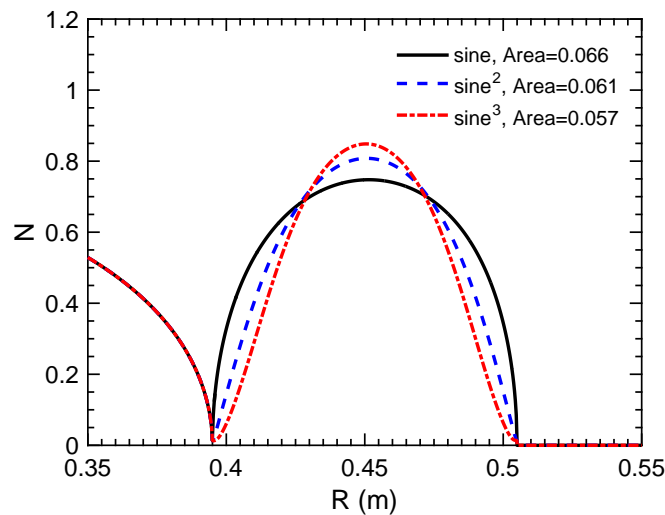


Fig. 4.20 The refractive index profile inside the perturbations with varying kurtosis from Fig. 4.19.

much slower when propagating through a region with  $f_R$  close to the probing frequency. This means that the bottom of the perturbation is shown in Fig. 4.21 to have a much lower contribution to the time-of-flight jump compared to the edges.

This effect raises another question. If the bottom of a valley perturbation has less impact on the time-of-flight, it means that the deeper the valley is, the less visible the signature of a given  $\delta f_R$  will be. This accuracy can be inferred by analyzing perturbations

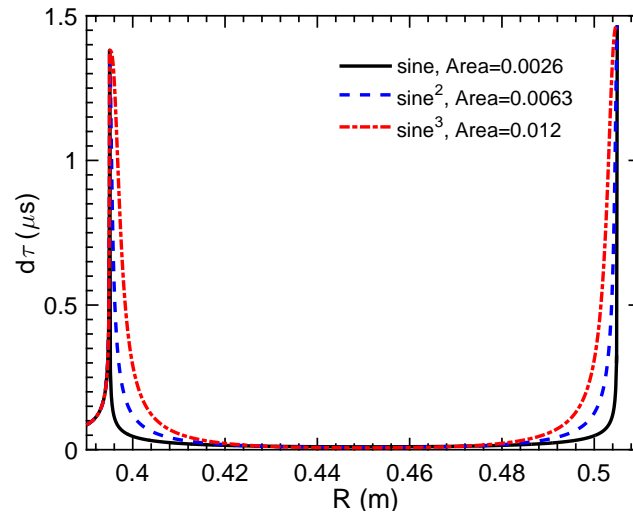


Fig. 4.21 Differential time-of-flight when probing with a frequency slightly above the perturbations of Fig. 4.19.

with different depth, and comparing the time-of-flight after the perturbation, with versus without an additional  $\delta f_R$  of constant area in  $f_R$ . The profiles simulated for this case are displayed in Fig. 4.22.

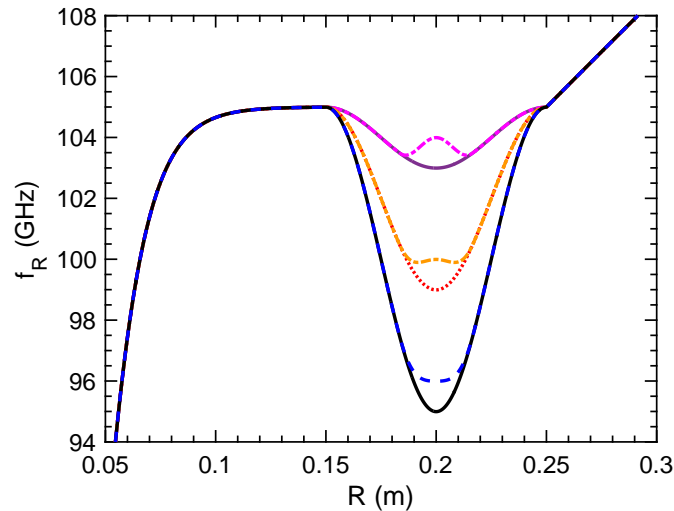


Fig. 4.22 Profiles with  $\sin^2$  perturbations of varying depths, with and without an additional  $\delta f_R$  of constant area. The plateau before the perturbation is introduced to decrease the frequency bandwidth tunnelled into the perturbation. Doing so reduces the interferences, and therefore, reduces the fluctuations on the time-of-flight signal.

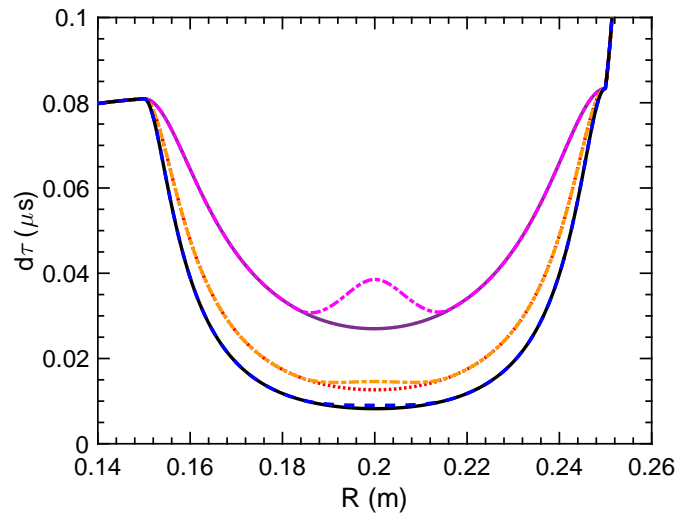


Fig. 4.23 Differential time-of-flight for the profiles in Fig. 4.22 when probing slightly above the perturbation.

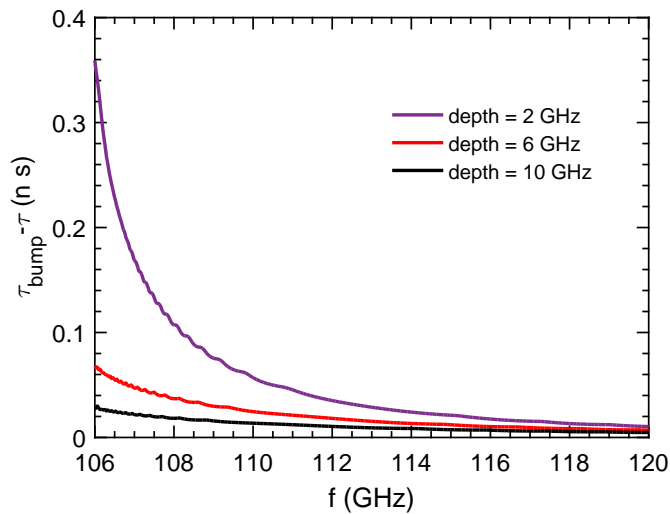


Fig. 4.24 Time-of-flight difference between valleys without and with a positive  $\delta f_R$  perturbation, as introduced in Fig. 4.22. The probing frequency range starts just after the jump in time-of-flight.

Computing the differential time-of-flight when probing at a frequency slightly above the perturbation gives the results in Fig. 4.23.

Fig. 4.23 shows that the deeper is the perturbation, the less visible the contribution from the  $\delta f_R$  becomes. To determine exactly how much is this difference, Fig. 4.24 shows

the time-of-flight difference between the profile with and without the  $\delta f_R$ , at the three different depths studied. The  $\delta f_R$  introduced causes an observable contribution in the time-of-flight when the valley is a few GHz deep. However, its contribution on a valley 10 GHz deep is quite small. In an experimental signals with significant background noise, such small structures inside deep valleys are indiscernible.

This concludes the investigation of the full-wave effects and the perturbation shape influence on the time-of-flight signal. The next section resumes the discussion on the reconstruction method for the perturbations.

## 4.7 A method to estimate the perturbation size with fixed conditions

The first step to estimate the perturbation profile is to detect that a perturbation exists. This can be done from the drop in amplitude coupled to the jump in the time-of-flight signal. The start point of the perturbation is still possible to be conventionally determined, and the end point is either directly after the jump, or it is marked with the bottom of a valley in the time-of-flight signal in the cases that the perturbation ends shortly after the time-of-flight jump. The parameters left to be determine are the perturbation depth and shape. The shape is assumed known in this first instance and in the future, the full wave effects could be explored to extract information about the perturbation shape. The depth can be scaled to the perturbation signature similarly to the WKB approach in Sec. 4.1. However, as it was demonstrated, the amplitude of the jump in time-of-flight is not a consistent scaling parameter anymore, because of the tunneling, frequency mixing and resonance effects already discussed. However, these effects appear in a narrow band around the time-of-flight jump. For the sweeping rate of 20 GHz/ $\mu$ s used throughout this chapter, the bandwidth of the strong interferences is limited to between 0.5 and 1 GHz before and after the time-of-flight jump, depending on the specific conditions. Away from this band width the signal is again compatible with the WKB approximation and have other intuitive scaling features. One example taken from Fig. 4.6 is the integral of the time-of-flight taken from the point after the jump where it crosses the unperturbed signal, until it converges back to the unperturbed signal. An example of this calculation is displayed in Fig. 4.25.

From Fig. 4.25, it is evident that the bigger the perturbation, the bigger is the integral of these signals until it converges back to the unperturbed case. For each fixed width, scanning the perturbation depth and computing the integral of the signals as displayed in Fig. 4.25 results in the relations present in Fig. 4.26.

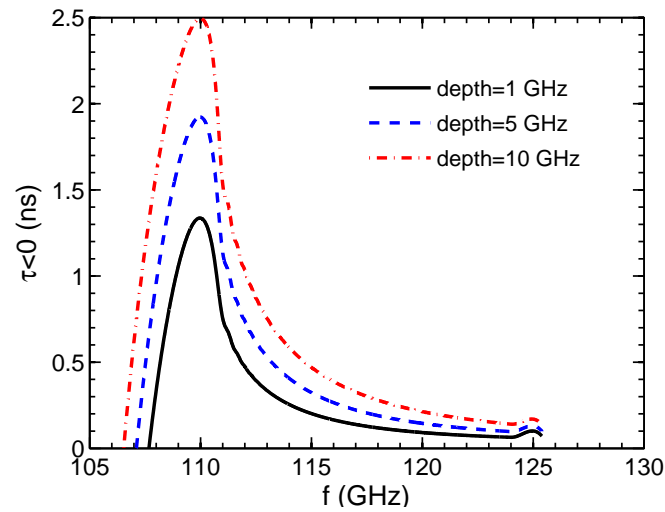


Fig. 4.25 Drop in time-of-flight from  $\text{sine}^2$  perturbations as introduced in Fig. 4.6, if subtracted by the smooth solution, starting when the signals with perturbation crosses the unperturbed solution.

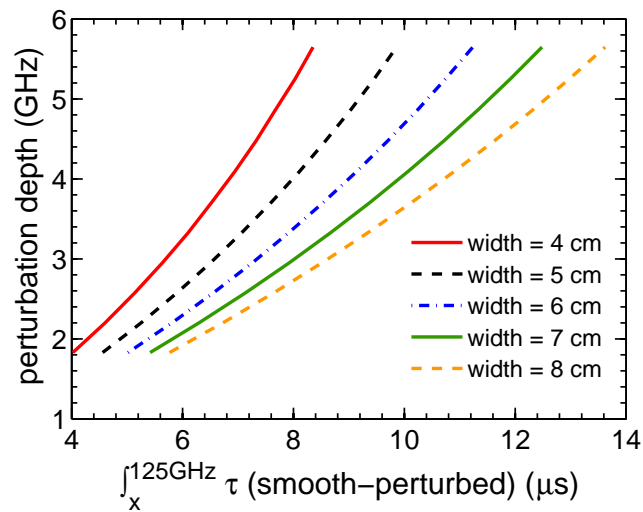


Fig. 4.26 Relations of hole depth to the integral of the time-of-flight difference between perturbed and unperturbed cases. The integral is computed from the probing frequency where the perturbed time-of-flight crosses the unperturbed case until 20 GHz above the frequency of the time-of-flight jump (in this case, 125 GHz).

These relations can be precisely fitted with polynomials of order two, with the parameters of the polynomials varying with the perturbation width. Such relations are enough to reconstruct the  $\text{sine}^2$  shaped valleys for the assumed fixed conditions. In

practice, however, this shape of the time-of-flight signal is too specific for this perturbation. To get insights towards a solution less reliant on the perturbation shape, the next section explores a combination of two perturbations, a positive perturbation followed by a negative perturbation. Turbulence vortices can typically introduce such perturbations where from mass conservation  $\langle \delta n_e \rangle = 0$ . The influence on the time-of-flight from each part of a composite perturbation is not always the same. The next section observes some examples and discuss how to proceed with the perturbation reconstruction on such cases.

## 4.8 Multiple perturbations

This section explores cases with multiple perturbations. More specifically, a bump followed by a valley. To start with simplified cases, the shapes are all assumed as  $\text{sine}^2$  again, and the width of the bump is the same as the valley. Just as before, the perturbations are added on a fixed linear  $f_R$  profile. At each width value, the bump part is kept constant and the valley depth varies. The objective is to observe how each perturbation influences the time-of-flight signal depending on the vertical distribution in the  $f_R$  profile. Perturbations with two width examples are given in Figs. 4.27 and 4.28. In both cases, the middle depth of the valley (green curve) has the same amplitude as the bump. This gives the same area in  $f_R$  space for both the unperturbed and perturbed cases, meaning a null radially averaged perturbation.

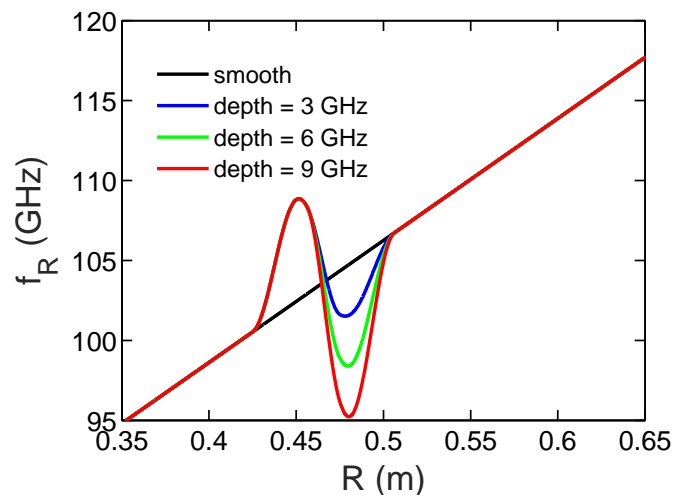


Fig. 4.27 9 cm long bump-valley perturbations added on a linear  $f_R$  profile. The valley has a varying depth while the bump is kept with a constant height of 6 GHz.

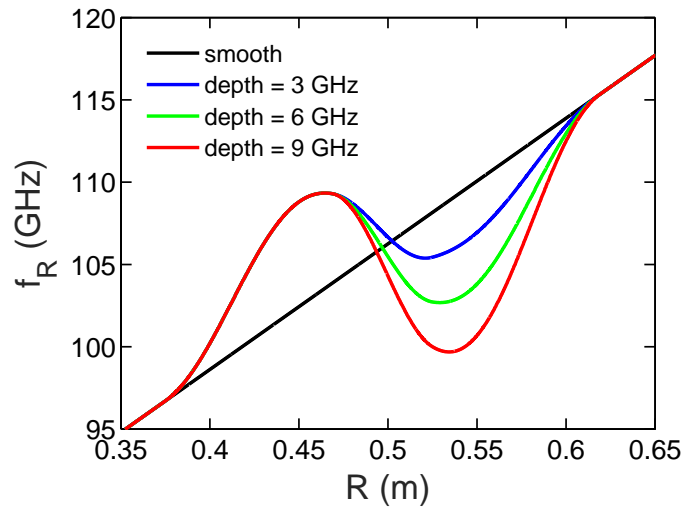


Fig. 4.28 25 cm long bump-valley perturbations added on a linear  $f_R$  profile. The valley has a varying depth while the bump is kept with a constant height of 6 GHz.

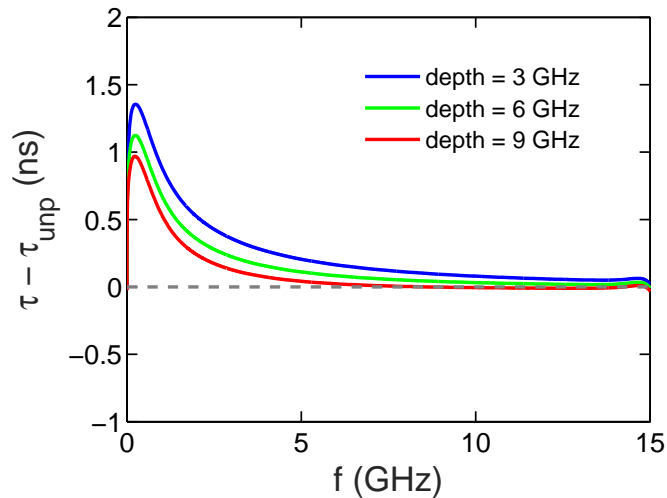


Fig. 4.29 The maximum of the IQ spectrogram time-of-flight signal when simulating the sweep on the profiles presented in Fig. 4.27.

The two examples in Figs. 4.27 and 4.28 were chosen as such because they show an uneven vertical distribution of the perturbation. On average, the bump lies on higher  $f_R$  values than the valleys. It is the exact opposite for a wide perturbation as in the examples in Fig. 4.28. This uneven vertical distribution is very significant for the time of flight signal after the perturbation. The physics interpretation is the same done for the perturbation kurtosis in Sec. 4.6.2. If the bump and the valley are evenly

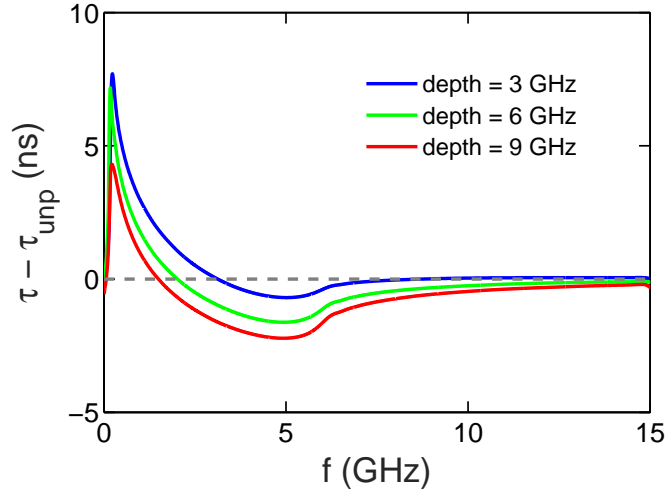


Fig. 4.30 The maximum of the IQ spectrogram time-of-flight signal when simulating the sweep on the profiles presented in Fig. 4.28.

distributed vertically in  $f_R$ , the time-of-flight signal after the jump quickly converges to the unperturbed solution if the bump height equals the valley depth. It is not the case for the examples in Fig. 4.27 and Fig. 4.28. The simulated time-of-flight signals, from the maximum of the IQ spectrogram, are found in Figs. 4.29 and 4.30.

The uneven vertical distribution of the perturbations in Figs. 4.27 and 4.28 are very evident from their respective time-of-flight signals in Figs. 4.29 and 4.30. In Fig. 4.29, there is always an excess in time-of-flight even when the valley has a smaller amplitude than the bump. The fact that the bump is higher in  $f_R$  than the valley makes it contribute much more to the time-of-flight signal in the higher frequencies. Exactly the contrary, if the perturbation is wider and the valley is much higher in  $f_R$  than the bump, it contributes more to the time-of-flight of the higher frequencies. Fig. 4.30 shows a case where the excess in time-of-flight after the perturbation is always negative even when the valley depth is smaller than the bump height. In the end, there is a distinct value of  $\nabla f_R$  for each perturbation width and depth that results in the exact condition where the contribution from the valley equals the contribution from the bump.

At this point there are two paths to follow to solve for the perturbation reconstruction method. One way is to continue with the same methodology of integrating the time-of-flight signal as presented in Sec. 4.7. To develop a reconstruction method in this direction, the value of the time-of-flight integrals would be very reliant on the composite perturbation shape. The number of solutions to be solved increase significantly, because all possible combinations between valleys and bumps must be solved. The other path to

follow, is to separate each perturbation and compute each contribution. In the end each contribution can be summed to generate the final signal. The bump part is possible to probe directly and therefore it is possible to compute its contribution on the composite perturbation signature. Then, subtracting the bump signature from the composite signal leads to a signal dependent only on the valley part to be analyzed. This methodology leads to many fewer cases to be solved and a much simpler implementation. In any case, the final reconstruction technique must take into account all the plasma parameters in the perturbation ( $f_{ce}$ ,  $f_{prob}$ ,  $\nabla f_R$ ) plus the perturbation geometry (depth, width, shape). The development of these solutions is performed in the next section.

## 4.9 A generalization of the reconstruction schemes

This section focuses on reviewing all features from the reconstruction methods of perturbations introduced earlier, and proposing a more general approach the reconstruction method of blind areas.

### 4.9.1 Review of the impact of full-wave effects on the reconstruction method

The hardest step into the generalization of the reconstruction method is solving for the perturbation shape, because it is not easily accessible. In theory, the full-wave features from the time-of-flight signal can contain information of the perturbations shape. The resonances, for example, indicate the valley width for the resonance frequency. However, not all resonances appear in the signal because the amplitude of each resonance is strongly bound to the quality factor of the cavity and the sweeping rate of the probing frequency. In addition, the interference pattern in the time-of-flight after the jump can also indicate features of the valley shape. The issue with this line of investigation is to extract these features from an experimental signal. The inherent noise levels in experimental signals hide this information. The information of the interference pattern is certainly destroyed by the experimental noise due to its dominantly low amplitude, and even if a resonance can emerge beyond the noise level, it is not possible to distinguish it from a possible noise spike. To acquire a statistically relevant data from the resonances, it would be necessary to probe the valley with each frequency for a long time. But at this pace the perturbation is not static anymore and the feature to be extracted is also not constant.

To avoid these overwhelming obstacles, the shape of the perturbation is firstly assumed known, or to be not very different from the assumed shape in a first order approximation.

If the probed perturbation shape can be estimated theoretically or by simulations, it can be used as input to refine the reconstruction scheme.

From the analyzes of the full-wave effects on the previous sections, the interference pattern can be fully neglected when taking the smoothed or filtered signal. The resonant peaks have little impact on the smooth time-of-flight signal, and they only appear in the vicinity of the jump. The tunneling effect is the harder effect to take into account because its bandwidth varies with the perturbation shape and size, although it is the only effect that can be observed in the smoothed signal, or the spectrogram maximum, instead of the instantaneous beat frequency. Thus, it is possible to observe it in an experimental signal. As illustrated in Fig. 4.12, the band is typically around 1 GHz. All full-wave effects are time-dependent effects. Therefore, the band in which they appear is also dependent on the probing sweeping rate. The values discussed were observed for a 20 GHz/ $\mu$ s sweeping rate, around the maximum sweeping rate used by the Tore Supra system. Summarizing, all full-wave effects can be ignored as long as the band of around  $\pm 1$  GHz around the jump in time-of-flight is not taken into account.

The perturbation depth can then be scaled to the time-of-flight over a large bandwidth instead of using localized features. This makes the reconstruction scheme more robust and reliable. In the point of view of generating the simulated signals, they are also in the validity domain of the WKB approximation.

The last feature to consider is related to the probing frequency at the end of the perturbation. In the cases that the time-of-flight signal converges back to the unperturbed solution after the valley, the probing beam still probes part of the valley after the jump. In such cases, there is a valley in the time-of-flight perturbation signature with the valley minimum marking the probing frequency at exactly the end of the perturbation. This feature is quite evident in most cases, as, e.g., in Fig. 4.6. After this minimum, the time-of-flight is always below the unperturbed signal for a valley perturbation, and above for a bump perturbation. The most general way to treat the signal of any given perturbation is to exploit this excess time-of-flight signal after this end mark. The two cases that can be out of the scope of this approach are: 1) the perturbation is too wide and the end frequency is so high that the excess time-of-flight from the perturbation has depleted; and 2) the perturbed signal does not converge back to the unperturbed case. In both cases, the perturbation excess time-of-flight is still present in the signal, only the unperturbed solution that is not anymore just a smooth continuation of the signal trend. The excess signal can still be extracted if the slope after the jump changes, as in the first case. Only the range has to be before the end of the perturbation. And it is the same as for the second case, where there would be a shift in the signal evolution. These

cases have a less reliable estimation of the unperturbed signal, but these estimations can be complemented by observing the evolution of the  $f_R$  profile along different sweeps. These explanations cover all perturbation shapes for the definition of the end of the perturbation. Either there is no visible end mark, then the end is considered just after the jump, or the end is marked by the minimum in the time-of-flight valley. In either cases, the perturbation width can now be determined from the reconstructed profile with the estimated unperturbed signal and the end probing frequency value.

Having discussed in this section the possibilities for the perturbation shape, the WKB valid scaling intervals of the time-of-flight signal, and lastly, the different cases of determining the perturbation width from the perturbation end mark, the following discussion focuses on the signal to be scaled to the plasma parameters. Similarly to the physics discussed in Sec. 4.6.2, the perturbation signature nearly disappears after around 15 GHz of its end probing frequency. Therefore, the reconstruction method can take into account this probing frequency range: from 1 to 15 GHz after the probing frequency at the end of the perturbation. If the perturbed signal is subtracted of the unperturbed signal, the signal left is originated solely from the perturbation introduced. This excess signal can then be scaled to the perturbation depth, i.e. the last and main feature to be estimated. This approach can isolate the perturbation signal regardless of the parameters in the probing zone  $(f_{prob}, f_{ce}, \nabla f_R)$ .

The greatest advantage of having a database of the perturbation signals as it was defined, is the flexibility it brings. E.g., it is much simpler to solve the multiple perturbation cases illustrated in Sec. 4.8 if the contribution in each perturbation is isolated and treated separately. Since the bump perturbation can still be probed, its contribution in the time-of-flight signal can be quickly computed numerically. By adding the bump contribution to the unperturbed signal, the excess time-of-flight is only originated from the valley contribution. Separating a composite signal in this way makes it possible to analyze each perturbation separately, regardless of the complexity of the combined signal. Each perturbation has its own end frequency and when summed shifted in frequency from each other, arrive at the complex shapes illustrated in Figs. 4.29 and 4.30. In some cases it's not even possible to intuitively deduce if the combined  $\delta f_R$  is positive or negative. The database approach on isolated perturbations can easily handle such complex cases.

The approach of creating a database of solutions is similar to developing a neural network to invert the perturbation signals, as it has been done for inverting the density profile [77]. The main difference is that when creating the database, the user has full

control of the input parameters and the output accuracy can be precisely verified, allowing for a more precise determination of the error bars around the solution found.

### 4.9.2 Database of time-of-flight signals from sine shaped valleys

Every time the probing beam crosses a perturbation, the time-of-flight signal of the following probing frequencies will carry information of the perturbation in addition to the information of the profile being probed after the perturbation. If the signal is observed subtracted of the unperturbed signal, the information left is only originating from the perturbation. This is true regardless of the local plasma parameters. Based on this principle, a database of perturbation signals can be computed for an assumed shape. For easy of implementation, the initial shape is assumed as a half period of a sine function. As explained in the previous section, the perturbation signal is evaluated avoiding the full-wave effects. This means that these solutions in the database can be computed under the WKB approximation. The signals stored are the time-of-flight in the range of 1 to 15 GHz in probing frequency above the frequency of the perturbation end point, bypassing the full-wave effects affecting the time-of-flight signal for a sweeping rate of 20 GHz/ $\mu$ s or slower. The signal is computed from the derivative of the WKB phase calculated by Eq. 3.5, generated exclusively from the perturbation area. This signal is then recomputed for a broad range of conditions in the five dimensional space of the parameters ( $f_{end}, f_{ce}, \nabla f_R, \text{width}, \text{depth}$ ). The  $f_{end}$  parameter is the probing frequency at exactly the end of the perturbation,  $f_{ce}$  is the constant  $f_{ce}$  value inside the perturbation,  $\nabla f_R$  is the  $f_R$  gradient of the equivalent unperturbed profile, and width and depth are the geometrical features of the perturbation. The perturbations are treated in the  $f_R$  space to account for the magnetic field dependency, and are added on constant  $\nabla f_R$  profiles, analogous to the study cases introduced in Fig. 4.5.

The range of the five parameters was chosen to cover all tokamaks range of density and magnetic field (from small tokamaks to ITER) and include both X and O mode polarizations. Both polarizations are covered due to the compatible minimum values in probing frequencies and magnetic field. A table containing a list of all boundary conditions used can be found in table 4.1.

Fig. 4.31 shows an example of the signal stored in the database for a fixed set of parameters ( $f_{end}, f_{ce}, \nabla f_R, \text{width}$ ). Given the experimental signal from probing a perturbation, it can be compared to the database of signals and the signal with the best match will indicate the perturbation depth.

When computing the database of solutions, all parameters are swept with the same discretization and boundary conditions as specified in 4.1. This means that the order

Table 4.1 Boundary conditions of all parameters in the database of sine valley perturbations.

parameter	minimum value	maximum value
$f_{end}$	25 GHz	250 GHz
$f_{ce}$	0	250 GHz
$\nabla f_R$	0	250GHz/m
width	0.02 m	0.4 m
depth	1 GHz	30 GHz

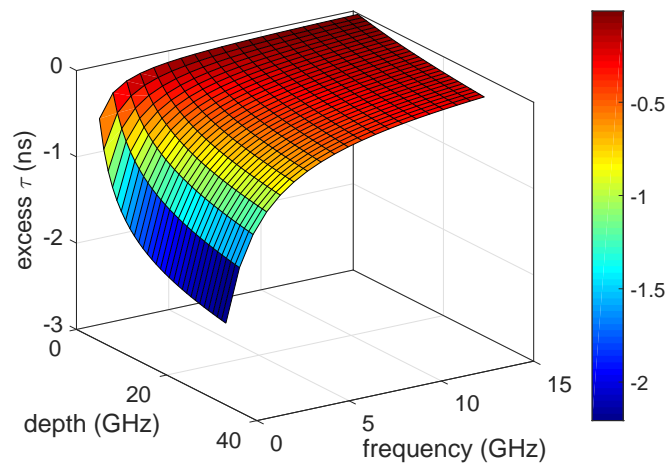


Fig. 4.31 Example solution of database of time-of-flight excess signals for sine shape valleys in the fixed conditions of  $width = 2cm$ ,  $f_{end} = 126.2GHz$ ,  $f_{ce} = 12.5GHz$ ,  $\nabla f_R = 118GHz/m$ .

of the parameters are interchangeable and can be explored graphically, as displayed in Fig. 4.31, for any of the parameters as a variable. Computing the database in this way also results in some cases that are unphysical because the perturbation in  $f_R$  goes below the value of  $f_{ce}$ . These cases have only a NaN (Not a Number) instead of a signal. The validity of possible solutions is easily verified if checking for NaN entries. Fig. 4.32 shows a validity map for the perturbation geometry for an example of fixed conditions in all other parameters.

After explaining the development process of the database in this section, the next step is to demonstrate its operation on a synthetic case in the next section. Then, the accuracy of the reconstruction is determined against all possible error sources and experimental noise in Sec. 4.9.4.

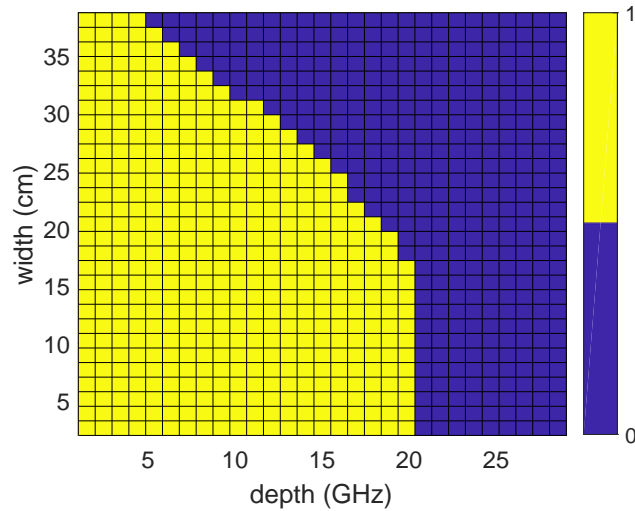


Fig. 4.32 Example of validity domain in database solutions for the fixed parameters of  $f_{end} = 70GHz$ ,  $f_{ce} = 37.3GHz$  and  $\nabla f_R = 118GHz/m$ . The valid solutions are numbered with the number one and displayed with the color yellow.

### 4.9.3 Example of reconstruction using the database on a synthetic case

One example of a perturbation reconstruction using the database of sine valleys as described in Sec. 4.9.2 is displayed in Fig. 4.33. The parameters represent a tokamak relevant case with low magnetic field. In this case, the perturbation signal is a synthetic signal computed under the WKB approximation. The accuracy in the depth estimation is better than 1%. The accuracy of the reconstruction method itself is practically negligible compared to the error coming from the experimental signals. The next subsection analyses the error in the perturbation reconstruction based on the magnitude of the time-of-flight signals in the database.

### 4.9.4 Analysis of reconstruction accuracy

The accuracy of the reconstruction of a perturbation using the database could be displayed using a few example reconstructions with added noise. However, no matter how many examples are used, this methodology is not exhaustive and does not prove the reconstruction accuracy for any possible condition. Instead, the accuracy dependency on the full range of all parameters can be observed by carefully analyzing the signals in the database.

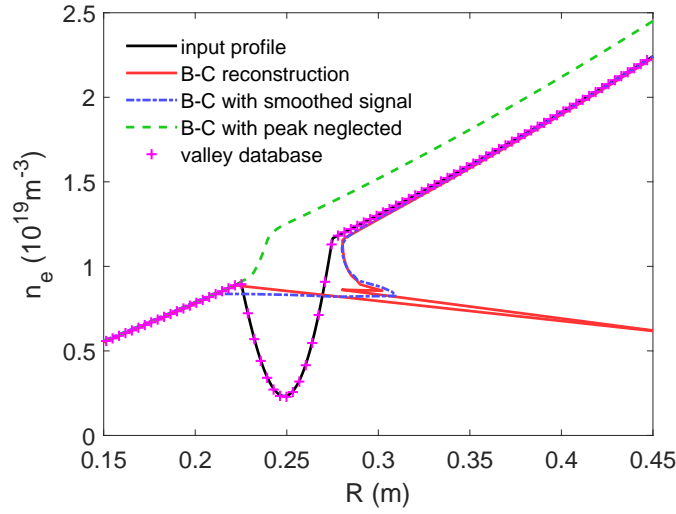


Fig. 4.33 Example of traditional reconstructions (Bottollier-Curtet algorithm) and a perturbation reconstruction using the computed database of sine valleys. The parameters in the perturbation are  $width = 5cm$ ,  $f_{end} = 62.3GHz$ ,  $f_{ce} = 47.2GHz$  and  $\nabla f_R = 70GHz/m$ .

The two important aspects to consider are: first, the available length in frequency of the signal to be analyzed; and second, the variation in the magnitude of the time-of-flight signature in the given conditions. In fact, both aspects are strongly linked as will be demonstrated below.

Focusing on the first aspect (the length of available frequency data), the longer the signal, the easier it is to restrain the perturbation signal to a solution in the database. In addition, the additional time-of-flight from the perturbation is very small at 15 GHz after the jump. Therefore, the end point of the signal is almost fixed, while the first frequencies vary strongly with the change in the perturbation depth, as can be observed in Fig. 4.31.

The second aspect, is on the variation of the magnitude of the time-of-flight signals. It is clear that, for a given fixed noise level, the greater is the variation in the signal's area when scanning the possible depths, the more accurate it is to determine which is the depth corresponding to the perturbation measured. Since the end frequency is nearly fixed, it is already clear that the first frequencies after the time-of-flight jump offer the best depth resolution. This feature can be quantitatively demonstrated by calculating the integral of the excess time-of-flight signals in the database in a few cases. Fig. 4.34 shows two very different cases in terms of the integral of the time-of-flight signal. To illustrate the impact of the first aspect mentioned (the range of frequency in the signal),

three example ranges are displayed in each case. They were divided as the second half of the frequency range, then the first half, and lastly, the full range. In any condition, the first frequencies will offer faster change in the integral value, as already pointed out. The different cases chosen show an order of magnitude difference between them in the magnitude of the integral of the time-of-flight signal. The same follows for the slope of these curves.

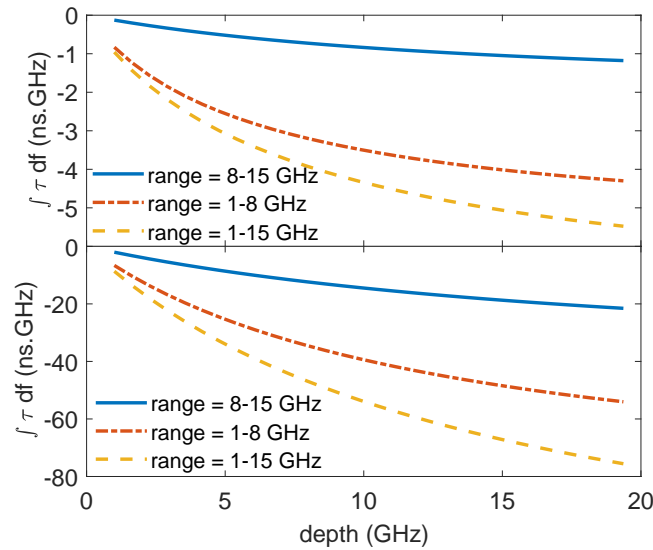


Fig. 4.34 Different ranges in the time-of-flight integration for two solution conditions. Top case with  $width = 2cm$ ,  $f_{end} = 47.5GHz$ ,  $f_{ce} = 24.9GHz$  and  $\nabla f_R = 106GHz/m$ . Bottom case with  $width = 9.7cm$ ,  $f_{end} = 227.5GHz$ ,  $f_{ce} = 199GHz$  and  $\nabla f_R = 106GHz/m$ .

In summary, both the perturbation parameters and the available signal range strongly affect the accuracy on the depth estimation. It is important to have this feature in mind specially in combined perturbations. In such cases, often the end of the valley is not directly probed, resulting in part of the signal not being used for the depth estimation, thus reducing the estimation accuracy as observed in Fig. 4.34. When comparing the experimental signal to the database, the user selects the confidence range in the area of the experimental signal. With this range for the signal's area and the corresponding database curve, as exemplified in Fig. 4.34, the variation encountered in the depth value results in the error bars of the estimated depth.

The interpretation of Fig. 4.34 showed the importance of the available frequency band and the local plasma parameters for the accuracy of the reconstruction. The next step is to demonstrate the integral behavior, considering the full 1 - 15 GHz band, over the full range of all database parameters. The first parameters to be observed are the geometrical

features: *depth* and *width*. Only for one case of all other fixed parameters, Fig. 4.35 shows the strong dependency over the perturbation geometry. Very intuitively, the bigger the valley, the bigger is the value of the integrated signal. The *width* is normally fixed, then the curve in *depth* is observed. The wider is the perturbation, the more emphasized is the change in the slope along *depth*. At this point, it is straight forward to understand the picture in Fig. 4.35, but the integral of time-of-flight is not yet directly the obtained accuracy one to one. The quantity that gives directly the obtainable accuracy is the derivative of the integral as a function of the depth, mathematically defined as:

$$accuracy(d_v) = \left| \frac{\partial}{\partial d_v} \int \tau df_{prob} \right| [ns], \quad (4.6)$$

where  $d_v$  denotes the valley depth in GHz. The quantity *accuracy* is interpreted as the change in the area of the time-of-flight's signal integrated over one GHz in  $f_{prob}$  resulting in a change in depth of one GHz. The higher is the variation in the time-of-flight area that is necessary to change one GHz in depth, the more resolution is available to estimate the depth for a fixed noise level.

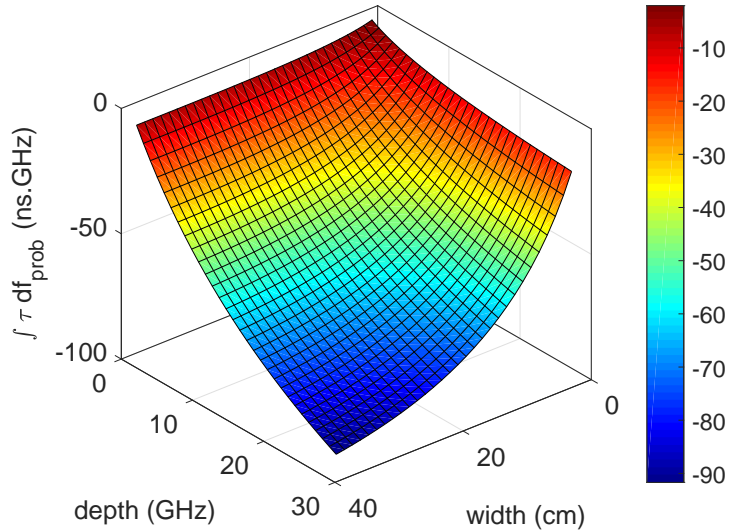


Fig. 4.35 Integral of time-of-flight signals in database for the fixed parameters of  $f_{end} = 167GHz$ ,  $f_{ce} = 91GHz$  and  $\nabla f_R = 82GHz/m$ , showing dependency on depth versus width.

Fig. 4.36 shows a direct illustration of the accuracy, calculated according to Eq. 4.6, in the database in respect to the different geometrical aspects of the perturbation (depth

and width). The result is that the wider is the perturbation, the more accurate is the depth estimation, for a given fixed noise level.

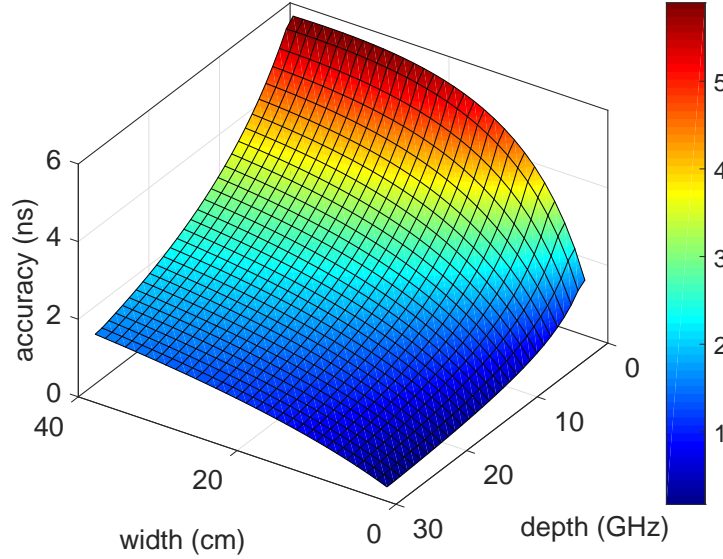


Fig. 4.36 Reconstruction accuracy computed according to Eq. 4.6. All other parameters are fixed at  $f_{end} = 167GHz$ ,  $f_{ce} = 91GHz$  and  $\nabla f_R = 82GHz/m$ . The accuracy is displayed versus the geometrical parameters depth and width.

The next parameters observed, again for a fixed value on all other parameters, are the  $f_{ce}$  and  $\nabla f_R$ . It was possible to interpret the geometrical dependency in Fig. 4.35 because all available depths are shown. However, to investigate the behavior over the other parameters, the accuracy can be averaged over all the depth range. The averaged accuracy is plotted for a case with a narrow perturbation in Fig. 4.37, and a wide perturbation in Fig. 4.38.

Any lack of range in the parameters displayed compared to the values presented in table 4.1 is due to an unphysical domain. As it was exemplified in Fig. 4.32, the unphysical cases are marked with NaN, and these cases are not displayed in the surfaces of Fig. 4.37, 4.38 and 4.39.

The change in respect to the parameter  $\nabla f_R$  is nearly negligible for the narrow perturbations, but rather significant for the wide perturbations. It is clear that the wider is the valley, the more it is affected by the change of gradient. As initially discussed in Sec. 4.6.2, the higher frequency part of the valley has the highest influence on the time-of-flight. In high gradient cases, it means that the top frequencies in the beginning of the valley are much lower in frequency, thus, having little impact on the probing frequencies above the valley. Therefore, it explains why the low gradient part in Fig. 4.38

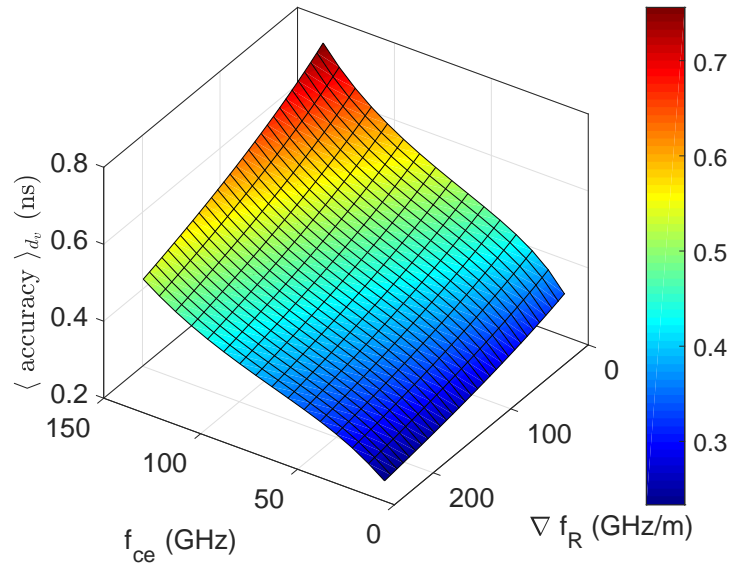


Fig. 4.37 Accuracy as given in Eq. 4.6, averaged over all depths  $d_v$ , for the fixed parameters of  $f_{end} = 197\text{GHz}$ ,  $width = 2\text{cm}$ , showing dependency on  $f_{ce}$  versus  $\nabla f_R$ .

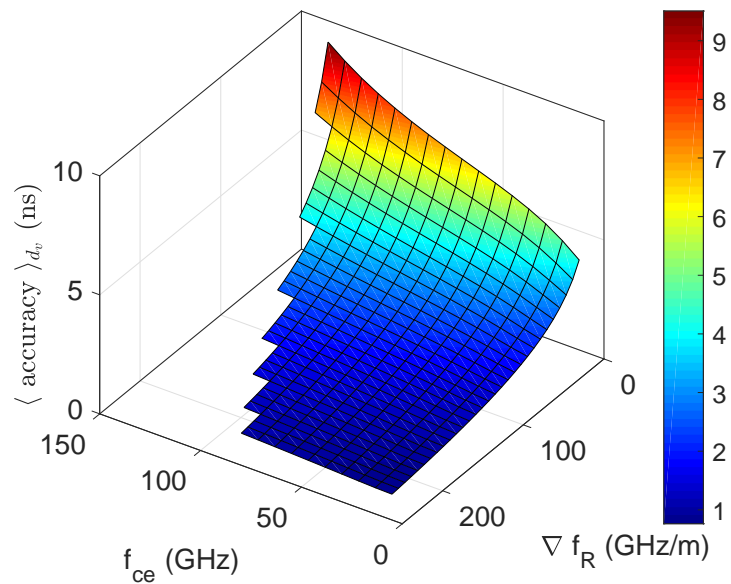


Fig. 4.38 Accuracy as given in Eq. 4.6, averaged over all depths  $d_v$ , for the fixed parameters of  $f_{end} = 197\text{GHz}$  and  $width = 32\text{cm}$ , showing the dependencies on  $f_{ce}$  versus  $\nabla f_R$ .

have a much lower value for  $\langle \text{accuracy} \rangle_{d_v}$ , a feature that is negligible in the narrow case of Fig. 4.37. A straight comparison of the magnitude of  $\langle \text{accuracy} \rangle_{d_v}$  between Figs. 4.37

and 4.38 directly shows how the wider case can have around ten times more accuracy on the reconstruction in the low gradient range.

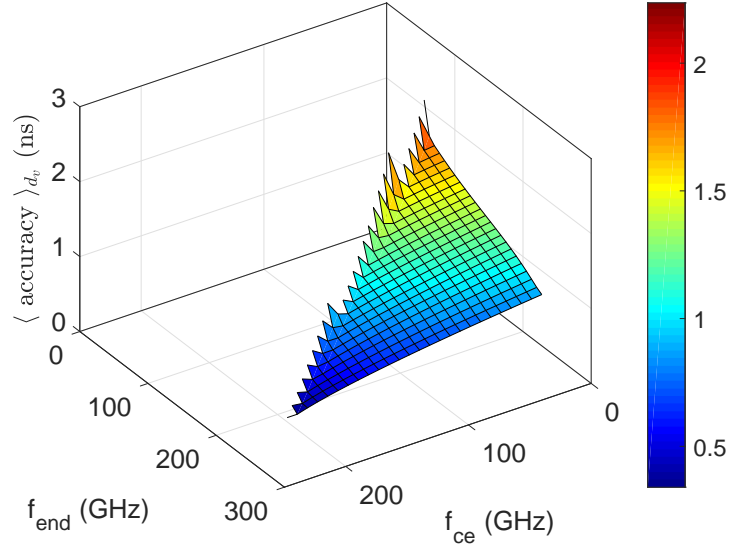


Fig. 4.39 Accuracy as given in Eq. 4.6, averaged over all depths  $d_v$ , for the fixed parameters of  $\nabla f_R = 34 \text{GHz/m}$  and  $width = 16 \text{cm}$ , showing the dependencies on  $f_{end}$  versus  $f_{ce}$ .

The last parameter to observe is the probing frequency at the end of the valley,  $f_{end}$ , and  $f_{ce}$ , as plotted in Fig. 4.39. A striking feature in this case is the obvious boundary conditions at the boundary where  $f_{ce}$  approaches  $f_{end}$ . Like mentioned before, and illustrated in Fig. 4.32, the perturbation profile in  $f_R$  can never go below the value set for  $f_{ce}$ . Therefore, the closer  $f_{ce}$  gets to  $f_{end}$ , the smaller becomes the range available for the valley depth, until no perturbations of any geometry are allowed. Very close to the boundary, the surface starts to dip, unlike the average trend. This effect is due to the deeper range being unavailable, thus the average accuracy over depth only accounts for the shallower depths, resulting in a slight change in the obtained accuracy.

In summary, the accuracy was observed to increase with increasing width and decreasing depth. The dependency over  $f_{ce}$  is almost negligible compared to the other parameters. The accuracy increases with decreasing  $\nabla f_R$ , and it is quite emphasized at wider perturbations. The last parameter,  $f_{end}$ , showed greater accuracy for lower frequencies.

The previous analyzes allowed to understand how the reconstruction accuracy will vary for any value of all parameters, given a time-of-flight signal with constant noise level. In addition to the noise level encountered in the time-of-flight signal, the parameter

$f_{ce}$  is also susceptible to experimental noise. In order to verify the error in the depth estimation from errors in  $f_{ce}$ , the integrated time-of-flight can be analyzed again versus the parameter  $f_{ce}$ , as presented in Fig. 4.40.

The process to determine the error in depth from the error in  $f_{ce}$  can be explained as follows. An error in  $f_{ce}$  means that the time-of-flight integral, i.e. the surface in Fig. 4.40, is kept constant while changing  $f_{ce}$ . Then, for the new value in  $f_{ce}$ , all that is left is to find the depth corresponding to the same area as before. In other words, it is the gradient in the *depth* axis of the surface in Fig. 4.40 in the direction following a constant value in the  $z$  direction. As the surface in Fig. 4.40 is quite smooth against small changes in  $f_{ce}$ , it is a very accurate approximation to assume that the depth error has a linear dependency on the  $f_{ce}$  error. The result of the calculation described, when applying a 1 GHz error in  $f_{ce}$ , is depicted in Fig. 4.41 as a percentage error in the perturbation depth. As the dependency on the  $f_{ce}$  error is linear, an observable error can be multiplied by the result displayed in Fig. 4.41 to arrive at the specific error encountered.

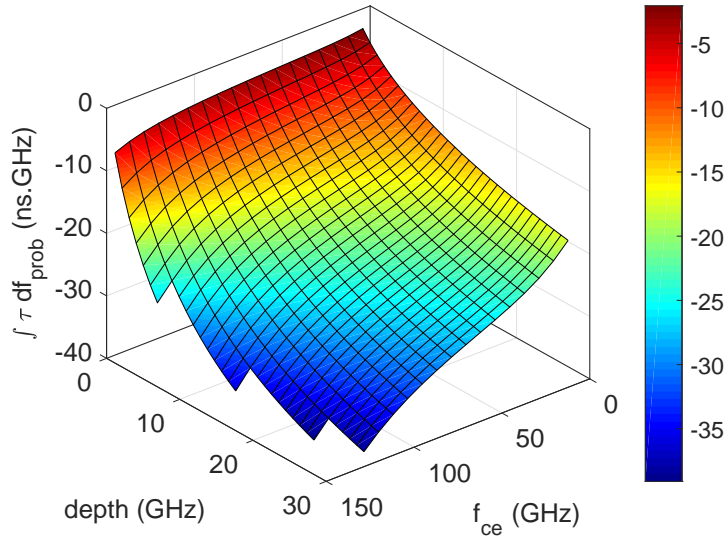


Fig. 4.40 Surface of integrated time-of-flight showing the impact in *depth* related to  $f_{ce}$ . The remaining parameters are kept constant, with  $width = 4.5\text{cm}$ ,  $f_{end} = 160\text{GHz}$  and  $\nabla f_R = 82\text{GHz}/\text{m}$ .

The error values displayed in Fig. 4.41 were also verified to not change from this order of magnitude for any different values of the fixed parameters  $width$ ,  $f_{end}$  and  $\nabla f_R$ .

This section showed an error analysis over the range of parameters solved in the database. Although the different accuracy regions were mapped, no peculiar regions were found with greatly enhanced reconstruction error for the perturbations. Even

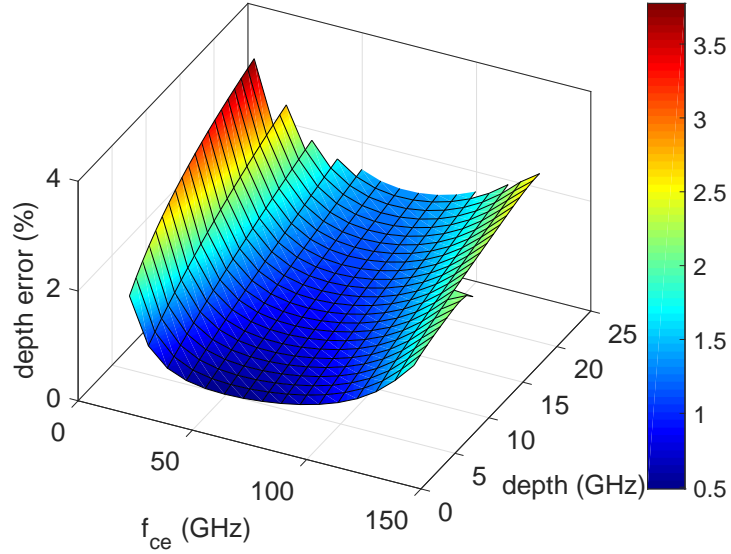


Fig. 4.41 Error in estimated perturbation depth for a 1 GHz error in  $f_{ce}$ . The remaining parameters are kept constant, with  $width = 4.5cm$ ,  $f_{end} = 160GHz$  and  $\nabla f_R = 82GHz/m$ .

though the demonstration of a perturbation reconstruction on experimental data is still necessary, these analyses guarantee that the observable accuracies will not drastically change for different parameters, and no exhaustive demonstration is necessary over countless parameter sets.

## 4.10 Conclusions and future prospects

The reconstruction of blind regions in frequency swept reflectometry has never been tackled before. As it was demonstrated, the standard reconstruction process add a significant error in the density profile if no special technique is applied around the perturbed region. The work performed here investigated more general characteristics to lay the foundations for this vast area of study. Further on, more detailed study is foreseen focusing in the reflectometer signal response from complex 3D geometrical aspects and on the shape assumed for the perturbation.

Even though the main physical characteristics of the blind regions have been well described by the 1D simulations present in this contribution, 3D simulations are necessary to verify any additional geometrical aspects. After all, the probing beam area and shape, plus the shape of the perturbations, make in conjunction a system too complex to be completely described in one dimension. The geometrical aspects also heavily influence

the amplitude evolution, which is a topic to be further investigated in the case of blind regions and specially for the initialization technique, as it is discussed in the next section.

As a first approximation, the valleys were assumed as having a sine shape. If any other shape is of interest, the database can be recomputed for that specific shape. In the end, a few different shapes can be available if the situation indicates for the preference of a specific shape over the others. Future studies including 3D simulations or a previous knowledge of the perturbation shape being studied can dictate which shape to be used in the database for a more accurate estimation of the perturbation depth.

The error in the perturbation reconstruction caused by noise in the time-of-flight and  $f_{ce}$  signals was described in Sec. 4.9.4 for all the range of parameters covered. No parameter regions were found with extraordinarily enhanced error. The possible additional sources of error are the assumptions made on the unperturbed profile gradient, the perturbation width, and the perturbation shape. The assumptions on the unperturbed profile gradient and the width of the perturbation will vary according to each application. In the cases where data is available for a clear and well-behaved evolution of the profile, these assumptions are straight forward and accurate. If there is available only a single sweep and the profile include high amplitude low  $k$  perturbations, these assumptions will not be accurate. As a future prospect, the assumption on the estimated shape can be corroborated with theoretical predictions or numerical simulations of the perturbations being studied.

The implementation of the reconstruction of complex perturbations add significant complexity to the profile reconstruction, as it was seen throughout this chapter. However, the perturbation signal was covered in nearly full extent. Due to this characteristic, any simplified reconstruction method that can still be satisfactorily used, can be easily derived from the generalized solution presented. An example of such a simplified method is to use of a small set of frequencies instead of fitting a broad band of probing frequencies, or even only using the integral of the excess time-of-flight.

The full-wave effects displayed have been avoided in the technique to reconstruct the blind regions. The observed full-wave effects rarely have enough amplitude to be distinguishable in a noisy experimental signal. The reliable extraction of information from these effects will only be possible when further developments in the hardware front are achieved. Furthermore, the amplitude of these effects can still be strongly linked to the 3D geometrical aspects that need to be investigated in 3D full-wave simulations.

Even though further investigation is foreseen on the 3D geometrical aspects and perturbation shapes as described above, the 1D sine shape database developed here will

be first applied in experimental cases in the near future to demonstrate the viability of this approach to determine the density profile inside the blind areas.

The first experimental application on the results developed in this chapter were demonstrated for the first time in data from the Tore Supra database. This work was performed after the manuscript deposition and therefore it is included in Appendix [B](#).

# Chapter 5

## Issues and new improvements on the determination of the first cut-off position

The third topic explored to improve the density profile reconstruction is the determination of the first cut-off position, or commonly referred to as the initialization of the profile reconstruction. It is a very crucial point in the profile reconstruction, but it is treated last because some of the experience and knowledge acquired before can be used here.

The first step taken was to benchmark the errors introduced in the reconstructed profile due to various possible errors in the initialization. Not only it serves as a benchmark for the error expected, but also, to reveal what are the significant error causes and their influence mechanisms.

After covering the benchmarking of all error sources, full-wave simulations are performed in Sec. 5.2 to investigate some aspects on the technique to initialize the profile reconstruction. A previous work [78] has used 1D full-wave simulations to determine the position of  $f_{prob} = f_{ce}$  for linear density profiles of varying gradient. The new aspect explored here is devoted to the diverging aspects between the WKB phase and the full-wave phase focused on the profile reconstruction, instead of the technique to determine the first position. The reason being because the profile reconstruction algorithm uses the WKB estimate for the phase in order to reconstruct the density profile. Any divergence should be taken into account in order to optimize the accuracy of the reconstruction algorithm. This aspect will also be present in Sec. 5.3 when exploring initialization cases with introduced perturbations in the vicinity of the first reflected frequency. Moreover, such perturbations in the edge can get detached from the main density profile. These cases can degrade the correct initialization or provide a false initialization position,

as shown in Sec. 5.3. The signature of these objects has to be identified to improve the initialization technique and avoid false initializations. When these events are well described, a reconstruction method similar to the one developed in the previous section can be used to provide the object's properties.

## 5.1 Benchmarks of the initialization error

The accuracy of all calculations in reflectometry is affected by the hardware precision. The sweep of probing frequency is assumed linear and the probing frequencies are assumed well known. If any irregularity in these assumptions is observed, a dedicated benchmarking can be performed for those specific irregularities detected. In the scope of this thesis, it is assumed that the probing frequencies are well known and accurate. Apart from possible hardware irregularities and the unavoidable inherent noise of the experimental signals, the possible additional physical sources of error introduced when determining the first cut-off can be divided in three categories: 1) the density on the first cut-off position is not negligible as normally assumed; 2) the error in the input magnetic field profile; and 3) ignoring some plasma that exists before the first assumed cut-off. These three error sources are each respectively explored in the next subsections.

All cases tested and presented below have been tested with various frequency step size in the reconstruction. Although there is a difference in the resulting error profile, this effect is only visible in the low gradient sections, and its magnitude is so small that it is below the noise level of any experimental signal.

In this section, the synthetic phase signals are computed using the WKB approximation. The WKB approximation is valid in this case because there are no full-wave effects present from perturbations in the probed profile. The technique to identify the first cutoff frequency is prone to full-wave effects, but a mistake in this step is exactly one of causes that lead to the errors introduced.

All cases treated in this section are based on the typical Tore Supra discharge, as also introduced in Chap. 3, with a pedestal present around the position of 0.2 m. The corresponding frequency profiles are depicted in Fig. 5.1. The density profiles are reconstructed using the optimized reconstruction algorithm presented in Chap. 3.

### 5.1.1 Shifts from errors in the starting density value

Following the order of error sources announced in the introduction, this section treats the first case: the assumed density in the first cut-off position, i.e.  $n_{e0}$ . To investigate

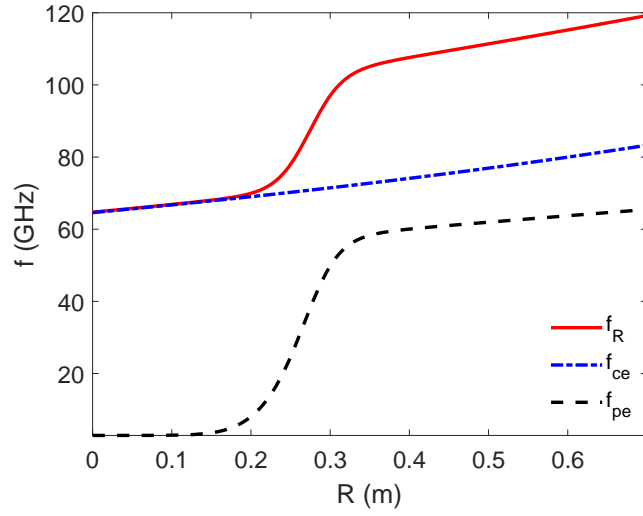


Fig. 5.1 Frequency profiles used as a base case for the benchmarks in Sec. 5.1. The density and magnetic field have magnitudes typical of Tore Supra discharges with a pedestal located around 0.2 m.

this issue, the base density profile introduced in Fig. 5.1 is added of a constant initial density, ranging from  $10^{16}m^{-3}$  to  $5 \times 10^{17}m^{-3}$ . The corresponding density profiles are depicted in Fig. 5.2, only displaying the edge region.

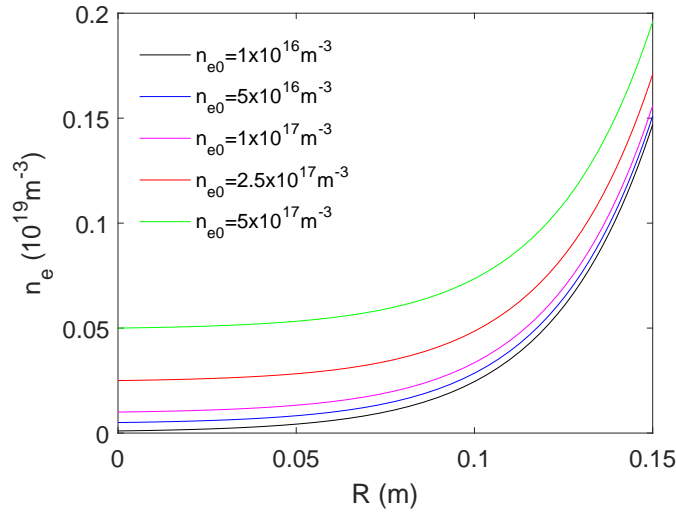


Fig. 5.2 Edge region of density profiles assumed to investigate the initialization error when the initial  $n_e$  is not negligible.

The first reconstruction position is calculated based on the assumption that at the first reflection, the density is negligible. If the density at the first cut-off is not negligible, the assumption that  $f_{prob} = f_{ce}$  becomes false. The corresponding initialization error from breaking the assumption that  $f_{prob} = f_{ce}$  can be directly observed on the dashed lines in Fig. 5.3. These dashed lines represent the radial distance between the upper X-mode cut-off profile,  $f_R$ , and the electron cyclotron frequency profile,  $f_{ce}$ , at the position of the first cut-off. In this case they also correspond to the maximum value of the profile of error. The complete error profile in the profile reconstruction from the error in the assumption  $f_{prob} = f_{ce}$  is depicted in Fig. 5.3 for various values of  $n_{e0}$ .

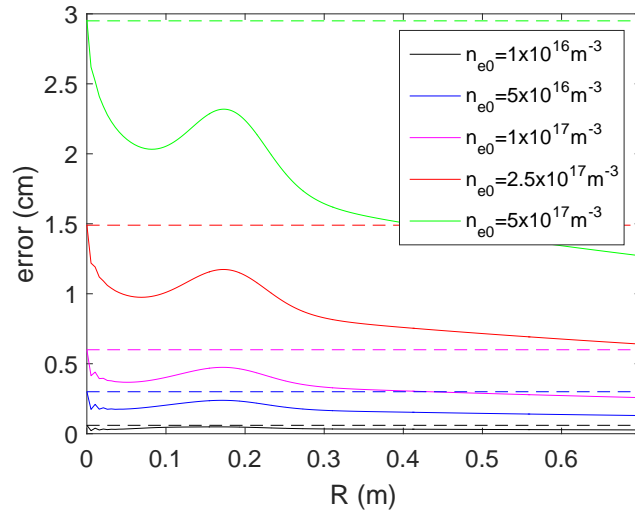


Fig. 5.3 Error profile when reconstructing the density profile using the optimized scheme of Chap. 3 with varying values in starting density,  $n_{e0}$ . The dashed lines represent the distance between  $f_R$  and  $f_{ce}$  for the probing frequency considered as the initialization point.

The shape of the error profile doesn't change significantly from each case, thus does not show any particular feature. The dashed lines, on the other hand, serve as a good guide of the error profile, exposing the main cause of error, i.e. the distance between the  $f_R$  and  $f_{ce}$  profiles at the initialization point. From Fig. 5.3, as the initial density increases, the distance between  $f_R(R_0)$  and  $f_{ce}(R_0)$  increases, together with the reconstruction error profile. For this error source, the error introduced decreases when moving to the plasma core, but the order of magnitude of the error initially introduced remains the same.

### 5.1.2 Shifts from neglecting shallow plasma

If there is enough plasma before the first assumed cut-off, there will be an additional phase related to this plasma ignored. Obviously, the longer and denser the plasma is, the greater is its influence. Two extents were tested, 1 cm and 12 cm, with various values of a constant density for the shallow plasma neglected. The density profiles were slightly modified for this purpose. The edge shallow plasma was set with constant density. To accommodate the shallow plasmas, the pedestal has moved slightly inwards. The resulting density profiles used are depicted in Fig. 5.4.

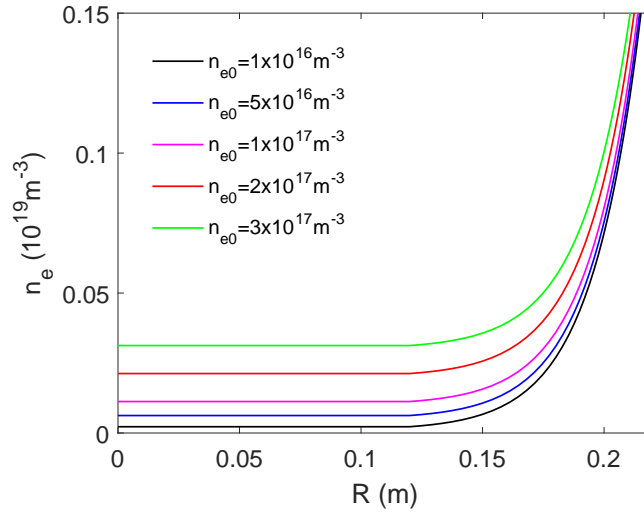


Fig. 5.4 Edge region of density profiles assumed to investigate the initialization error when a given radius of a shallow plasma of constant density is neglect.

The results after the profile reconstruction on the input cases displayed in Fig. 5.4 can be found in Figs. 5.5 and 5.6, for the 1 cm and 12 cm of edge plasma neglected, respectively. The 1 cm value was chosen as a typical case that is routinely expected, and the 12 cm case, to observe what happens in an exceptionally bad case. Again, the distance between the upper X-mode cut-off profile,  $f_R$ , and the electron cyclotron frequency profile,  $f_{ce}$ , at the position of the first cut-off is marked with the respective dashed line.

Although neglecting some plasma that exists before the initialization have an impact on the reconstructed profile error, it is of a higher order compared to the error associated to the assumption of  $f_{prob} = f_{ce}$  at the first cut-off frequency. This conclusion is evident from observing the dashed lines in Figs. 5.5 and 5.6. The error profiles exhibit higher values when neglecting a longer plasma, but always follow relatively close to the dashed

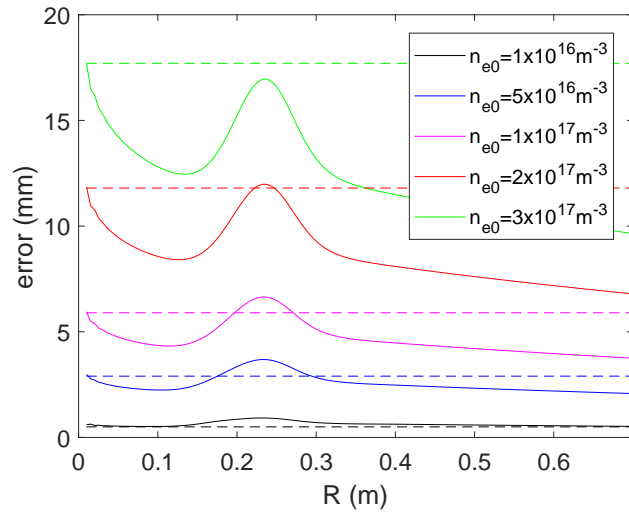


Fig. 5.5 Error profile when reconstructing the density profile using the optimized scheme of Chap. 3 while skipping a shallow plasma 1 cm long with varying values of a constant density. The dashed lines represent the distance between  $f_R$  and  $f_{ce}$  for the initial probing frequency.

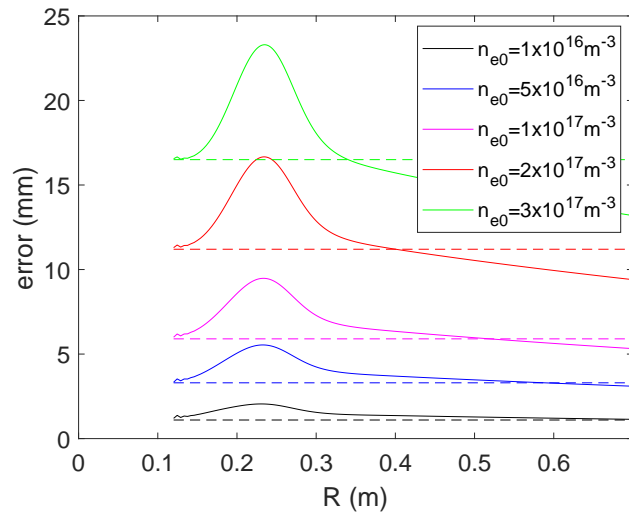


Fig. 5.6 Error profile when reconstructing the density profile using the optimized scheme of chapter 3 while skipping a shallow plasma 12 cm long with varying values of a constant density. The dashed lines represent the distance between  $f_R$  and  $f_{ce}$  for the initial probing frequency.

line. The dashed lines, which represent the distance between  $f_R$  and  $f_{ce}$ , dictate the order of magnitude of the error profile. In fact, the case with the realistic short plasma

neglected in Fig. 5.5 shows nearly the same error profiles when there is no plasma neglected, but only a non-negligible start density, as displayed in Fig. 5.3.

### 5.1.3 Shifts from errors in the magnetic field

The density profile reconstruction method in X-mode requires the  $f_{ce}$  profile as an input. Any error in the input  $f_{ce}$  profile, specially at the initialization position, will propagate into the density profile reconstructed. To benchmark the magnitude of this error, Fig. 5.7 shows the error profile for various error levels in the magnetic field that defines the  $f_{ce}$  profile. The frequency profiles used as input for this calculations are the profiles introduced in Fig. 5.1.

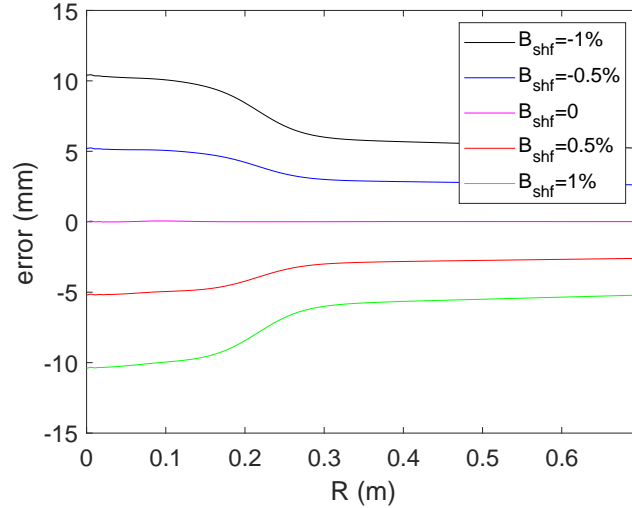


Fig. 5.7 Error profile when reconstructing the density profile using the optimized scheme of Chap. 3 with varying errors in the magnetic field.

Similarly to the previous section, the cause of the errors in the reconstructed profiles comes from breaking the validity of  $f_{prob} = f_{ce}$  at the first cut-off position. But this time, caused by an error in the input magnetic field.

### 5.1.4 Conclusions from benchmarking the initialization errors

From all benchmarks illustrated, it is clear that the error in the determination of the position of the first cut-off is never significantly damped along the profile reconstruction. This is the reason why the initialization is such an important aspect of the profile reconstruction.

The order of magnitude of the initialization error is dictated by the distance between the exact  $f_R$  and the exact  $f_{ce}$  for the first probing frequency. The cause for making this mistake can be a non-negligible initial density or an error in the input  $f_{ce}$  profile. Neglecting a short plasma before the initial position has shown to have a negligible impact compared to the error from the distance between  $f_R$  and  $f_{ce}$ . The techniques to estimate the  $f_{ce}$  profile are a different topic altogether and beyond the scope of this PhD thesis. The estimation of the initial conditions, such as the first cut-off position and the density at that position, however, are tackled using the reflectometer signals. This aspect is investigated in the next section.

## 5.2 Full-wave signals in the vicinity of the first cut-off

The errors benchmarked in the profile initialization occur because it is not straight forward to determine the initialization conditions. This section focuses on how to interpret the time-of-flight and amplitude signals used to estimate these initialization conditions,  $n_{e0}$  and  $R_{n_{e0}}$ .

The first aspect to be observed is the minimal density at which a full reflection can occur. In fact, this aspect can be influenced by the probing frequency and the size of the plasma. Therefore, the tests performed used conventional Tore-Supra equivalent probing frequency around the initialization ( $\approx 70$  GHz) and a plasma radius of 0.7 m. The signal used to determine the initialization frequency is the IQ amplitude signal. The profiles tested are shown in Fig. 5.8. They have a constant density in the core region and a smooth transition in the edge into vacuum. The smooth transition is required to avoid strong reflections due to a jump the refractive index.

Using the  $f_R$  profiles in Fig. 5.8, the IQ amplitude is computed for two different sweeping rates. One 5 GHz/ $\mu$ s case, i.e. in the order of magnitude of the apparatus in most recent tokamaks, as e.g. in JET, and a 20 GHz/ $\mu$ s case, corresponding to the fastest set up used at Tore Supra and Asdex Upgrade. The IQ amplitude signals are displayed in Figs. 5.9 and 5.10.

In the case with a slower sweeping rate, in Fig. 5.9, the frequency of the first cut-off (just above 70 GHz) displays an abrupt but still smooth increase in the amplitude signal. On the faster sweeping rate, in Fig. 5.10, there is a peak present in the same region, and after the peak, the amplitude continues to raise smoothly. This peak is quite low in amplitude and it is due to the interface between plasma and vacuum. In these cases, the interface has a very smooth profile, as depicted in Fig. 5.8. If this transition is not

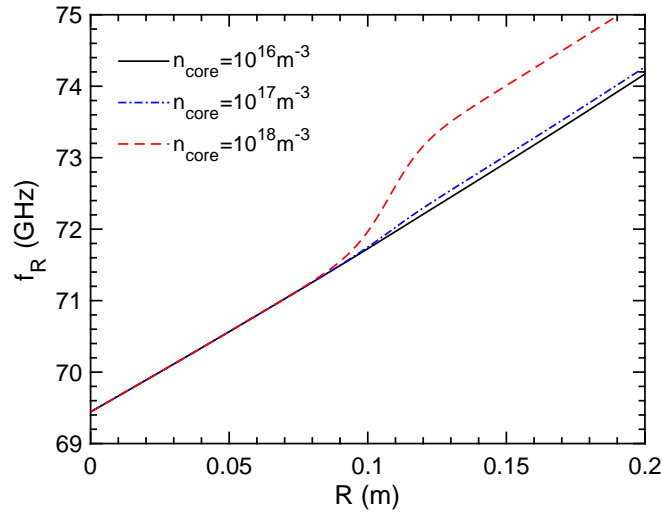


Fig. 5.8 Upper X-mode cut-off profiles of plasmas with constant density and a smooth transition into vacuum in the edge.

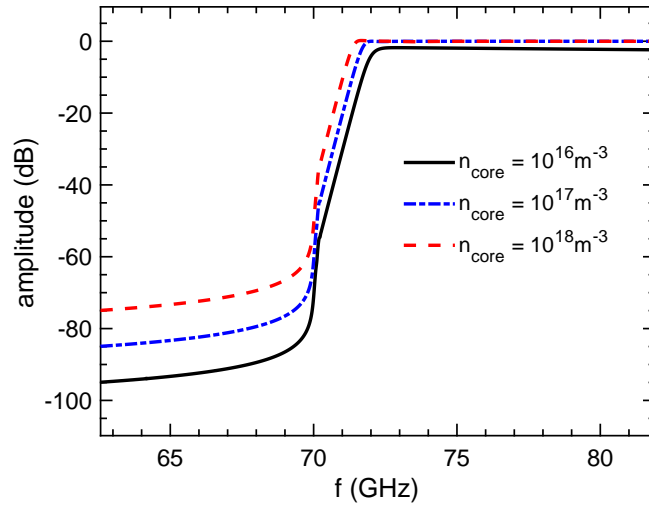


Fig. 5.9 IQ amplitude signal corresponding to a 5 GHz/ $\mu$ s sweep on the profiles introduced in Fig. 5.8.

smooth, this peak can have a significant amplitude and be visible above the noise level. If experimentally this interface is abrupt, this peak from the refractive index jump can be used as an initialization mark.

After reaching the maximum amplitude value, the slower sweeping case keeps a constant amplitude, where the faster sweeping shows a decrease in amplitude. The

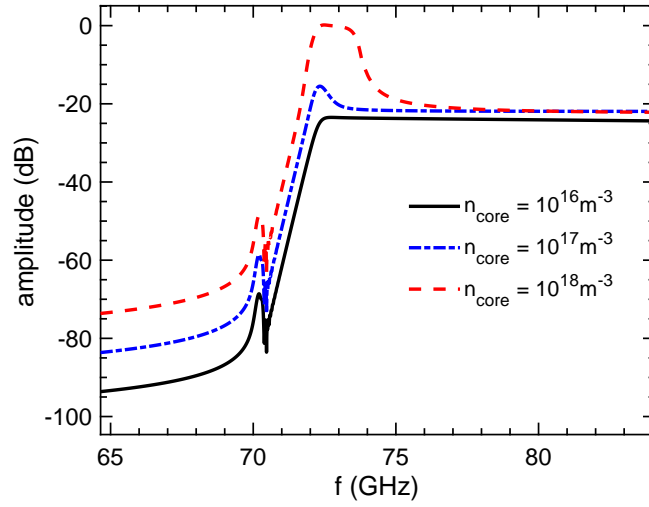


Fig. 5.10 IQ amplitude signal corresponding to a 20 GHz/ $\mu$ s sweep on the profiles introduced in Fig. 5.8.

decrease is surely affected by the transition into a lower gradient zone, but in addition, probing at a higher frequency into the same density is also causing the reflection efficiency to drop. The typical cases in Tore Supra present a noise level up to -30 dB, and a threshold is used to determine the first cut-off frequency, set at around -20 dB. One example can be found in [57]. This means that in the signals in Fig. 5.10, only the highest amplitude signal, of  $10^{18} \text{ m}^{-3}$  density in the core, the amplitude values are well above the -20 dB mark around the initialization frequency. This result gives an idea of the required density to have a strong reflection amplitude around the initialization in order to base the next simulations on. For the 20 GHz/ $\mu$ s sweeping rate, the density at  $10^{17} \text{ m}^{-3}$  is about the lowest density that can produce a strong reflection for the initialization to take place. A more comprehensive investigation of the amplitude rise for various density gradient length in the interface can be found in [78]. There, the density profile is considered linear and increase starting at zero density. The paper concludes with a solution to find the position of  $f_R = f_{ce}$ . An aspect not yet considered was the 3D geometrical aspects, which would need to include the shapes of the probing wavefront and cutoff layer. The scope in this thesis is not to revisit these results in 1D or investigate the 3D effects, but to add new 1D aspects, like the uneven profile around the initialization frequency, examined in the next section. The analyzes will also compare the full-wave and WKB signals. The comparison is performed because the reconstruction algorithm uses the WKB phase expression to recompute part of the waves phase. With these aspects covered, a future prospect will be to verify these results including the 3D geometrical aspects.

### 5.3 Perturbations in the vicinity of the first cut-off

The edge of the confined plasma in tokamaks is the location most prone to turbulence. In addition to the background localized turbulence, profile relaxations can emanate density filaments that propagate outwards. Such perturbations can be the ‘ELMs’ present in H-mode discharges or the ‘blobs’, associated to the development of micro turbulence. In the presence of such perturbations, it is very common to have them crossing the reflectometry initialization region. This section presents 1D simulations of the initialization process in the presence of this kind of perturbations. The main objective is to investigate how they alter the signals and how to take them into account, specially in the scope of comparing the full-wave to the WKB signals.

The base profile for the following tests is the profile used in Fig. 5.8, with a  $10^{18} m^{-3}$  density in the core, and perturbations are added around the initialization frequency. The unperturbed frequency profiles can be found in Fig. 5.11.

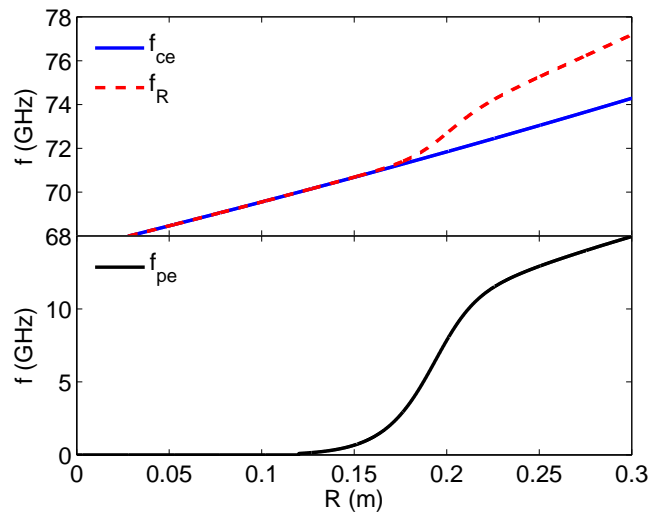


Fig. 5.11 Base frequency profiles for tests of perturbations in the initialization frequency. The density is constant in the core plasma at  $10^{18} m^{-3}$  and a smooth transition in the edge into vacuum

Following the test case profiles in Fig. 5.11, the sweep full-wave simulations are performed with a  $20 \text{ GHz}/\mu\text{s}$  sweeping rate. The respective IQ amplitude have already being illustrated in Fig. 5.10 and the time-of-flight signal can be found in Fig. 5.12.

The slight mismatch between the full-wave and WKB time-of-flight signal is expected and it is an effect of the sweeping rate. The faster the probing frequency is swept, the more enhanced this mismatch becomes. The main difference in the comparison

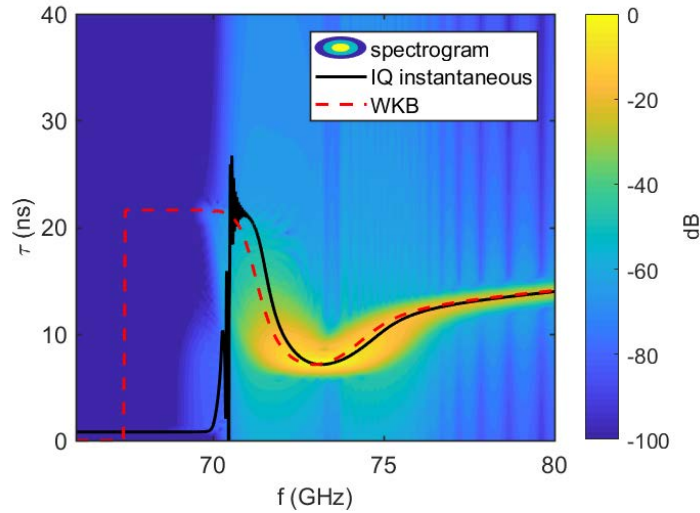


Fig. 5.12 Time-of-flight signals corresponding to the unperturbed profiles of Fig. 5.11, with a sweeping rate of  $20 \text{ GHz}/\mu\text{s}$ .

between the full-wave and the WKB signals is in the frequencies before the top of the IQ amplitude raise. The full-wave signals show a smooth transition between not having a reflection in the plasma into having it. In the WKB signal this transition cannot be taken into account. Even in the locations with zero density, the WKB solution always assumes a cut-off with full reflection. Even though the full-wave signal describes better the experimental signals, the profile reconstruction algorithm uses the WKB solution of the time-of-flight. As a result, the best input for the profile reconstruction is to adapt the experimental signal into a WKB valid signal.

Moving forward, with the profiles and time-of-flight base signals established, a fixed perturbation is inserted in different radial positions. Following the observations from Fig. 5.10, the perturbations were chosen to have amplitude of  $10^{18} \text{ m}^{-3}$  in density. At much lower density, the reflected waves would not have amplitude above the typical background noise level, as concluded in the analysis of Fig. 5.10. The geometry is set with a shape of one period of a sine function and 6 cm width. The probing location at which the IQ amplitude starts to rise in the unperturbed case is around 0.12 m, thus the perturbation is placed around this position. Three positions were chosen for the analysis: 0.06 m; 0.10 m; and 0.14 m. The resulting frequency profiles can be found in Fig. 5.13.

Next, the profiles depicted in Fig. 5.13 are probed with a sweeping rate of  $20 \text{ GHz}/\mu\text{s}$ . The resulting IQ amplitude signals can be found in Fig. 5.14.

The amplitude signals in Fig. 5.14 show a very weak signal ( $\approx -55 \text{ dB}$ ) before probing the density profile, only for the unperturbed case and for the perturbation located at

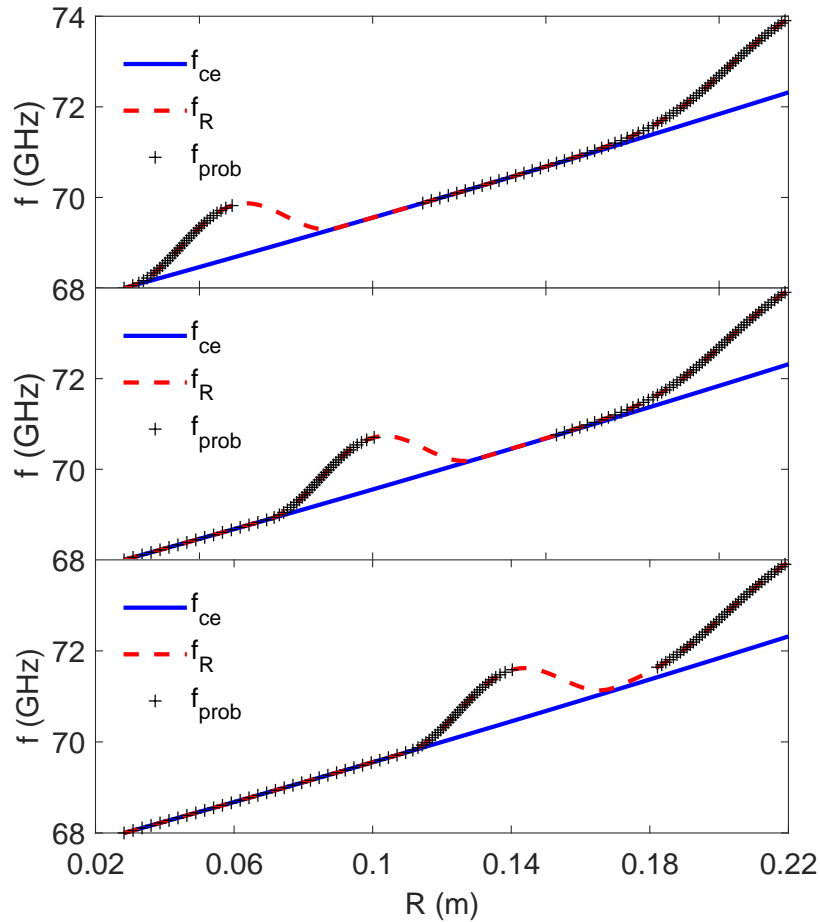


Fig. 5.13 Base frequency profiles of Fig. 5.11 with a perturbation inserted at three different radial positions. From top to bottom,  $R_{pert}=0.06, 0.10$  and  $0.14$  m. In the top case, above the perturbation, there is still a range of probing frequencies on the region with negligible plasma density. For the middle case, the jump frequency matches where it would be the unperturbed initialization frequency. At the bottom case, the frequency jump is already inside the main profile.

0.06 m. When the perturbation is introduced at the radial positions of 0.10 m and 0.14 m, there is a significant increase (into  $\approx -20$  dB) in the amplitude before having any reflections on the density profile. This is caused by the combination of the perturbation and profile shapes introducing matching frequencies to the Bragg condition for reflections. Regardless, there is still a 20 dB difference between the frequencies that are reflected on the density profile or not. The perturbation located at 0.06 m showed no influence in the IQ amplitude. Even though there are strong reflections in the smooth profile

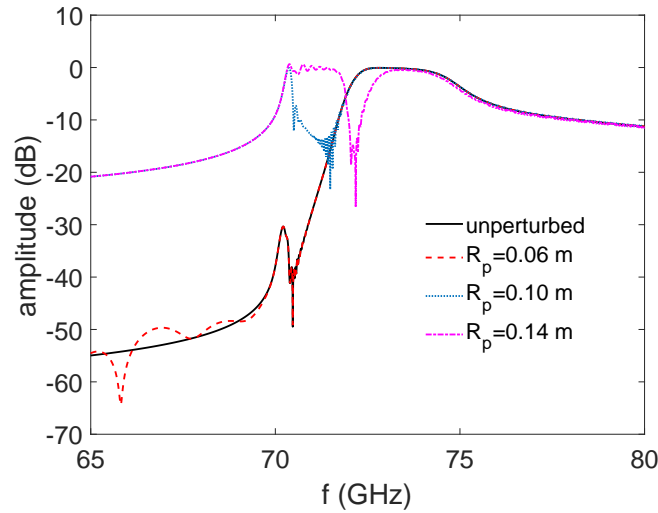


Fig. 5.14 IQ amplitude signals for the simulated probing of the profiles in Fig. 5.13, compared to the unperturbed reference case with the profile from Fig. 5.11.

with core density of  $10^{18}m^{-3}$  as shown in Fig. 5.10, for the small edge perturbation there isn't. As a short perturbation that is completely detached from the density profile, there isn't enough radial length for the evanescent wave to reduce significantly and generate a high reflection rate. This is a clear example of the importance of the plasma size when investigating the first reflected frequency. A complete study of the minimum conditions for a fully detached perturbation to have high amplitude reflections is not covered here. The focus is on how the perturbations alter the initialization technique. As a future prospect, these fully detached perturbations can be reconstructed with the same technique developed in Chap. 4.

The time-of-flight signals corresponding to the perturbation positions of 0.06 m, 0.10 m and 0.14 m can be found in Figs. 5.15, 5.16 and 5.17, respectively.

From the WKB signal in Fig. 5.15, the perturbation left a clear decrease in time-of-flight in the beginning of the perturbation, followed by the jump when the probing wave jumps over the top of the perturbation. The spike in the WKB signal is exactly where the IQ amplitude shown in Fig. 5.14 starts to increase. In the full-wave IQ signal, on the other hand, the signal is exactly the same as the unperturbed case. Combining this fact with the amplitude signal, indeed there isn't enough amplitude coming from the perturbation band to have any impact on the full-wave time-of-flight signal.

The perturbation probing frequency band moves into higher frequencies when the perturbation is placed at 0.10 m. This probing band starts to cover part of the frequencies in the amplitude raise. At this time, the jump in the WKB signal seen in Fig. 5.16 falls

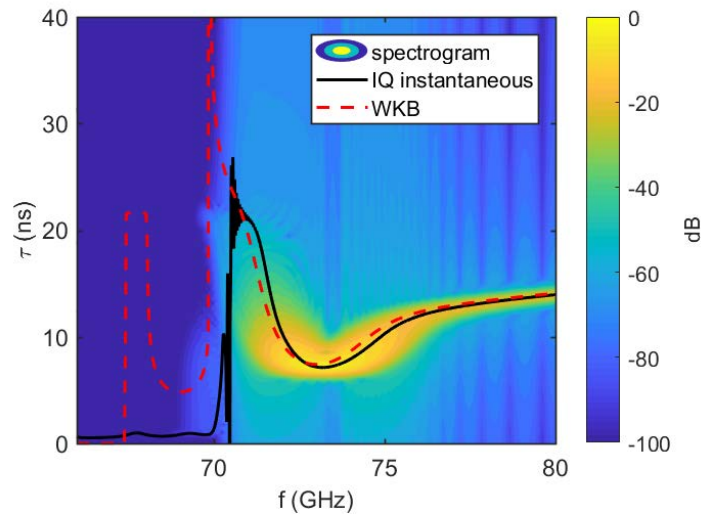


Fig. 5.15 Time-of-flight signals corresponding to frequency profiles of Fig. 5.13, top case, swept at  $20 \text{ GHz}/\mu\text{s}$ . The perturbation is inserted at  $0.06 \text{ m}$  and is directly probed in the frequency range between approximately  $68$  and  $69.8 \text{ GHz}$ .

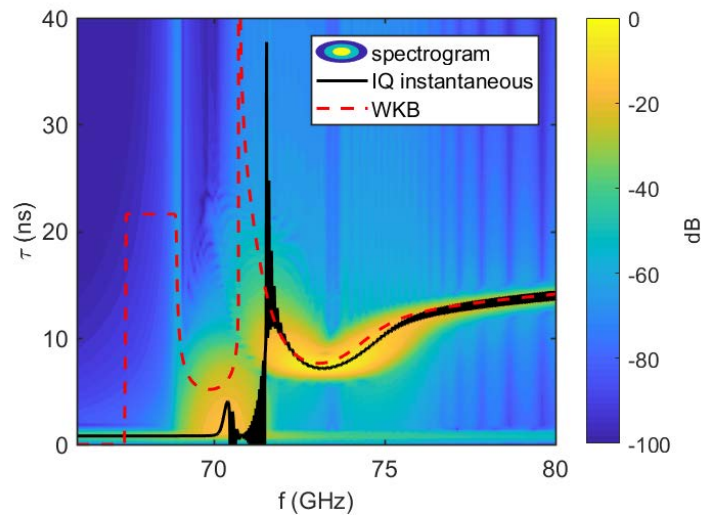


Fig. 5.16 Time-of-flight signals corresponding to frequency profiles of Fig. 5.13, middle case, swept at  $20 \text{ GHz}/\mu\text{s}$ . The perturbation is inserted at  $0.10 \text{ m}$  and is directly probed in the frequency range between approximately  $68.8$  and  $70.8 \text{ GHz}$ .

inside the full-wave time-of-flight transition from not having into having a reflection in the plasma. Observing first the spectrogram signal, the main time-of-flight branch, which lies above  $71 \text{ GHz}$ , seems practically unaffected. The new contribution appears around  $70 \text{ GHz}$  with good amplitude. The signal vanishes again between these two branches,

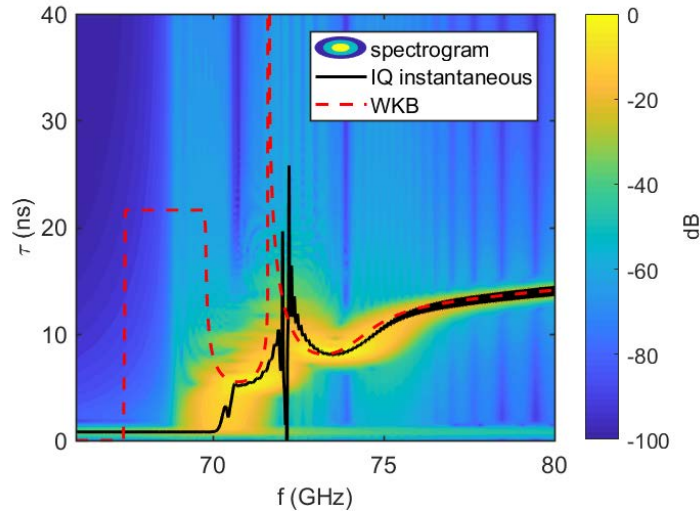


Fig. 5.17 Time-of-flight signals corresponding to frequency profiles of Fig. 5.13, bottom case, swept at  $20 \text{ GHz}/\mu\text{s}$ . The perturbation is inserted at 0.14 m and is directly probed in the frequency range between approximately 69.8 and 71.6 GHz.

back to the background amplitude of -20 dB at 71 GHz, as seen in Fig. 5.14. The frequency of 71 GHz is the typical frequency at which the initialization could start, i.e. at 20 dB below the maximum amplitude reached. At this case, this probing frequency has just crossed above the perturbation. Going back to the results observed in Chap. 4, it is typical along the time-of-flight jump to observe a drop in amplitude followed by a small discontinuity in the spectrogram branch. This can be observed in Figs. 4.7, 4.13 and 4.14 and is further discussed in Sec. 4.4 when observing part of the probing wave tunneling into the valley. At the instantaneous IQ and the WKB signals, on the other hand, the time-of-flight jump is visible. The interpretation from the full-wave effects around this jump is the same as for the blind regions and have been covered in the previous chapter. Nevertheless, it was shown that the full-wave signal around the jump is not WKB compatible and therefore should not be directly injected into the profile reconstruction algorithm. Typically this band is limited to  $\approx 1 \text{ GHz}$ .

The last case is the perturbation located at 0.14 m, with the corresponding time-of-flight signals in Fig. 5.17. In this occasion, the perturbation is just completely attached to the density profile. Just as the time-of-flight starts to move towards the unperturbed solution, the presence of the perturbation causes a drop in the time-of-flight, followed by a positive jump. The time-of-flight jump matched with the 20 dB amplitude drop indicate the presence of this jump. In this case the perturbation signal is fully contained in the main branch of the full-wave signal and can be investigated to extract characteristics

of the perturbation. Even though there is no signal before the perturbation to use interpolation to estimate the unperturbed signal, such cases can still be explored by observing the profile evolution along many frequency sweeps.

Exactly like observed in the previous chapter, the WKB signal does not describe well the reflectometer signal around the jump over perturbations. Thus, it is necessary to adapt the profile reconstruction in this region. The identification of these regions also follow the same principles in Chap. 4, again observed in Figs. 5.14, 5.16 and 5.17. The presence of a jump over a perturbation is signaled with a drop in the IQ amplitude coupled with a spike in the time-of-flight signal. For a 20 GHz/ $\mu$ s sweeping rate, the WKB description of the signal fails in a band around  $\pm 1$  GHz. Only if the frequency distance between two branches in the spectrogram signal at the edge plasma is greater than this range, the perturbation can be considered fully detached.

A fully detached perturbation can be reconstructed by a database technique similar to the one developed in Chap. 4. In this case, the signatures in the time-of-flight signal deviate from the valley perturbation, because in this cases there are two transitions from vacuum to plasma and back to vacuum. These transitions cause drops in the time-of-flight. A complete investigation is yet to be done on the connection between the minimum width and density of these perturbations, as well a connecting the signal shape to the perturbation size. The fully attached perturbations, on the other hand, have the same identification and reconstruction procedure as developed in Chap. 4. The special case is when the bandwidth of time-of-flight jump is exactly where the initialization frequency should be in the unperturbed scenario. In this case, the tunneling and frequency mixing effects described in Chap. 4 delay the first initialization frequency. The best procedure in such cases is to use the adjacent sweeps to estimate the unperturbed signal and use it to initialize the reconstruction. After all, these typical perturbations are moving through the probing area and therefore, in a previous or a next sweep, the perturbation is not present anymore.

## 5.4 Partial conclusions

The benchmarking task produced a reference for the expected error introduced in the reconstructed density profile according to the precision of the different possible error sources. The error can be roughly assumed radially constant, which means that it acts as a shift of the density profile. This benchmarks served not only as a reference for knowing the profile error bars, but also to demonstrate the possible causes for error and their importance. Due to the high error values demonstrated from reasonable parameters, it is

clear that the initialization quality has an important impact on the reconstructed profile accuracy.

The introduction of edge perturbations led to three distinct scenarios: reconstruction of fully detached perturbations; reconstruction of fully attached perturbations; and perturbations that interfere on the standard initialization.

Fully detached perturbations can be treated completely unrelated to the main density profile. A database approach can also be developed in this case, however with different signal shape and constraints, specially for the minimum detectable density connected to the perturbation width. Additional investigation is still necessary to fully describe the signature of these perturbation in the time-of-flight signal and reconstruct their profile.

Fully attached cases do not disturb the initialization and can be identified and reconstructed with the same methodology developed in Chap. 4.

The only additional restriction on the initialization procedure is the partially attached perturbation. In these cases, the unperturbed initialization frequency band is disturbed by the perturbation, typically in the band where the probing frequency jumps over the perturbation into the main profile. The issue in these cases is the lack of interpolatable probing frequencies that helps to estimate the unperturbed profile. The best approach in this case is to observe the neighbouring sweeps to estimate the unperturbed time-of-flight and starting frequency.

The initialization procedure is always subject to the signal noise level. The reflectometer signal's noise mainly originates from micro-turbulence, stranded scatterings, from electron cyclotron emission from the plasma, and even from reflections around the antenna in some situations. Although it is not in the scope of this work to fully access each of these components, the final initialization procedure shall be benchmarked against various background noise levels. The benchmarking allows to infer the expected initialization precision and insert adequate error bars.

### 5.4.1 Future prospects

The ongoing investigation is characterizing the fully detached perturbations and developing the correct approach on the initialization technique in the presence of the partially attached perturbations.

As a future prospect, the different perturbation shapes can be studied with a time-dependent 3D full-wave code. The geometrical aspects of the possible edge perturbations combined with the probing wave-front shape comprise a very complex system that is not fully described with a 1D analysis. These additional geometrical aspects are expected to reduce the contribution of the perturbation signature in most cases, but in specific

---

cases, they can even focus the probing beam and increase the detected amplitude and contribution from the perturbation.

Some experimental evidences on initialization uncertainties were demonstrated in data from the Tore Supra database. This work was performed after the manuscript deposition and therefore it is included in [Appendix C](#).



# Chapter 6

## Conclusions and prospects

### 6.1 General conclusions

The recent continuous advances in the reflectometry diagnostic hardware and data extraction techniques, together with strong requirements for the next generation of fusion experiments, starting at ITER, created a demand which this thesis addresses for deeper understanding and additional improvements on the density reconstruction methods in the data analysis front.

The first topic investigated was the reconstruction algorithm. It was demonstrated that using the radially optimized fractional power integration functions improved the reconstructed profile accuracy and stability because these functions describe well the true refractive index shapes. Although the use of a square root integration profile achieved good results in the core plasma, it is not the best suited shape in the edge plasma. In this region, the power of the fractional power functions can be very close to zero in the first reflected frequencies. The adaptation of the power of these functions according to the plasma profile showed an accuracy improvement in the edge plasma profile of up to two orders of magnitude. The exact improvement depends on the initialization precision and the profile to be reconstructed.

The method elaborated in Sec. 3.8 can be used to determine the entire profile of integration weight factors  $W(R)$  for any profile shape. Optimizing the integration factors also allow to use a reduced number of probing frequencies to reconstruct the profile without any accuracy loss, as demonstrated in two examples. This feature enables the real-time monitoring of faster density profile evolution.

The comparison between all methods investigated also showed how the reconstruction is more stable when not using any information of the previously calculated positions to determine the next position, or even, forcing smoother variation on any of the

reconstruction terms. All these procedures were demonstrated to delay the error damping capability of the reconstruction method when spurious events and phase noise were introduced. In addition, the analysis on the reconstruction stability deduced a better damping of errors for higher values of  $WN_{n-1}$ . The profile of  $WN_{n-1}$  is generally monotonically decreasing radially from the edge to the core, which is quite beneficial for the reflectometry diagnostic since the edge region is typically more prone to turbulence and the reconstruction algorithm is more robust.

The reconstruction of blind regions in frequency swept reflectometry was investigated for the first time in this thesis. As it was demonstrated, the standard reconstruction process add a significant error in the density profile if no special technique is applied around the perturbed region. The work performed here investigated more general characteristics to lay the foundations for this vast area of study.

As a first approximation, the valleys were assumed as having a sine shape. If any other shape is of interest, the database can be recomputed for that specific shape. In the end, a few different shapes can be available if the situation indicates for the preference of a specific shape over the others. Future studies including 3D simulations or a previous knowledge of the perturbation shape being studied can dictate which shape to be used in the database for a more accurate estimation of the perturbation depth.

The error in the perturbation reconstruction from the computed database was showed to not vary significantly along any plasma parameters, and that they are never above a few %. The main reconstruction error sources are due to noise in the time-of-flight and  $f_{ce}$  signals, and on the assumptions made on the unperturbed profile gradient, the perturbation width, and the perturbation shape. The assumptions on the unperturbed profile gradient and the width of the perturbation will vary according to each application. In the cases where data is available for a clear and well-behaved evolution of the profile, these assumptions are straight forward and accurate. If there is available only a single sweep and the profile include high amplitude low  $k$  perturbations, these assumptions will not be as accurate. As a future prospect, the assumption on the estimated shape can be corroborated with theoretical predictions or numerical simulations of the perturbations being studied.

The perturbation signatures in the time-of-flight signal have been investigated in the most general approach reasonably possible. Due to this characteristic, any simplified reconstruction method that can still be satisfactorily used, can be easily derived from the generalized solution presented. An example of such a simplified method is to use of a small set of frequencies instead of fitting a broad band of probing frequencies, or even only using the integral of the excess time-of-flight.

The full-wave effects displayed have been avoided in the technique to reconstruct the blind regions. The observed full-wave effects rarely have enough amplitude to be distinguishable in a noisy experimental signal. The reliable extraction of information from these effects will only be possible when further developments in the hardware front are achieved. Furthermore, the amplitude of these effects can still be strongly linked to the 3D geometrical aspects that need to be investigated in 3D full-wave simulations. After all, the probing beam area and shape, plus the shape of the perturbations, make in conjunction a system too complex to be completely described in one dimension. The geometrical aspects also heavily influence the amplitude evolution, which is a topic to be further investigated in the case of blind regions and specially for the initialization technique.

The initialization benchmarking produced a reference for the expected error introduced in the reconstructed density profiles according to the precision of the different possible error sources. The error can be roughly assumed radially constant, which means that it acts as a shift of the density profile. This benchmark served not only as a reference for knowing the profile error bars, but also to demonstrate the possible causes for error and their importance. Due to the high error values demonstrated from reasonable parameters, it is clear that the initialization quality has an important impact on the reconstructed profile accuracy.

The introduction of edge perturbations led to two distinct research paths: reconstruction of fully detached perturbations; and adjustments on the initialization technique when observing perturbations around the first reflected frequency. The fully detached perturbations can be treated completely unrelated to the main density profile using a similar database approach as developed in Chap. 4. The only additional restriction on the initialization procedure is the partially attached perturbation. In these cases, the unperturbed initialization frequency band is disturbed by the perturbation, typically in the band where the probing frequency jumps over the perturbation into the main profile. The issue in these cases is the lack of interpolatable probing frequencies that helps to estimate the unperturbed profile. The best approach in this case is to observe the neighbouring sweeps to estimate the unperturbed time-of-flight and starting frequency.

The initialization procedure is always subject to the signal noise level. The reflectometer signal's noise mainly originates from micro-turbulence, stranded scatterings, from electron cyclotron emission from the plasma, and even from reflections around the antenna in some situations. Although it is not in the scope of this work to fully access each of these components, the final initialization procedure shall be benchmarked

against various background noise levels. The benchmarking allows to infer the expected initialization precision and insert adequate error bars.

Overall, this thesis provided a solid knowledge on the density profile algorithm for X-mode. The optimization of the integration factors minimized the error in the density profile due to the reconstruction technique. The sources that dictate the final error are now only originated from the experimental noise level, the description of blind areas and on the initialization technique. The work on the description of blind areas is surely not in its final stage yet. Although it was demonstrated that the error of the database reconstruction approach is very small, in the order of a few %, there is still room for further development on the assumptions made and specially into analysing real non-synthetic applications. The main driving errors in the initialization technique have been identified and an initial assessment already illustrated how the initialization can be improved, although additional work is still necessary to demonstrate practical improvements.

## 6.2 Future prospects

The work presented about the description of blind areas is pioneer in this topic. The initial approach has led to a database based method to reconstruct the blind areas. This method still has to be demonstrated in practice on non-synthetic data. If additional information is required from the perturbations signal, the inverse scattering approach can be used to study the information in the scattered waves from the perturbation. First of all, in order for this approach to be successful, the experimental signals still have to demonstrate strong scattering above the signal's noise level. In addition, this problem can only be studied with close compatibility with the real case if studied with a 3D time-dependant full-wave code[79]. The geometrical aspects of the possible edge perturbations combined with the probing wave-front shape comprise a very complex system that is not fully described with a 1D analysis. Such 3D code is being tested and is foreseen to soon be applied into practical cases, including the description of the signals from these blind areas.

The 3D geometrical aspects are also foreseen to play a role in the description of the perturbations that are fully detached from the main profile, and on the initialization technique in the presence of perturbations around the first reflected frequency. The work started here on the initialization still needs refinements and to demonstrate practical improvements. Then the same 3D time-dependant code will be used to evaluate the geometrical impact on these initialization techniques.

# References

- [1] EIA (U.S. Energy Information Administration), International Energy Outlook 2017. <https://www.eia.gov/outlooks/aeo/>.
- [2] J. Hansen, R. Ruedy, M. Sato, and K. Lo. Global surface temperature change. *Reviews of Geophysics*, 48(4), 2010. RG4004.
- [3] J. Cook et. al. Quantifying the consensus on anthropogenic global warming in the scientific literature. *Environmental Research Letters*, 8(2):024024, 2013.
- [4] World Energy Council. World Energy Scenarios 2016 - The Grand Transition, 2016. [www.worldenergy.org/publications/2016/world-energy-scenarios-2016-the-grand-transition](http://www.worldenergy.org/publications/2016/world-energy-scenarios-2016-the-grand-transition).
- [5] A. S. Eddington. The internal constitution of the stars. *The Observatory*, 43:341–358, 1920.
- [6] F. Chen. *Introduction to Plasma Physics and Controlled Fusion*. Springer US, 1984.
- [7] S Nakai and H Takabe. Principles of inertial confinement fusion - physics of implosion and the concept of inertial fusion energy. *Reports on Progress in Physics*, 59(9):1071, 1996.
- [8] <http://www.lhd.nifs.ac.jp/en/home/lhd.html>.
- [9] <http://www.ipp.mpg.de/w7x>.
- [10] A. Dinklage et. al. Core confinement in Wendelstein 7-X limiter plasmas. Talk and proceeding at the 43rd EPS conference, 2016. <http://ocs.ciemat.es/EPS2016PAP/pdf/O2.107.pdf>.
- [11] S.A. Bozhenkov et. al. Power balance analysis of Wendelstein 7-X plasmas using profile diagnostics. Talk and proceeding at the 43rd EPS conference, 2016. <http://ocs.ciemat.es/EPS2016PAP/pdf/O2.106.pdf>.
- [12] M. Otte et. al. Magnetic flux surface measurements at Wendelstein 7-X. Talk and proceeding at the 43rd EPS conference, 2016. <http://ocs.ciemat.es/EPS2016PAP/pdf/O2.105.pdf>.
- [13] <https://focusfusion.org>.
- [14] [www.iter.org](http://www.iter.org).

- 
- [15] [www.euro-fusion.org/programme](http://www.euro-fusion.org/programme).
- [16] <https://www.euro-fusion.org/jet>.
- [17] [www.euro-fusion.org](http://www.euro-fusion.org).
- [18] <http://www-fusion-magnetique.cea.fr/gb/cea/ts/ts.htm>.
- [19] <http://www.ipp.mpg.de/16195/asdex>.
- [20] <http://west.cea.fr>.
- [21] J. Freidberg. *Plasma Physics and Fusion Energy*. Cambridge University Press, 2008.
- [22] J. D. Lawson. Some criteria for a power producing thermonuclear reactor. Atomic Energy Research Establishment, Harwell, Berkshire, U. K, 1955.
- [23] H. P. Furth. Tokamak research. *Nuclear Fusion*, 15(3):487, 1975.
- [24] Ch. P. Ritz et. al. Fluctuation-induced energy flux in the tokamak edge. *Phys. Rev. Lett.*, 62:3099–3099, 1989.
- [25] H. Iguchi, K. Kadota, K. Takasugi, T. Shoji, M. Hosokawa, M. Fujiwara, and H. Ikegami. Space and time-resolved measurements of plasma density by a lithium neutral beam probe in NBT-1M. *Review of Scientific Instruments*, 56:1050, 1985.
- [26] D. M. Thomas. Development of lithium beam emission spectroscopy as an edge fluctuation diagnostic for DIII-D. *Review of Scientific Instruments*, 66(1):806–811, 1995.
- [27] A Komori, O Mitarai, K Yamagiwa, C Honda, K Kadota, J Fujita, YT Lie, U Samm, A Pospieszczyk, K Höthker, et al. Observations of low frequency density fluctuations in a tokamak edge plasma. *Nuclear fusion*, 28(8):1460, 1988.
- [28] Evgeny V Shun’ko. *Langmuir probe in theory and practice*. Universal-Publishers, 2009.
- [29] H. M. Mott-Smith and Irving Langmuir. The theory of collectors in gaseous discharges. *Phys. Rev.*, 28:727–763, 1926.
- [30] I. H. Hutchinson. *Principles of Plasma Diagnostics*. Cambridge University Press, UK, 2002.
- [31] Grégoire Hornung. *Study of plasma turbulence by ultrafast sweeping reflectometry on the Tore Supra tokamak*. PhD thesis, Aix-Marseille Université, 2013.
- [32] Hugo Arnichand. *Identification of trapped electron modes in frequency fluctuation spectra of fusion plasmas*. PhD thesis, Aix-Marseille Université, Ugent, CEA Cadarache, Forschungszentrum Jülich, 2015.
- [33] H. Arnichand et. al. Identification of trapped electron modes in frequency fluctuation spectra. *Plasma Physics and Controlled Fusion*, 58(1):014037, 2016.

- 
- [34] Georgiy V. Zadvitskiy. *Experimental and numerical study of turbulence in fusion plasmas using gyrokinetics codes data in reflectometry synthetic diagnostics*. PhD thesis, Université de Lorraine, 2018.
- [35] G. V. Zadvitskiy, S. Heuraux, C. Lechte, S. Hacquin, and R. Sabot. Edge turbulence effect on ultra-fast swept reflectometry core measurements in tokamak plasmas. *Plasma Physics and Controlled Fusion*, 2017.
- [36] M. Hirsch, E. Holzhauser, J. Baldzuhn, and B. Kurzan. Doppler reflectometry for the investigation of propagating density perturbations. *Review of Scientific Instruments*, 72(1):324–327, 2001.
- [37] X. L. Zou, L. Laurent, and J. M. Rax. Scattering of an electromagnetic wave in a plasma close to a cut-off layer. application to fluctuation measurements. *Plasma Physics and Controlled Fusion*, 33(8):903, 1991.
- [38] I. H. Hutchinson. One-dimensional full-wave analysis of reflectometry sensitivity and correlations. *Plasma Physics and Controlled Fusion*, 34(7):1225, 1992.
- [39] B. B. Afeyan, A. E. Chou, and B. I. Cohen. The scattering phase shift due to bragg resonance in one-dimensional fluctuation reflectometry. *Plasma Physics and Controlled Fusion*, 37(3):315, 1995.
- [40] C. Fanack, I. Boucher, F. Clairet, S. Heuraux, G. Leclert, and X. L. Zou. Ordinary-mode reflectometry: modification of the scattering and cut-off responses due to the shape of localized density fluctuation. *Plasma Phys. Control. Fusion*, 38(1915-1930), 1996.
- [41] M. Colin. *Modélisations d'un réflectomètre mode X en vue de caractériser les fluctuations de densité et de champ magnétique: Applications aux signaux de Tore Supra*. PhD thesis, Université de Lorraine, 2001.
- [42] E. Z. Gusakov, A. V. Surkov, and A. Yu Popov. Multiple scattering effect in doppler reflectometry. *Plasma Physics and Controlled Fusion*, 47(7):959, 2005.
- [43] F. da Silva, S. Heuraux, E. Z. Gusakov, and A. Popov. A numerical study of forward- and backscattering signatures on doppler-reflectometry signals. *IEEE Transactions on Plasma Science*, 38(9):2144–2149, 2010.
- [44] L. G. Bruskin, A. Mase, and T. Tamano. Microwave scattering near the cut-off layer by density and magnetic field fluctuations. *Plasma Physics and Controlled Fusion*, 36(4):681, 1994.
- [45] L. Colas, X.L. Zou, M. Paume, J.M. Chareau, L. Guiziou, G.T. Hoang, Y. Michelot, and D. Grésillon. Internal magnetic fluctuations and electron heat transport in the Tore Supra tokamak: Observation by cross-polarization scattering. *Nuclear Fusion*, 38(6):903, 1998.
- [46] David Colton and Rainer Kress. *Inverse Acoustic and Electromagnetic Scattering Theory*. Springer-Verlag New York, 2013.
- [47] Maciej Dunajski. *Solitons, Instantons and Twistors*. Oxford University Press, 2010.

- 
- [48] C. Gil et. al. Diagnostic systems on Tore Supra. *Fusion Science and Technology*, 56(3):1219–1252, 2009.
- [49] Ph. Moreau, F. Clairet, J. M. Chareau, M. Paume, and C. Laviron. Ultrafast frequency sweep heterodyne reflectometer on the Tore Supra tokamak. *Review of Scientific Instruments*, 71:74–81, 2000.
- [50] F. Clairet et. al. X-mode heterodyne reflectometer for edge density profile measurements on Tore Supra. *Review of Scientific Instruments*, 72(1):340–343, 2001.
- [51] F. Clairet, B. Ricaud, F. Briolle, S. Heuraux, and C. Bottereau. New signal processing technique for density profile reconstruction using reflectometry. *Review of Scientific Instruments*, 82(083502), 2011.
- [52] F. Briolle, R. Lima, and R. Vilela Mendes. Tomographic analysis of reflectometry data: II. the phase derivative. *Measurement Science and Technology*, 20(10):105502, 2009.
- [53] E. J. Doyle. Status of the system design and component testing for the ITER low-field side reflectometer system, 2015.
- [54] C. Laviron, A. J. H. Donné, M. E. Manso, and J. Sanchez. Reflectometry techniques for density profile measurements on fusion plasmas. *Plasma Phys. Control. Fusion*, 38, 1996.
- [55] E. Mazzucato. Microwave reflectometry for magnetically confined plasmas. *Review of Scientific Instruments*, 69(6), 1998.
- [56] R. Sabot, F. Clairet, C. Honoré, C. Bottereau, J.-M. Chareau, F. Gabillet, P. Hennequin, S. Heuraux, G. Leclert, A. Sirinelli, A. Truc, and L. Vermare. Advances of reflectometry on Tore Supra: From edge density profile to core density fluctuations. *International Journal of Infrared and Millimeter Waves*, 25(2):229–246, 2004.
- [57] F. Clairet, C. Bottereau, J. M. Chareau, and R. Sabot. Advances of the density profile reflectometry on Tore Supra. *Review of Scientific Instruments*, 74(3), 2003.
- [58] H. Bottollier-Curtet and G. Ichtchenko. Microwave reflectometry with the extraordinary mode on tokamaks: Determination of the electron density profile of Petula-B. *Review of Scientific Instruments*, 58(539), 1987.
- [59] N. Bretz. One-dimensional modeling of the wavelength sensitivity, localization, and correlation in reflectometry measurements of plasma fluctuations. *Physics of Fluids B: Plasma Physics*, 4(8):2414–2422, 1992.
- [60] Samuel Daniel Conte and Carl W. De Boor. *Elementary Numerical Analysis: An Algorithmic Approach*. McGraw-Hill Higher Education, 1980.
- [61] R. B. Morales, S. Hacquin, S. Heuraux, and R. Sabot. Density profile reconstruction for fusion plasmas with reflectometry. Poster session at Seminaire de l'école doctoral EMMA, Metz, France, 2015.

- [62] R. B. Morales, S. Hacquin, S. Heuraux, and R. Sabot. Density profile reconstruction methods for X-mode reflectometry, 2015. [www.fz-juelich.de/conferences/IRW12](http://www.fz-juelich.de/conferences/IRW12).
- [63] R. B. Morales, S. Hacquin, S. Heuraux, and R. Sabot. Density profile reconstruction methods for X-mode reflectometry in fusion plasmas. Talk and proceeding at the 43rd European Physical Society Conference on Plasma Physics, Leuven, Belgium, 2016. <http://ocs.ciemat.es/EPS2016PAP>.
- [64] R. B. Morales, S. Hacquin, S. Heuraux, and R. Sabot. New density profile reconstruction methods in x-mode reflectometry. *Review of Scientific Instruments*, 88(043503), 2017.
- [65] R. B. Morales, S. Hacquin, S. Heuraux, and R. Sabot. New density profile reconstruction methods for X-mode reflectometry. Talk and proceeding at the 13th International Reflectometry Workshop, Daejeon, South Korea, 2017. <http://irw13.nfri.re.kr>.
- [66] H. Bottollier-Curtet. *Réflexométrie hyperfréquence pour la détermination de la densité électronique et de ses fluctuations sur le Tokamak Petula-B*. PhD thesis, Université de Paris XI, 1986.
- [67] D. A. Shelukhin et. al. X-mode lower cutoff high field side reflectometer for electron density profile measurements in T-10 tokamak. 11th International Reflectometry Workshop, Palaiseau, France, 2011. [www.lptp.polytechnique.fr/news/11/Workshop/index.html](http://www.lptp.polytechnique.fr/news/11/Workshop/index.html).
- [68] S. Heuraux, S. Hacquin, F. da Silva, F. Clairet, R. Sabot, and G. Leclert. Radial wave number spectrum of density fluctuations deduced from reflectometry phase signals. *Review of Scientific Instruments*, 74(1501), 2003.
- [69] T. Gerbaud, F. Clairet, R. Sabot, A. Sirinelli, H. Heuraux, G. Leclert, and L. Vermare. Comparison of density fluctuation measurements between O-mode and X-mode reflectometry on Tore Supra. *Review of Scientific Instruments*, 77(10E928), 2006.
- [70] R. Sakamoto, B. Pégourié, F. Clairet, A. Géraud, C. Gil, S. Hacquin, and F. Köchl. Cross-field dynamics of the homogenization of the pellet deposited material in Tore Supra. *Nucl. Fusion*, 53(063007), 2013.
- [71] A. J. H. Donné, J. C. van Gorkom, V. S. Udintsev, C. W. Domier, A. Krämer-Flecken, N. C. Luhmann, and F. C. Schüller. Evidence for high- $m$  secondary islands induced by large low- $m$  islands in a tokamak plasma. *Phys. Rev. Lett.*, 94:085001, 2005.
- [72] B. Baiocchi, C. Bourdelle, C. Angioni, F. Imbeaux, A. Loarte, M. Maslov, and JET Contributors. Transport analysis and modelling of the evolution of hollow density profiles plasmas in JET and implication for ITER. *Nuclear Fusion*, 55(12):123001, 2015.
- [73] S. Heuraux, E. Gusakov, A. Yu Popov, F. da Silva, and M. Irzak. Simulations on the role of the resonance of the probing wave on reflectometry measurements in fluctuating plasmas. *IEEE Trans. Plasma Sci*, 38(2150), 2010.

- 
- [74] K. G. Budden. *Radio Waves in the Ionosphere*. Cambridge University Press, UK, 1966.
- [75] E. Z. Gusakov, S. Heuraux, and A. Yu. Popov. Strong bragg backscattering in reflectometry. *Plasma Phys. Control. Fusion*, 51(065018), 2009.
- [76] M. Abramowitz and I. A. Stegun (Eds.). *Handbook of Mathematical Functions with Formulas, Graphs, and Mathematical Tables, 9th printing*. Dover Books on Mathematics, New York, 1972.
- [77] J. Santos, F. Nunes, M. Manso, and I. Nunes. Neural network evaluation of reflectometry density profiles for control purposes. *Review of Scientific Instruments*, 70(521), 1999.
- [78] S. Heuraux, F. Clairet, and F. da Silva. An x-mode reflectometry study on the reflection point for the density profile reconstruction. Talk and proceeding at the 9th International Reflectometry Workshop, Lisbon, Portugal, 2009. [www.ipfn.tecnico.ulisboa.pt/irw9](http://www.ipfn.tecnico.ulisboa.pt/irw9).
- [79] F. da Silva, M. Campos Pinto, B. Després, and S. Heuraux. Stable explicit coupling of the yee scheme with a linear current model in fluctuating magnetized plasmas. *Journal of Computational Physics*, 295(Supplement C):24 – 45, 2015.

# Appendix A

## Experimental application of optimized $W(\mathbf{f})$

The optimization of the profile reconstruction algorithm was discussed in Chap. 3. In Sec. 3.9, a difficult synthetic case was assumed to demonstrate the advantages of optimizing the weight factor  $W(f_{prob})$ , as obtained in Sec. 3.8. Not only the reconstruction was demonstrated more accurate when using the optimized  $W(f_{prob})$ , it also enabled using less probing frequencies without losing accuracy. This appendix applies the same procedure in an experimental data set from the Tore Supra tokamak. Since the real correct profile is not known in an experimental situation, the focus in this section is on demonstrating a reduction of the initial fluctuations and being able to reduce the number of probing frequencies without losing accuracy.

The experimental demonstration of these results are important to validate them in experimental conditions. The data available was the shot 32029 analysed after the deposition of the PhD manuscript. In this appendix only a single sweep was used, measured at  $t = 3.0037$  s. Three edge density profiles reconstructed for this sweep are illustrated in Fig. A.1.

For the profile reconstructions of Fig. A.1 with 100 frequency steps, Fig. A.2 shows, at the top, the value of the refractive index in the previously known positions,  $N_{n-1}$ , at each frequency. At the bottom plot, the computed optimized weight factors are illustrated. The values of  $N_{n-1}$  close to one indicate a region where it is crucial to optimize the weight factors  $W$ .

As can be observed in Fig. A.1, reducing the number of probing frequencies to 100 degraded significantly the density profile in the edge region. Optimizing the weight factors  $W(f_{prob})$  decreased this discrepancy but not to the full extent as expected to follow up the synthetic test cases in Chap. 3. The solution for the optimized weight factors

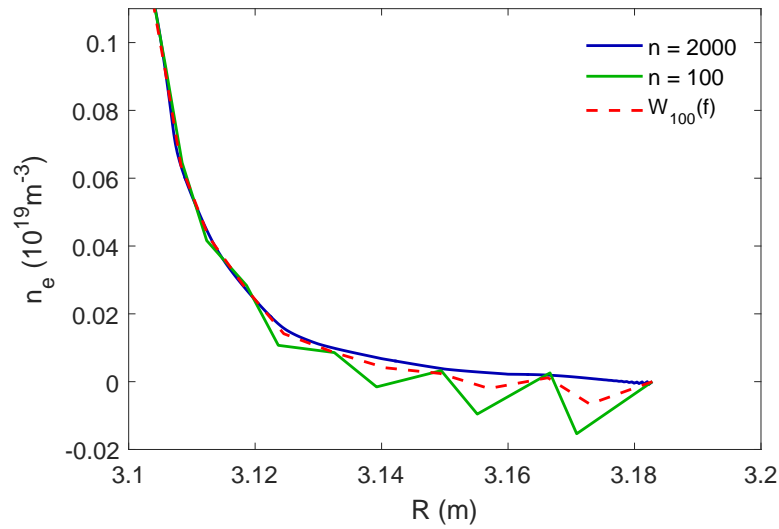


Fig. A.1 Comparison between edge density profiles when using 2000 or 100 frequency steps with the constant  $W = 2/3$  and also a case with 100 frequency steps with  $W(f_{prob})$  optimized for each probing frequency. Tore Supra discharge 32029 at  $t = 3.0037$  s.

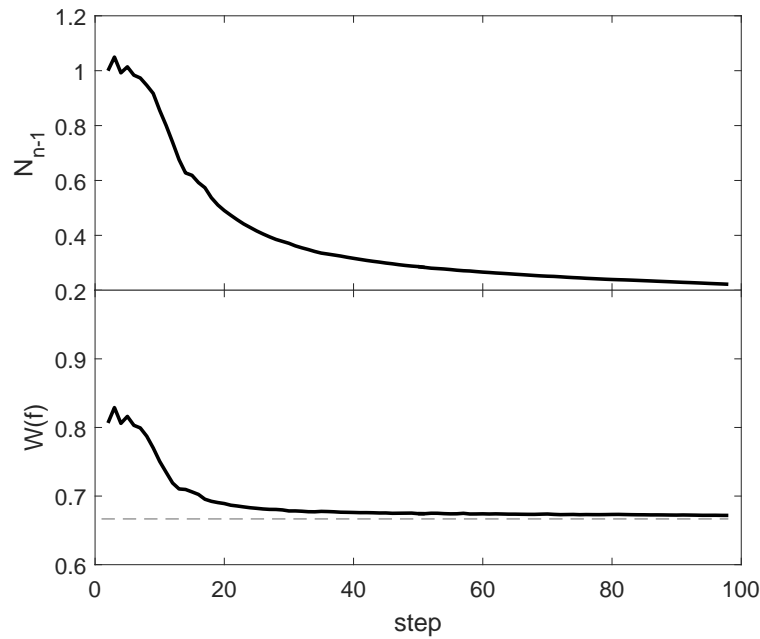


Fig. A.2 Two parameters from the profile reconstructions in Fig. A.1 when using 100 frequency steps. At the top, the refractive index in the previous known position, and at the bottom, the optimized weight factors.

were demonstrated very accurately in Chap. 3, thus the cause for the discrepancy must come from the data inserted in the calculations. The weight factors are functions of the probing frequency (which is well known) and the local gradient of the cut-off frequency,  $\nabla f_R$ . An error in  $\nabla f_R$  can only be caused by an error in the calculated magnetic field profile. The computation of the magnetic field profile must have an inaccuracy when accounting for the ripple effect in this edge region.

By adjusting the input values of  $\nabla f_R$  when computing  $W(f_{prob})$ , the reconstructed profiles with 2000 and 100 frequency steps can be closer to each other. Fig. A.3 shows an example when assuming the values of  $\nabla f_R$  to be multiplied by 0.47 everywhere. This value was found simply by minimizing the discrepancy between the density profiles.

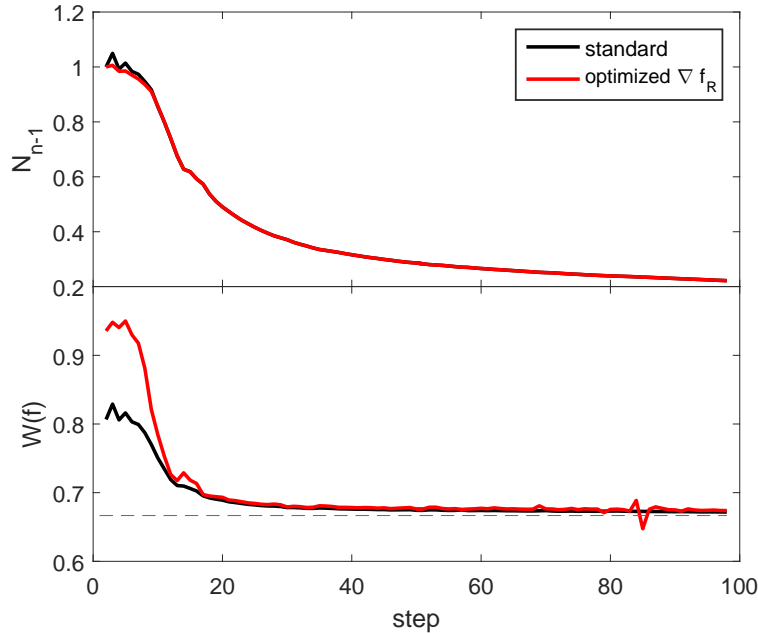


Fig. A.3 Comparison of two reconstruction parameters between two cases when using the originally computed  $\nabla f_R$  profile and when adjusting it by multiplying by 0.47. The parameters are related to the profile reconstructions in Fig. A.4 when using 100 frequency steps. At the top, the refractive index in the previous known position, and at the bottom, the optimized weight factors.

By taking a better profile of  $\nabla f_R$ , the top plot in Fig. A.3 already illustrates how the fluctuations are decreased in the initial reconstruction positions and  $N_{n-1}$  never goes above one, which is an indication of a more accurate reconstruction. Fig. A.3, at the bottom plot, also indicates how the optimized weight factors have changed significantly,

being much greater in the edge region. The density profiles reconstructed under these conditions are displayed in Fig. A.4.

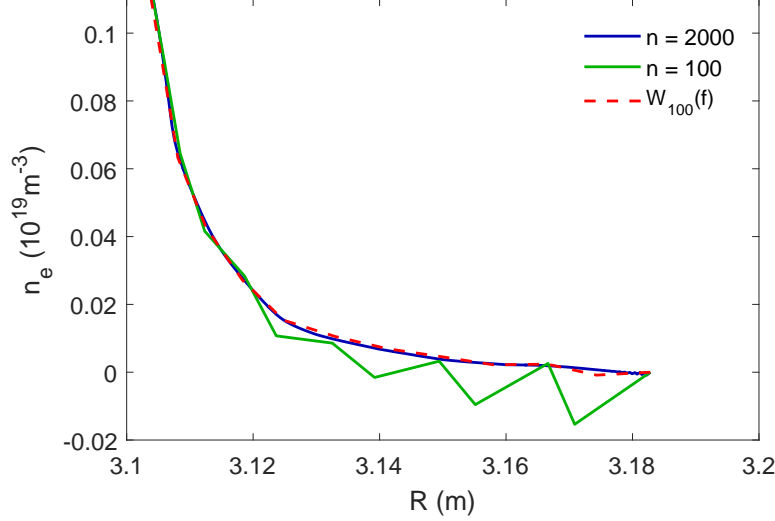


Fig. A.4 Comparison between edge density profiles when using 2000 or 100 frequency steps with the constant  $W = 2/3$  and also a case with 100 frequency steps with  $W(f_{prob})$  optimized for each probing frequency. In this case, the values of  $\nabla f_R$  used to compute  $W(f_{prob})$  have been multiplied by 0.47. Tore Supra discharge 32029 at  $t = 3.0037$  s.

The simple alteration in the profile of  $\nabla f_R$  already showed significant improvement in the agreement between profiles reconstructed with 2000 and 100 frequency steps, as shown in Fig. A.4. For an even better agreement, the adjustment on the profile of  $\nabla f_R$  can be further refined by minimizing the discrepancy between the profiles at each frequency step. The optimized profile of  $\nabla f_R$  can also be used to optimize  $W(f_{prob})$  for the case of 2000 frequency steps.

The sensitivity of the calculation of  $W(f_{prob})$  to the local  $\nabla f_R$  allowed to verify the calculation of the magnetic field in the edge region. This result can have significant impact on the reconstructed edge density profiles when there are any errors in the computed magnetic field, specially if reducing the number of probing frequencies to speed up the reconstruction for real time applications.

In addition, this result can also benefit a refined initialization technique. The method of finding the first reflected frequency needs improvement and is currently under investigation. As the initialization technique becomes more refined, the accuracy on the value of  $\nabla f_R$  in the edge will become an essential parameter.

# Appendix B

## Experimental demonstration of blind area reconstruction

Chap. 4 covered the problem of reconstructing density profiles over valleys that introduce a blind areas. The techniques and signals have been investigated with the use of simulations under the WKB approximation and full-wave in 1D. This appendix applies the techniques discussed in Chap. 4 in an experimental case analysed after the deposition of the PhD manuscript. The data available was the shot 32029.

The best frequency and amplitude signals around the perturbation to be analysed are displayed in Fig. B.1.

Fig. B.1 shows the density perturbation to be reconstructed around the 100 GHz probing frequency. The indications of the perturbation are the discontinuity on the spectrogram and a strong drop in the amplitude signal in the respective probing frequency. This behaviour is due to the tunnelling effect in this area, as already observed in Chap. 4.

In the signal used to analyse the density perturbation, as displayed in Fig. B.1, only a broad (40 MHz) bandpass filter was applied. The narrow band filtering along the main branch was found to smooth the signal observed in the presence of these discontinuities on the spectrogram. Since the perturbation signal is analysed aided by a reference unperturbed signal, the reference signal is taken from a previous sweep that had no perturbation around the 100 GHz probing frequency. The reference signal was filtered with the same broad bandpass filter, followed by a narrow (8 MHz) bandpass filter along the main branch in the spectrogram. The standard window size used for each FFT in the spectrogram was 128 points for the reference signal. For the perturbed signal, on the other hand, the perturbation signature was found to be better described (not smoothed)

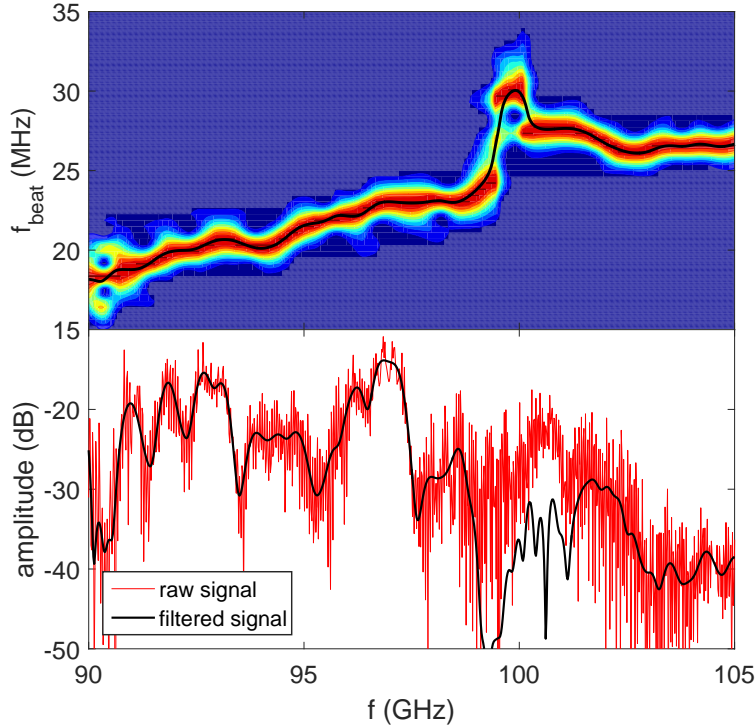


Fig. B.1 Beat frequency and amplitude signals around the perturbation to be investigated. Only a broad bandpass filter was applied to remove reflections that were far from the main branch. Tore Supra discharge 32029 at  $t = 3.0037$  s.

with a window size of 90 points. Fig. B.2 illustrates the time-of-flight signal of the perturbation compared to the reference unperturbed signal in white.

The specific perturbation found in this discharge is a magnetic island that typically appear with a positive density perturbation followed by a negative density perturbation. The positive part of the perturbation can still be traditionally probed and reconstructed. Therefore, in this case, instead of using a database of sine valleys, the perturbation shape follows the same shape as the positive part that is probed. The perturbation is split into four quarters, and the first quarter is taken from the probed section, as demonstrated in Fig. B.3 for the data from Fig. B.2.

As the width is determined, the second and third quarters of the perturbation are squeezed or stretched to arrive at the desired perturbation width. The width is determined by estimating the end frequency of the perturbation, and associating that probing frequency to a position in the unperturbed density profile. The signature for the perturbation end is always a dip in the time-of-flight signal when the perturbation end is

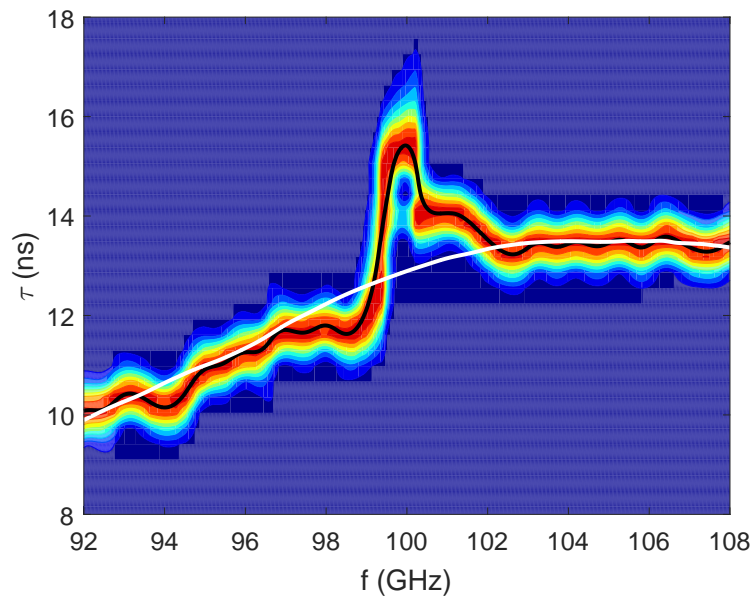


Fig. B.2 Time-of-flight signal around the perturbation of interest compared to the reference unperturbed case in white. Tore Supra discharge 32029, with the perturbation at  $t = 3.0037$  s and the reference unperturbed case at  $t = 3.0033$  s.

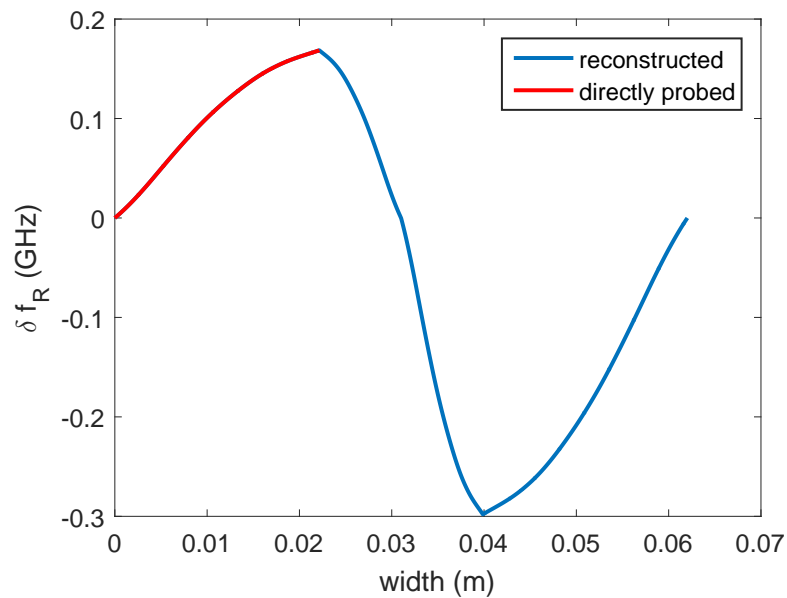


Fig. B.3 Complete perturbation in  $f_R$  formed by a partially probed first quarter that is reflected to complete the bump and valley perturbations.

exposed, or not visible when the end is not exposed (meaning that the positive part is in front of the valley end). For the perturbation present in Fig. B.2, the perturbation end is not very clear due to the level of fluctuations in the signal not being much smaller than the jump due to the blind area. In this specific case, the density perturbation could not end at the end of the perturbation signature,  $\approx 102.5$  GHz, because the respective  $f_R$  profile was verified to be very smooth and the perturbation is so minimal that there would be no jump in time-of-flight, as observed in practice. Therefore, the perturbation end must be no greater than 100.2 GHz, which was the value assumed and led to a combined width of 6.1 cm. In any case, if the perturbation end is slightly before this value, the perturbation shape would not change significantly.

The next step is to estimate the perturbation depth. The depth is extracted from comparing the experimental data against WKB signals of various depths. The typical frequency band that is not compatible with the WKB signals was observed to be between one and two GHz around the time-of-flight jump, based on the 1D full-wave simulations of Chap. 4. This would mean that the signal in Fig. B.2 would be WKB compatible starting from approximately 100.5 GHz. In the case investigated here, there was an additional frequency band not WKB compatible, until approximately 102 GHz. This unexpected extended frequency band where WKB is not valid needs to be further investigated with a dedicated full-wave simulation in 1D and in the future verified with the introduction of 3D geometrical effects. Nevertheless, the WKB relevant signal could still be compared to the WKB signals of various depths, as depicted in Fig. B.4.

It is clear from observing Fig. B.4 that the synthetic signal that better describes the experimental measurement is the one with a valley depth of 0.3 GHz. The depths of 0.2 GHz and 0.4 GHz are good indications of each limit of the possible depth, leading to a final depth for the valley perturbation of  $0.3 \pm 0.1$  GHz. Taking this valley depth in the  $f_R$  profile, the final reconstructed density profile is depicted in Fig. B.5 compared to the traditional reconstruction method on the perturbed and unperturbed measurements.

It is clear from observing Fig. B.5 that the new reconstruction scheme for the blind area describes much better the perturbation and eliminates a reminiscent tail of discrepancy. These calculations were performed using a single sweep from the Tore Supra discharge 32029, when the sweeping time was 20  $\mu s$  followed by a dead time of 5  $\mu s$ . In this case, there is a significant change of the perturbation at each sweep. For a system with only 1  $\mu s$  sweep time, as it is set up now in the WEST experiment, there would be many sweeps at which the perturbation can be considered stationary. In this case, the sum of many sweeps can provide a much better signal of a perturbation, containing less fluctuations. This is critical for the analyses of the time-of-flight over blind areas because

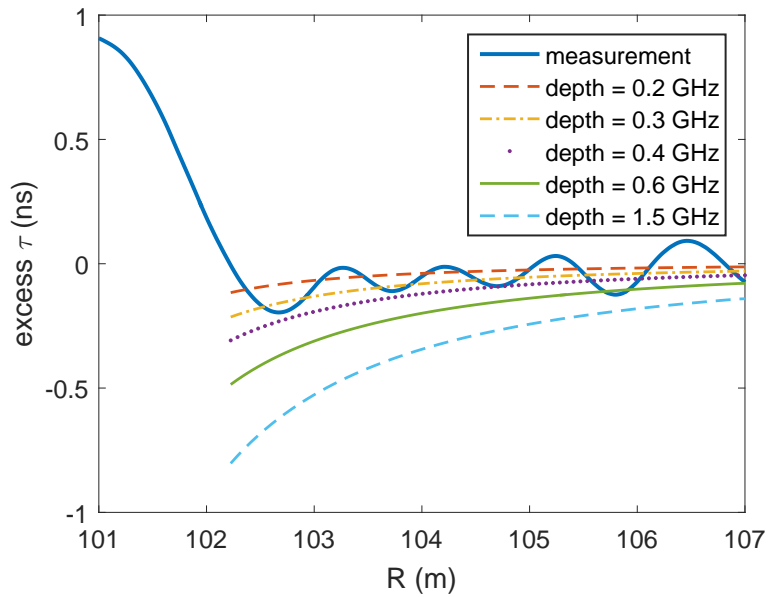


Fig. B.4 Comparison between the measured perturbation signal to WKB signals including the valley density perturbation with varying depth values.

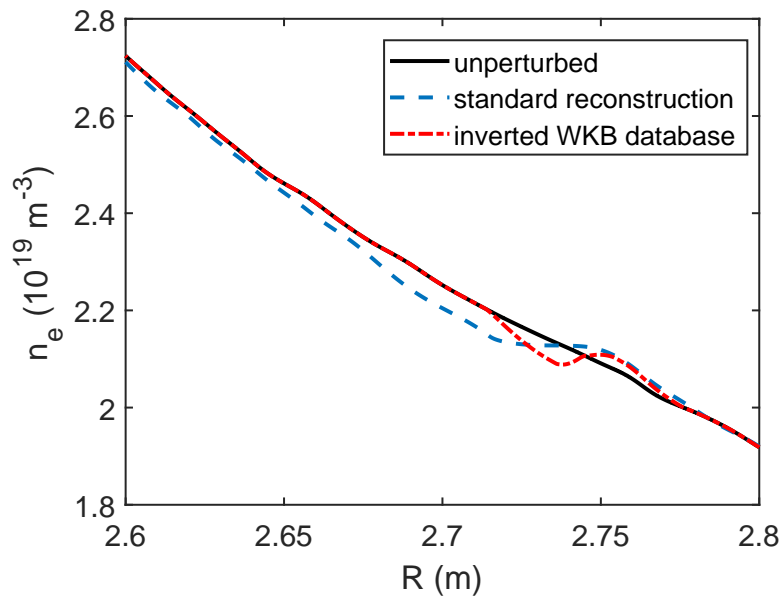


Fig. B.5 The reconstructed density profiles using the standard reconstruction method on the perturbed and unperturbed measurements versus the new method to reconstruct blind areas introduced in Chap. 4.

the narrow bandpass filter must not be applied in order to conserve the perturbation signature. Using the sum of many sweeps would improve the determination of the perturbation width and decrease the error bar of the depth calculated. This improvement is critical in applications near the limits of validity of the reconstruction method of blind areas.

# Appendix C

## Experimental errors in the initialization technique

All error sources in the initialization technique have been introduced in Chap. 5. This appendix focuses on analyses done after the deposition of the PhD manuscript. First, the experimental problem of determining which is the first reflected probing frequency is observed, followed by an experimental evidence of perturbations around the initialization frequency. Fig. C.1 shows an example of the initialization frequency band on an experimental case from the shot 32029 in Tore Supra.

The top plot of Fig. C.1 shows a spectrogram bandpass filtered between 3 and 22 MHz. The dashed white line marks the probing frequency at which the broadband fluctuation decreases, leaving a clear branch from the waves reflected in the plasma. The bottom plot shows the amplitude rise when the waves start to be reflected at the plasma. In order to initialize the profile reconstruction, the first reflected frequency must be determined. This task is not straight forward since there are no guidelines in the literature on how to find the initialization frequency. The only study on this topic was based on full-wave simulations in 1D considering linear density profiles around the initialization frequency [78]. This reference provided the guideline of using the -10 dB mark in the amplitude rise counting from the top of the amplitude rise, as marked by the black dashed line in the bottom plot of Fig. C.1.

The experimental problem is then on how to determine the correct initialization frequency, which can be anywhere between the white and black dashed lines in Fig. C.1. This range of approximately 1 GHz leads to an uncertainty in Tore Supra of around 3 cm. The uncertainty of the same frequency bandwidth in the JET experiment would translate to an uncertainty of 4 cm. These uncertainties are quite large compared to the desired operation accuracy in ITER of at least 5 mm.

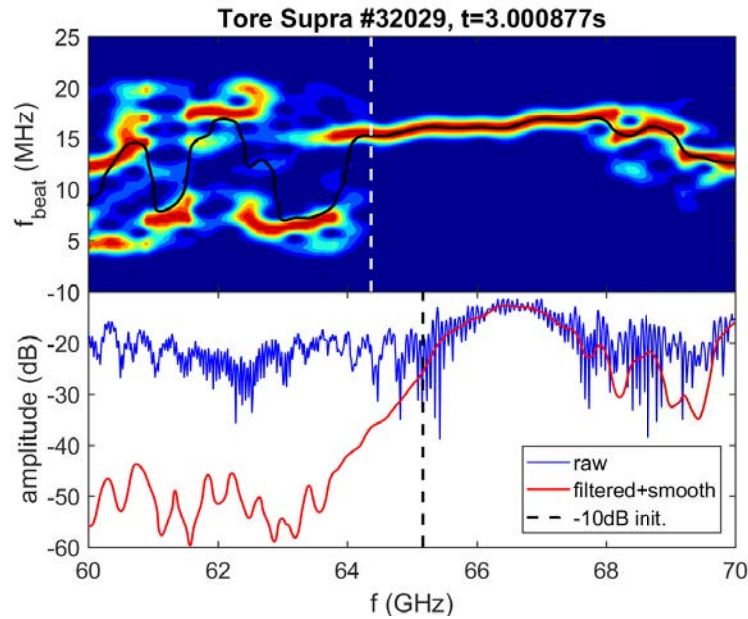


Fig. C.1 Top: spectrogram around the initialization frequency, bandpass filtered between 3 and 22 MHz. The white dashed line marks a drop of the broadband fluctuations. Bottom: the amplitude rise around the initialization frequency. The dashed black line marks the frequency that has amplitude of -10 dB compared to the top of the amplitude rise.

Fig. C.2 shows an example for the Tore Supra shot 32029, comparing two cases; one case in the top, where there are no apparent fluctuations around the initialization frequency, and another case at the bottom plot where there is a small perturbation around the initialization frequency.

The cases depicted in Fig. C.2 demonstrate in experimental data the problem of perturbations in the vicinity of the initialization frequency, as investigated with full-wave simulations in Sec. 5.3. The edge perturbation in Fig. C.2 pushes the initialization into higher frequencies. This case is not as evident as in Fig. 5.16 from the full-wave simulation due to the fact the discharge analysed is from a quiet low confinement mode (L-mode) discharge in Tore Supra. The influence of edge perturbations will be much more apparent when analysing high confinement mode (H-mode) discharges that feature relaxation events ejecting dense filaments.

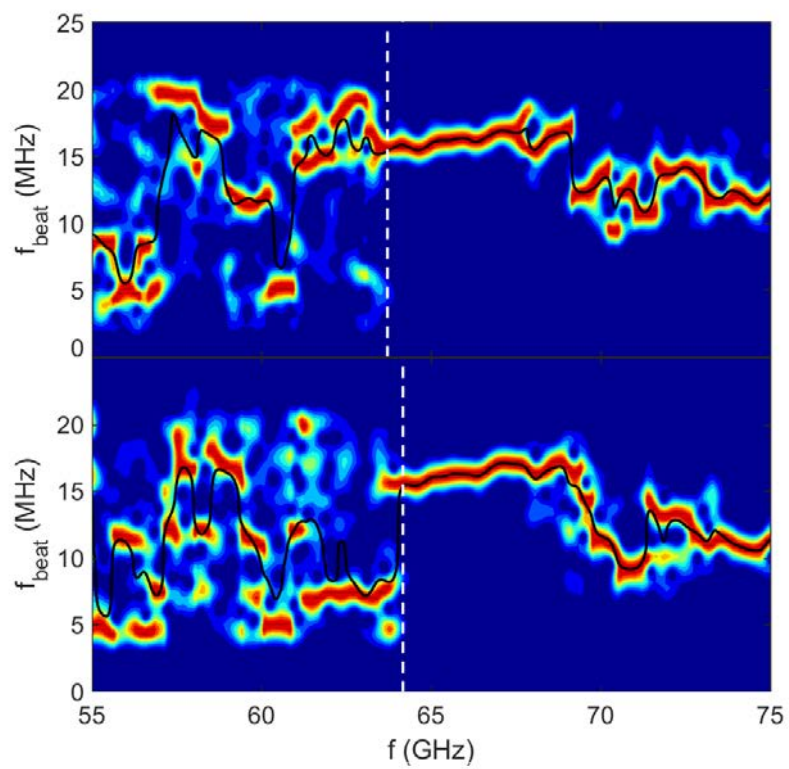


Fig. C.2 Comparison of the probing frequency where the broadband fluctuation decreases for two sweeps around  $t = 3.02$  s at the Tore Supra shot 32029.

